BRNO UNIVERSITY OF TECHNOLOGY
VYSOKÉ UČENÍ TECHNICKÉ V BRNĚ

FACULTY OF CHEMISTRY
FAKULTA CHEMICKÁ

Relativistic Effects on Light-Atom NMR Chemical Shifts: Origin, Trends, and Applications

HABILITATION THESIS IN PHYSICAL CHEMISTRY

Mgr. Jan Vícha, Ph.D.

Brno 2025

Obsah

List of Abbreviations

- **1eX2C**: One-Electron Exact Two-Component
- **2c**: Two-Component (relativistic method)
- **4c**: Four-Component (relativistic method)
- **(e)amfX2C**: (Extended) Atomic Mean-Field Exact Two-Component
- **amfX2C**: Atomic Mean-Field Exact Two-Component
- **COSMO**: Conductor-like Screening Model (solvation model)
- **CS**: Chemical Shift
- **DFT**: Density Functional Theory
- **DR-TDDFT**: Damped Response Time-Dependent Density Functional Theory
- **EDA**: Energy Decomposition Analysis
- **EPR**: Electron Paramagnetic Resonance
- **GGA**: Generalized Gradient Approximation
- **HA**: Heavy Atom
- **HALA**: Heavy-Atom on Light-Atom
- **HB**: Hydrogen Bond
- **HF**: Hartree-Fock
- **IR**: Infrared
- **IRPD**: Infrared Photodissociation Spectroscopy
- **LA**: Light Atom
- **LP***: Vacant Lone Pair
- **LP**: Lone Pair
- **MAS**: Magic-Angle Spinning
- **mmfX2C**: Molecular Mean-Field Exact Two-Component
- **MO**: Molecular Orbital
- **NBO**: Natural Bond Orbital

- **NMR**: Nuclear Magnetic Resonance
- **NQEs**: Nuclear Quantum Effects
- **OMC**: Orbital Magnetic Coupling
- **PBE0**: A hybrid DFT functional combining PBE with exact exchange
- **PIMD**: Path-Integral Molecular Dynamics
- **ppm**: Parts Per Million
- **PT2**: Second-Order Perturbation Theory
- **PT3**: Third-Order Perturbation Theory
- **QTAIM**: Quantum Theory of Atoms in Molecules
- **RMSD**: Root Mean Square Deviation
- **SO**: Spin-Orbit
- **SO-EDD**: Spin-Orbit Induced Electron Density Difference
- **SO-HALA**: Spin-Orbit Heavy-Atom on Light-Atom
- **SO-ZORA**: Spin-Orbit Zeroth-Order Regular Approximation
- **SS-NMR**: Solid-State Nuclear Magnetic Resonance
- **TMS**: Tetramethylsilane (NMR reference)
- **X2C**: Exact Two-Component (relativistic Hamiltonian)
- **XAS**: X-ray Absorption Spectroscopy
- **XC**: Exchange-Correlation

Abstract

This habilitation thesis summarizes the key points of my research on relativistic effects on NMR chemical shifts of light atoms near heavy elements, particularly on spin-orbit heavy-atom on light-atom (SO-HALA) effects. The thesis briefly covers the theoretical background of SO-HALA effects and various computational and analytical methods for their calculation. The central part of the thesis is dedicated to the analysis, understanding, and practical applications of SO-HALA effects. I am showing how SO-HALA effects and relativistic NMR chemical shifts depend on the electronic structure of heavy elements across the Periodic Table, how they can be used to guide experimental efforts, how they affect NMR chemical shift ranges, and how they may serve as probes for structural determination. The thesis is written as a commentary on selected articles covering all aspects of relativistic NMR research, from validation of computational methods, development and application of analytical tools, search for general concepts, combining computations with experiments, explaining the structure/SO-HALA relationship, to the first proof of "through space" SO-HALA propagation and beyond. The thesis also represents my opinions and my point of view on the matter, as I seek to connect the elusive concept of relativistic effects with the reality of molecular structure.

Abstrakt

Tato habilitační práce shrnuje klíčové části mojí práce věnované výzkumu relativistických efektů na NMR chemické posuny lehkých atomů v blízkosti těžkých prvků, obzvláště na spin-orbit efekt těžkého atomu na lehký atom (SO-HALA). Práce stručně popisuje teoretické základy SO-HALA efektů a různé výpočetní a analytické metody pro jejich výpočet. Hlavní část práce je věnována analýze, pochopení a zejména praktickým aplikacím SO-HALA efektů. Ukazuji, jak SO-HALA efekt a relativistické chemické posuny NMR závisí na elektronové struktuře těžkých prvků napříč periodickou tabulkou, jak je lze využít k podpoře experimentálního úsilí, jak ovlivňují rozsahy NMR chemických posunů a jak je lze využít coby sond pro určování struktury molekul. Práce je psána jako komentované shrnutí mých vybraných článků pokrývajících všechny aspekty studia relativistického NMR, od validace výpočetních metod, vývoje a aplikace analytických nástrojů, hledání obecných vztahů, kombinování výpočetních a experimentálních metod, vysvětlení vztahu mezi molekulární strukturou a SO-HALA efekty, až po první důkaz šíření SO-HALA efektů mimo chemické vazby a dalších. Práce reprezentuje mé názory a pohled na tuto problematiku, ve které se snažím propojit těžko uchopitelný koncept relativistických efektů s realitou molekulární struktury

Foreword

Although I am talking about the research summarized in this thesis as “mine”, I am well aware that we all stand on the shoulders of the giants, and sometimes they even walk among us. I was lucky enough to meet and even work with several of them – the people who formulated the very foundations of the theories that I have used in my research, and without which none of this would be possible. As a young student, I spent several months in the group of Prof. Pekka Pyykkö, one of the founding fathers of relativistic NMR theory. The stay opened the doors into the relativistic NMR community, which, albeit small, is full of excellent scientists and great people. Let me thank at least a few of them:

First, I would like to thank Prof. Radek Marek, my Ph.D. supervisor and friend, who sent me on this fascinating relativistic journey, and to Assoc. Prof. Michal Straka, whose “crazy” ideas turn out to be true more than once, sometimes for entirely different reasons than initially expected. Next, I would like to thank my two ReSpected friends, Dr. Komorovský and Dr. Repiský, for their great ReSpect code, a large whiteboard, always full of equations so advanced that they looked like something that was found in a UFO crash site, and for the inspiration that they provided. I also thank my dear friend Dr. Michael Patzschke for his enthusiasm, humor, and for teaching me the basics of NMR relativistic calculations when I knew even less than I know now. And to all others who made days and nights in Mariapfarr a relativistic heaven full of inspiration, particularly to Vladimir Malkin and Martin Kaupp, who made it possible.

To Zdenka, who makes my heart both spin and orbit around hers.

Introduction

Nuclear magnetic resonance spectroscopy (NMR) is one of the most valuable analytical techniques. Since the discovery of NMR phenomena in 1946 by Felix Bloch at Stanford University and Edward Purcell at Harvard University,[1, 2] NMR has evolved from a physics experiment into an indispensable tool that has essentially revolutionized structural chemistry.

The NMR is based on specific atomic nuclei possessing intrinsic magnetic moments due to their non-zero nuclear spin. This quantum mechanical property manifests when these nuclei are placed in an external magnetic field.[3] When exposed to an external magnetic field, nuclear spins align parallel or antiparallel to the field direction, creating discrete energy levels whose separation corresponds to the irradiation frequency. The fundamental discovery that transformed NMR from a physics curiosity into a chemical tool emerged when researchers realized that the exact resonance frequency of a given nucleus depends not only on the applied magnetic field strength but also on its local electronic environment. This phenomenon, known as nuclear magnetic shielding, occurs because electrons surrounding the nucleus create local magnetic fields that shield the nucleus from the external field to varying degrees.[3] The local electronic environment thus produces characteristic resonance frequencies that serve as fingerprints for different chemical environments. Later, the NMR chemical shift (CS) scale was established instead of absolute magnetic shielding. The CS is measured in parts per million (ppm) relative to standard reference compounds. It can thus be used to determine the differences in chemical shielding between nuclei at different resonance frequencies, allowing direct comparison of the results, disregarding the field strength.

The versatility of NMR spectroscopy has led to its widespread adoption across numerous scientific disciplines. In organic chemistry, NMR provides detailed information about molecular structure, stereochemistry, and conformational dynamics, allowing chemists to reveal which atoms are directly connected and determine the spatial arrangements of these connections and the dynamic processes that interconvert different molecular conformations.

In biochemistry and structural biology, NMR has proven invaluable for studying proteins, nucleic acids, and other biomolecules in their native aqueous environments by using multiple NMR-active nuclei, such as ^{1}H, ^{13}C, ^{15}N, and ^{31}P. [4, 5] Unlike crystallographic methods that provide snapshots of molecules in crystal lattices, solution-state NMR can capture the dynamic nature of biological systems, revealing conformational changes, binding interactions, and enzymatic mechanisms crucial for understanding biological function. The ability to observe biomolecules under physiological conditions has made NMR

essential for drug discovery, protein folding studies, and investigations of molecular recognition processes.

The materials science applications of NMR include characterization of polymers, ceramics, nanomaterials, and solid-state systems. The technique provides unique information about local structure, phase composition, molecular dynamics, and interfacial phenomena.[6, 7] Solid-state NMR methods have become particularly important for studying non-crystalline materials, surface chemistry, and heterogeneous systems that are difficult to characterize by other techniques. The development of magic-angle spinning and other solid-state NMR techniques has extended the reach of NMR to virtually any solid material.

The CS represents one of the most information-rich aspects of NMR spectroscopy. CS typically spans ranges of several hundred parts per million for ^{13}C nuclei and approximately 15 ppm for protons in organic compounds. CS reflects the complex interplay between diamagnetic and paramagnetic nuclear magnetic shielding contributions. While diamagnetic contributions reflect local electron density around the nucleus and provide shielding effects, paramagnetic contributions arise from magnetic coupling between occupied and virtual molecular orbitals in external magnetic fields. Both reflect the electronic structure of the molecule in question.[8]

The diamagnetic shielding contribution is relatively straightforward to understand and calculate. It arises from the movement of electrons in closed shells around the nucleus in response to the external magnetic field. This contribution scales with electron density at the nucleus and provides the baseline shielding modified by chemical bonding and molecular environment.

On the other hand, the paramagnetic contribution involves mixing ground and excited electronic states. It is much more sensitive to subtle aspects of electronic structure, including orbital energies, symmetries, and overlaps, as briefly discussed in subsequent chapters.

For several decades, empirical correlations between CS and molecular structure have been developed and refined through extensive experimental studies, allowing chemists to predict and interpret NMR spectra based on well-established trends and additive models. Functional groups, aromatic systems, coordination environments, and stereochemical arrangements all produce characteristic CS patterns for structural identification. These empirical approaches have been codified in extensive databases and prediction algorithms that enable routine and fast spectra assignment and structural analysis without demanding quantum-chemical calculations.

Although these empirical approaches are valid in most organic compounds, heavy atoms in molecules can lead to surprising and counterintuitive NMR observations that fundamentally challenge traditional understanding of CS behavior. In contrast to the elements from the first three periods of the periodic table, heavy atoms introduce entirely new physical phenomena that can dramatically alter the electronic structure and magnetic response of neighboring light atoms.

One example is the anomalous CS trend of light atoms bound to halogen compounds, known as "normal halogen dependence".[9] Briefly, the CS of light atoms bound to different halogens decreases with the increase in the halogen proton number, even when conventional electronic factors suggest otherwise. Traditional theories of nuclear magnetic shielding cannot explain these unusual CS patterns, because they are primarily caused by various heavy-atom on the light-atom (HALA) relativistic effects.

Despite their, for most chemists, enigmatic origin, the HALA relativistic effects are not mere spectroscopic curiosities. They carry important information about electronic structure and bonding characteristics that are inaccessible through conventional NMR analysis.[10] The magnitude and sign of these unusual shifts show systematic correlations with factors such as the oxidation state of the heavy atom, the nature of its electronic configuration (particularly the presence or absence of occupied lone pairs), and the degree of covalent character in bonding with neighboring light atoms. HALA effects can also be extensive, pushing the CS of neighboring light atoms well outside standard CS ranges, thus complicating the experimental analysis.

This thesis summarizes and comments on some of my works [10–29], dedicated to relativistic NMR chemical shifts, understanding of their propagation and origin, and applications in structure elucidation. To provide the required context, however, it is necessary to start with a brief overview of non-relativistic NMR theory.

Part 1: Theoretical background

1.1 Nonrelativistic magnetic shielding and chemical shift

Nuclear magnetic shielding represents one of the most sensitive probes of molecular electronic structure available to chemists, providing detailed information about the local electronic environment surrounding magnetic nuclei. The fundamental physics underlying the origin of nuclear magnetic shielding was established by Norman Ramsey in 1950.[8] Ramsey showed that the nuclear shielding constant σ can be decomposed into diamagnetic σ^d and paramagnetic σ^p contributions:

$$\sigma = \sigma^d + \sigma^p \qquad \text{Eq. (1)}$$

where σ^d represents the diamagnetic contribution, and σ^p the paramagnetic contribution.

As mentioned in the Introduction, the diamagnetic contribution σ^d arises from the movement of the electrons in closed shells around the nucleus induced by the external magnetic field, providing shielding to said field. Following Ramsey's original derivation, this term can be expressed as:

$$\sigma^d = \frac{\mu_0 e^2}{12\pi m} \int \rho(\mathbf{r}) r^{-1} d^3 r \qquad \text{Eq. (2)}$$

where ρ(r) is the electron density, μ_0 is the permeability of free space, *e* is the elementary charge, *m* is the electron mass, and the integral extends over all space.

The diamagnetic term provides the “baseline” shielding that is present in all atoms, even in the absence of low-lying excited electronic states. It scales approximately with the number of electrons around the nucleus and their average distance from the nuclear center. This term is typically positive, providing shielding effects. It is relatively insensitive to chemical environment changes, primarily reflecting the ground-state electron density distribution around the nucleus from core orbitals. For atoms in molecules, the diamagnetic term is modified by molecular orbital overlap and bonding effects, but these modifications are usually modest compared to paramagnetic contributions. In heavy-atom compounds, additional diamagnetic contributions can arise from the occupied orbitals of the heavy atom, even when these orbitals are spatially distant from the light nucleus being observed. [30]

The paramagnetic contribution σ^p originates from magnetic coupling between occupied and virtual molecular orbitals in an external magnetic field. This term is typically negative, causing deshielding, and is highly sensitive to the electronic structure of the molecule. Within the framework of second-order perturbation theory, as derived by Ramsey [8], the paramagnetic shielding can be written as:

$$\sigma^p = \frac{\mu_0 e^2}{4\pi m} \sum_{i,j} \frac{\langle i|\hat{L}|j\rangle\langle j|r^{-3}|i\rangle}{E_j - E_i} \qquad \text{Eq. (3)}$$

where $|i\rangle$ and $|j\rangle$ represent occupied and virtual molecular orbitals, respectively, $\hat{L}$ is the orbital angular momentum operator, and the energy difference in denominators (E_j - E_i) determines the magnitude of the paramagnetic contribution.

The paramagnetic term depends critically on several factors that have also been extensively studied in the context of heavy-element compounds. First, the matrix elements of the orbital angular momentum operator, governed by symmetry, determine which orbital transitions can contribute to the magnetic coupling [9, 31, 32]. Second, the inverse cube distance factor r^{-3} in the non-relativistic paramagnetic nuclear-spin-electron-orbit operator (do not confuse with relativistic electron-spin-electron-orbit interaction, discussed further) makes this contribution usually localized around the nucleus. Third, the energy denominators favor contributions from frontier orbital transitions, particularly those involving the highest occupied and lowest unoccupied molecular orbitals. [33, 34]

Given these factors, the paramagnetic contribution is usually responsible for most shielding differences. It provides information about molecular orbital energies, symmetries, and orbital overlaps, making it an excellent probe of chemical bonding and electronic structure changes. The sensitivity of the paramagnetic term to molecular orbital structure explains why NMR is so effective for distinguishing between different molecular conformations, coordination environments, and electronic states.

The prime example of using NMR σ^d and σ^p contributions for detailed molecular structure analysis is our study explaining unusual chemical shifts of ^{3}He physically trapped inside various fullerene cages, such as He@C_{60} and He@C_{70}.[28] In these systems, the helium atom is chemically inert, meaning its nucleus acts as a pristine probe of the magnetic field generated by the host fullerene cage's electrons, and the chemical shift of the entrapped ^{3}He atom is highly sensitive to the cage's structure and charge state. For instance, upon reduction of the neutral fullerenes to their hexa-anions, the ^{3}He in He@C_{60}^{6-} is shielded by an additional ~43 ppm, whereas in He@C_{70}^{6-} it is paradoxically deshielded by ~37 ppm. This counterintuitive behavior cannot be explained by simple electrostatic arguments, which would predict increased diamagnetic shielding in both cases due to the added electron density on the cage.

Our analysis revealed that the key to understanding these dramatic and opposing chemical shift changes lies in the high symmetry of the fullerene cages themselves, modulating σ^p(^{3}He). The total σ(^{3}He) is a delicate balance between a large, positive (shielding) σ^d and a large, negative (deshielding) σ^p contributions, both originating from the cage's electrons. We found that the diamagnetic term from the

core and inner valence orbitals of the cages provides a substantial and relatively constant baseline shielding of about +140 ppm to ^{3}He. Therefore, the differences in the final CS are dictated by the highly variable paramagnetic term, which is governed by orbital magnetic couplings (OMCs) between the cage's frontier molecular orbitals. In the highly symmetric I_h-C_{60} cage, the HOMO is a five-fold degenerate $6h_u$ orbital, and the LUMO is a three-fold degenerate $7t_1u$ orbital. In the neutral state, the symmetry-allowed coupling between these two frontier orbitals ($6h_u \rightarrow 7t_1u$) generates a massive paramagnetic deshielding effect of about -70 ppm, which partially cancels the diamagnetic shielding from the cage, resulting in a slight net chemical shift of -6.4 ppm. When six electrons are added to form the He@C_{60}^{6-} anion, they occupy the $7t_1$u LUMO. This occupation completely quenches the dominant HOMO→LUMO deshielding pathway. Because of the high symmetry, the newly occupied $7t_1u$ orbital has very few symmetry-allowed couplings to higher-lying virtual orbitals. Consequently, the large paramagnetic deshielding is removed without introducing significant new deshielding pathways. In contrast, the underlying extensive diamagnetic shielding from the cage remains, leading to the observed strong shielding effect.

The situation is entirely different in the less symmetric D_{5h}-C_{70} cage. In the neutral He@C_{70}, several frontier orbital couplings contribute to a total paramagnetic deshielding of about -50 ppm. Upon reduction to He@C_{70}^{6-}, the added electrons again quench some of these couplings. However, because of the lower symmetry of the C_{70} cage, the newly occupied frontier orbitals have many opportunities for symmetry-allowed magnetic couplings with nearby virtual orbitals. These new couplings introduce a large additional paramagnetic deshielding (about -56 ppm) that more than compensates for the quenching of the original pathways. The net result is a dramatic increase in deshielding of the ^{3}He nucleus, explaining the puzzling positive shift observed experimentally, representing the current limits of ^{3}He CS range.

This example illustrates how the symmetry of the molecular cage orbitals can act as a critical switch, allowing or forbidding specific orbital magnetic couplings that determine the balance between shielding and deshielding. This highlights the capabilities of NMR shielding analysis as a powerful tool for probing subtle features of molecular architecture even in the absence of chemical bonds.

In practice, absolute nuclear magnetic shielding constants are seldom used in chemistry outside of computational benchmarks and other specialized studies. Instead, differences in shielding are expressed as chemical shifts (CS), i.e., relative to reference compounds according to:

$$\delta = (\sigma_{ref} - \sigma_{sample})/\sigma_{ref} \times 10^6 \qquad \text{Eq. (4)}$$

where σ_{ref} is the shielding constant of the reference compound, and the result is expressed in parts per million (ppm).

For experimental ^{1}H NMR, tetramethylsilane (TMS) is the primary reference due to its high symmetry, chemical inertness, and convenient CS position. For ^{13}C NMR, TMS is also commonly used, while other nuclei have their own established reference standards.[35] The relative CS scale is also helpful for theoretical calculations, because it cancels many systematic errors, while preserving the chemically relevant differences between compounds. However, secondary references are often necessary in computational studies to further reduce systematic errors and improve agreement with experimental data, particularly in the framework of Density Functional Theory (DFT).[11, 12]

1.2 Relativistic magnetic shielding and chemical shift

While the conventional theory of non-relativistic quantum mechanics provides excellent foundations for compounds containing light elements, the presence of heavy atoms introduces new physical phenomena that can dramatically alter chemical shift values and patterns. This chapter offers only a basic overview of the relativistic theory. For more details on this topic and the SO-HALA effects in general, see our Chemical Reviews review. [10]

The influence of relativistic effects on NMR CS has been known for over half a century. The first attempts to explain the observations of unusual CS in HA compounds were reported by Nakagawa and coworkers in the 1960s, who noticed anomalous proton CS in halobenzenes that could not be explained by conventional electronic structure theory. [36, 37] These pioneers suggested a "spin-polarization" mechanism causing additional shielding, though the underlying relativistic nature of the phenomenon was not yet fully appreciated.

The recognition that relativistic corrections to electronic structure could not be ignored for accurate treatment of heavy-atom compounds came in the 1970s [38]. It led to the development of quantitative computational methods capable of treating these effects. [39–41]

At this point, it is necessary to emphasize that there are two major contributors to HALA effects: the scalar (SC) and spin-orbit (SO) contributions. Following and expanding on Ramsey's original formalism, the relativistic nuclear shielding constant σ can be written as:

$$\sigma = \sigma^d + \sigma^p + \sigma^{SR} + \sigma^{SO} + \text{higher-order terms} \qquad \text{Eq. (5)}$$

To describe the underlying theory, let us start with a closed-shell singlet system. At the Hartree-Fock level, the non-relativistic Fock equations are:

$$F^{NR}\varphi_p = \varepsilon_p\varphi_p \qquad \text{Eq. (6)}$$

where φ_p and ε_p are the molecular orbitals, *MOs*, and one-electron energies, respectively. The one-electron part of the Fock operator, F^{NR} corresponds to the non-relativistic Schrödinger operator h^{NR}. To include the relativistic effects, it is necessary to expand the Schrödinger operator h^{NR} with three corrections, resulting in the well-known Pauli Hamiltonian[42]

$$h^{Pauli} = h^{NR} + h^{MV} + h^{DW} + h^{SO} \qquad \text{Eq. (7)}$$

Scalar relativistic effects arise from corrections to the kinetic energy operator in the Schrödinger equation that account for the relativistic mass increase of electrons moving at high velocities near heavy nuclei. These corrections include the mass-velocity and Darwin correction terms.[9] The mass-velocity correction accounts for the change in electron mass with velocity approaching the speed of light according to special relativity:

$$h^{MV} = -\frac{p^4}{8m_0^3c^2} \qquad \text{Eq. (8)}$$

The Darwin correction arises from the finite size of the electron and its interaction with the nuclear Coulomb field:

$$T_{\text{Darwin}} = \frac{\pi e^2 \hbar^2 Z}{2m_0^2c^2}\delta(r) \qquad \text{Eq. (9)}$$

where Z is the nuclear charge and $\delta(r)$ is the Dirac delta function. [43]

The magnitude of scalar relativistic effects scales approximately with Z^2, making them increasingly important for heavy elements. These effects typically produce systematic shifts that are relatively predictable and are easily included in modern quantum chemical calculations.[44] Scalar relativistic effects primarily influence CS through the relativistic contraction of s orbitals and related expansion of higher angular momentum orbitals, which impacts electron density around the nucleus, affecting diamagnetic and paramagnetic shielding contributions. Changes in orbital energies and shapes due to relativistic corrections modify the paramagnetic contribution through altered energy denominators and orbital overlaps.

The spin-orbit shielding, σ^{SO}, which arises from mixing electronic states with different spin multiplicities due to spin-orbit coupling at heavy atoms, is the most important of many relativistic corrections that introduce additional terms to the nuclear shielding expression. For more details, see, e.g., works by Vaara et al. [45, 46]. The spin-orbit Hamiltonian can be written as:

$$h^{SO} = \frac{1}{4c^2}\sum_{N=1}^{nuc} Z^N \, r_N^{-3} \, \hat{\boldsymbol{l}}^N \cdot \boldsymbol{\sigma} \qquad \text{Eq. (10)}$$

where r_N is the electron position operator relative to the position of nucleus N.

The σ^{SO} scales approximately as Z^4 and becomes increasingly important for heavy element magnetic shielding. Pÿkko and Görling have, perhaps half-jokingly, termed the σ^{SO} effect induced by a heavy atom on its own shielding as the "HAHA" (heavy atom on heavy atom) effect, maybe because their magnitude can be truly ridiculous (up to several thousand ppm). [32]

1.2.1 Computational methods

Accurately predicting relativistic effects on NMR CS requires sophisticated quantum chemical methods that adequately account for scalar relativistic effects and spin-orbit coupling. Over the past decades, many approaches have been developed and refined to meet this challenge, each with distinct advantages and limitations depending on the molecular system under study and the desired accuracy.[10] The main types include:

Four-component Dirac-Coulomb methods represent the most rigorous approach to relativistic NMR calculations. These methods solve the Dirac equation directly, treating all relativistic effects variationally without approximation.[47] The four-component Dirac equation can be written as

$$[c\,\boldsymbol{\alpha}\cdot\mathbf{p}+\beta mc^2+V(\mathbf{r})]\Psi(\mathbf{r})=E\Psi(\mathbf{r}) \qquad \text{Eq. (11)}$$

where α and β are the Dirac matrices, $\boldsymbol{p}$ is the momentum operator, m is the electron rest mass, c is the speed of light, $V(r)$ is the potential, and Ψ is the four-component wavefunction.

In the four-component framework, both large and small components of the electronic wavefunction are included explicitly, allowing for the emergence of spin-orbit coupling and other relativistic effects. The method thus naturally includes all relativistic corrections to infinite order and provides a benchmark against which different approaches can be evaluated. However, the raw computational cost scales with approximately a factor of sixteen compared to non-relativistic calculations due to the doubling of basis functions and the complex arithmetic required for the Dirac matrices.[48] The computational implementation also requires careful treatment of several technical aspects, mainly regarding the basis sets. For instance, the small component basis functions must be constructed to avoid variational collapse and maintain kinetic balance with the large component functions. For magnetic property calculations, which is the case of NMR, the basis functions must satisfy magnetic balance conditions to ensure proper gauge-origin independence.[49]

Despite high computational demands, four-component methods have become increasingly practical for molecules up to moderate size, particularly for NMR property calculations where high accuracy is essential. Recent algorithmic improvements, including diagonalization-free SCF procedures and efficient parallel implementations, have significantly reduced the computational requirements and made four-component calculations feasible for systems containing hundreds of atoms, which we used, for instance, in our study on heavy element hydrides.[13] The four-component approach has been implemented in several quantum chemistry codes and has proven highly accurate for predicting HALA effects. [50]

Two-component relativistic methods offer computationally more efficient 4c alternatives, retaining most of the accuracy of four-component approaches. These methods eliminate the small component of the Dirac equation through various transformation procedures, reducing the computational requirements while preserving the essential physics of relativistic effects.

The exact two-component (X2C) Hamiltonian provides a rigorous framework for eliminating the small component of the Dirac equation algebraically, reproducing four-component results with excellent accuracy for most molecular properties, including NMR CS. The X2C approach performs a unitary transformation that decouples the positive and negative energy states of the Dirac Hamiltonian [51, 52]:

$$\mathbf{H}_{\mathrm{X2C}} = \mathbf{U}^{\dagger}\mathbf{H}_{\mathrm{DC}}\mathbf{U} \qquad \text{Eq. (12)}$$

where $\boldsymbol{H}_{X2C}$ is the exact two-component Hamiltonian, $\boldsymbol{H}_{DC}$ is the four-component Dirac–Coulomb Hamiltonian, $\boldsymbol{U}$ is the unitary transformation matrix that block-diagonalizes $\boldsymbol{H}_{DC}$, decoupling the positive- and negative-energy states, $\boldsymbol{U}^{\dagger}$ is the Hermitian conjugate (adjoint) of $\boldsymbol{U}$.

The unitary transformation preserves spin-orbit coupling to infinite order while reducing computational requirements by approximately a factor of four compared to four-component methods. Atomic mean-field X2C (amfX2C) and other variants of X2C that confine the transformation to atomic blocks provide additional computational savings while maintaining near-four-component accuracy. [14, 53]

Besides X2C methods, various approximate approaches have been implemented in the two-component framework. The zeroth-order regular approximation (ZORA) represents one of the most widely used two-component approaches that has succeeded in numerous NMR applications. The ZORA Hamiltonian is derived from the Dirac equation by assuming that the potential energy is small compared to the speed of light. The ZORA Hamiltonian is typically written as [54]:

$$H_{\mathrm{ZORA}} = \vec{\sigma}\cdot\vec{p}\,\frac{c^2}{2mc^2-V}\,\vec{\sigma}\cdot\vec{p} + V \qquad \text{Eq. (13)}$$

where $\vec{\sigma}$ are the Pauli matrices, $\vec{p}$ is the momentum operator, V is the potential energy, m is the electron mass, c is the speed of light. This formulation captures the majority of essential physics of relativistic effects while remaining computationally efficient.

Spin-orbit ZORA (SO-ZORA) calculations have been extensively validated against experimental data and four-component calculations of σ^{SO}, showing good agreement for most chemical systems. As shown in Chapter 1.4, the SO-ZORA approach has significant limitations.

1.3 SO-HALA Effects

The relativistic effects on nuclear shielding, particularly the σ^{SO}, are not limited only to the heavy atom itself, but can propagate through the molecule to nearby light atoms. Fundamental work describing and summarizing the origin of HALA effects came in 1987 with Pekka Pyykkö's work on interpreting relativistic contributions in NMR. [32] Pyykö and Görling unequivocally demonstrated that spin-orbit coupling at heavy atoms could induce substantial changes in the NMR CS of adjacent light nuclei through normally forbidden mixing of singlet and triplet electronic states. In response to the term HAHA effect coined by Pyykkö, this effect has been later termed the heavy-atom on the light atom (HALA) effect. The spin-orbit part of this contribution is then the SO-HALA effect.

In the 1990s, rapid development in theoretical methods and experimental observations led to further progress in understanding how relativistic effects propagate from heavy atoms to light spectator nuclei. This culminated in 1998 with the publication of a breakthrough work by Martin Kaupp, Vladimir and Olga Malkin, and Pekka Pyykkö, aptly named "*How do spin-orbit-induced heavy-atom effects on NMR CS function?*".[31] For the first time, authors described the whole pathway of spin-orbit-induced heavy-atom effects on the light atom (SO-HALA) effect propagation. According to Kaupp et al. [31], the propagation of SO-HALA is a multi-step process that is remarkably similar to J-coupling propagation, as both phenomena involve the Fermi-contact mechanism and the propagation of spin density through molecular electronic structure, see Figure 1.[31]

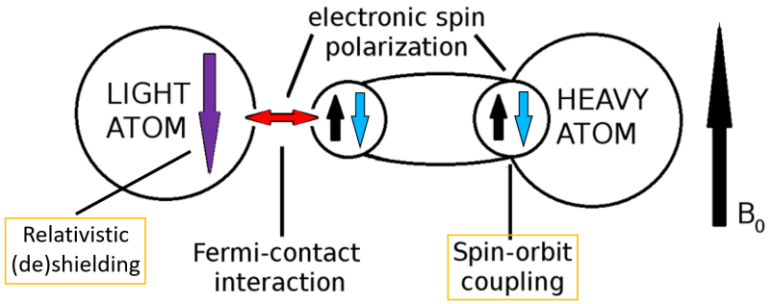

Figure 1: The schematic representation of SO-HALA propagation, based on Kaupp et al.[31]

Briefly, when a molecule is placed into an external magnetic field B_0, the spin-orbit operator at the HA nucleus mixes single and triplet states, thus inducing electron spin polarization. This "perturbation" of electron spin density can propagate through chemical bonds and may influence the nuclear magnetic moment of a neighboring light element nucleus *via* the Fermi contact mechanism. Authors also noted that the efficacy of the SO-HALA effect, and thus the size of σ^{SO} at light atom, σ^{SO}(LA), scales with the

participation of s-orbitals (s-orbital character) of the light atom in a bond with a heavy element. The higher the s-character, the more efficient the Fermi-contact mechanism is, and the larger the σ^{SO}(LA).

The remarkable resemblance of the SO-HALA mechanism with that of indirect nuclear spin–spin coupling pointed out in Kaupp's work laid the foundations for using SO-HALA effects for structure elucidation. This was used, for instance, already in 2004 by Hegetschweiler et al. [33], who used the Karplus-like behavior of SO-HALA to elucidate the structure and dynamics of Co(III) complexes at different pH levels.

Kaupp's work, however, did not elaborate on other aspects of the SO-HALA propagation mechanism, particularly those arising from the side of HA. The presented mechanism also could not explain why σ^{SO}(LA) can be both negative and positive (deshielding and shielding).

Hence, we have built on this concept to explain the SO-HALA/electronic structure relationship further. First, however, it was necessary to validate a suitable computational methodology.

1.4 Calculations of relativistic NMR chemical shifts – benchmarking and validation

My journey to relativistic NMR started with a need to use relativistic NMR chemical shift calculation to complement our experimental findings and help with structural elucidation.[11] The SO-ZORA approach implemented in the ADF software package was particularly attractive for such routine applications due to its computational efficiency, implementation of solvent effects, and broad customizing options. The goal was to complement our experimental findings regarding a series of platinum(IV) complexes with aromatic cytokinins. To interpret their NMR spectra, we have collected detailed ^{1}H, ^{13}C, and ^{15}N NMR measurements for both the free ligands and their platinum complexes in both solution and the solid state. In solution, we observed that the N3–H proton of adenine is remarkably stable, likely due to intramolecular hydrogen bonding with chloride ligands, while the N7–H proton is labile and involved in a dynamic protonation–deprotonation equilibrium, which dramatically influences the NMR chemical shift of N7. Hence, we have employed relativistic DFT SO-ZORA calculations to help interpret the experimental data. The calculations were performed using the PBE0 hybrid functional.[55, 56] By comparing experimental and DFT-calculated ^{15}N chemical shifts for the N7 atom in its protonated and deprotonated forms, we could estimate the population of each tautomeric form. For example, in pure DMF solution, the N7 site was about 38% protonated, which increased to 67% upon addition of DCl, with N7 NMR chemical shifts responding accordingly. Combining NMR spectroscopy with relativistic DFT proved decisive for elucidating subtle protonation equilibria in metal-modified nucleobases.

Including SO coupling also significantly improved the agreement with the experiment for the N9, which bears platinum. Although the difference between calculated and experimental values decreased from ~35 ppm to ~10 ppm, the overall agreement with experiment for N9 was still significantly worse than for other nitrogen atoms, which differed only by 1 – 3 ppm. It was clear that the employed computational methodology could be improved.

Therefore, I have started a thorough benchmarking study [29] in which we have focused on finding a detailed and methodologically rigorous approach to modeling the structures and NMR chemical shifts of octahedral platinum(IV) and iridium(III) complexes using relativistic DFT SO-ZORA calculations. The study was grounded in the context of bioinorganic and medicinal chemistry, where such metal complexes are of interest due to their biological activity and potential therapeutic applications.

We have systematically evaluated the performance of seven DFT functionals in optimizing the geometries of these complexes, using supramolecular clusters derived from crystallographic data as benchmarks. Among the tested functionals, PBE0 combined with the def2-TZVPP basis set and Grimme's D3 dispersion correction emerged as the most reliable for reproducing experimental geometries. This combination

balances computational efficiency and structural accuracy, making it suitable for both solid-state and solution-phase modeling.

As before, the study employed the SO-ZORA method to calculate NMR shielding constants. The geometries used in these calculations were optimized in solution using the COSMO solvation model, ensuring that the computed NMR parameters reflect realistic experimental conditions. A key finding of the study was the importance of the exact exchange component in the hybrid PBE0 functional. By adjusting the exact exchange to 40% (instead of 25% present in PBE0), we have achieved excellent agreement between calculated and experimental NMR CS. As shown later [16, 57], this adjustment compensates for the exchange–correlation (XC) response kernel, which was missing in the contemporary implementation of the SO-ZORA approach. Nevertheless, this work provided a validated and transferable computational protocol for studying SO-HALA effects in transition-metal complexes.

Subsequently, this approach was further tested in the study of organometallic dimers, $[Pd(2ppy^*)(\mu\text{-}Cl)]_2$ and $[Pt(2ppy^*)(\mu\text{-}Cl)]_2$, where 2ppy* is the cyclometalated form of 2-phenylpyridine [12]. The primary goal was to understand their structural behavior in solution and solid state, particularly their solvolysis in DMSO, and to determine the structure of the resulting species.

Using multinuclear NMR spectroscopy (^1H, ^{13}C, ^{15}N, and ^{195}Pt), we observed that both dimers retain their dimeric structures in DMF-d_7, as evidenced by consistent chemical shifts and coordination shifts compared to the free ligand. However, in DMSO-d_6, the behavior diverged significantly. The platinum dimer underwent a complete transformation into a single trans(S,N)-[Pt(2ppy*)(DMSO)Cl] species, while the palladium dimer cleaved into two distinct species in a 1:1 ratio. Based on NMR data supported by DFT calculations, we proposed that these are $[Pd(2ppy^*)(DMSO)_2]^+$ and $[Pd(2ppy^*)Cl_2]^-$, forming an ionic pair.

I performed relativistic DFT calculations using the SO-ZORA method and PBE0 functional with varying exact-exchange admixtures to confirm these findings. A previously validated 40% admixture in the functional (PBE-40) agreed best with experimental ^{15}N and ^{13}C chemical shifts, giving an excellent RMSD of $\sim$2 ppm in both cases. Calculations confirmed the proposed identities of the solvolysis products, although the NMR analysis was insufficient to distinguish between cisoid and transoid geometries of the dimers in solution.

Encouraged by these results and seeking to properly evaluate the impact of the missing XC response kernel in SO-ZORA implementation, we have performed a final and much broader validation study focused on relativistic NMR CS calculations in square-planar transition-metal complexes.[16] The study focused on systematically assessing the performance of various DFT approaches in predicting NMR shifts of various

light atoms near heavy metal centers like platinum, gold, palladium, and rhodium. This time, both two-component (SO-ZORA) and four-component (Dirac-Coulomb) relativistic methods were included, and particular focus was paid to molecular structure, solvent effects, and relativistic treatment.

As in a previous work [20], the study began by calibrating the structural models using a cluster-based approach, where the central molecule was embedded in a crystal-like environment derived from X-ray diffraction data. Among the ten tested DFT functionals, PBE0, TPSSh, and MN12SX provided the most accurate geometries, with PBE0 again performing best overall. The importance of reliable geometry optimization has been highlighted by comparing the best and worst approaches, leading to significant deviations in calculated NMR shifts, up to 22 ppm for ^{13}C and 14 ppm for ^{15}N.

Comparison of the SO-ZORA approach with the more rigorous 4c method implemented in the ReSpect code revealed the expected critical limitation of the SO-ZORA implementation - the absence of the XC response kernel. The XC response kernel is essential for accurately capturing SO effects in hybrid functionals. Its omission leads to systematic underestimation of the SO-HALA effects. The study confirmed that to compensate for the missing XC kernel in SO-ZORA, one has to artificially increase the exact exchange admixture in the PBE0 functional from 25% to 40% (PBE-40). This adjustment improves agreement with experimental data in many cases, especially for ^{13}C shifts, but the improvement is primarily based on error cancellation. Through detailed analysis of 4c calculations, we have shown that the missing XC kernel contribution accounts for approximately 15–20% of the total σ^{SO}(LA). When this kernel correction is explicitly included in the 4c framework, the standard PBE0 functional performs as well as or better than the empirically adjusted PBE-40, reaffirming the importance of a physically grounded treatment of relativistic effects. The study also evaluated the role of solvent effects using the COSMO implicit solvation model, which was particularly important for ^{15}N shifts, contributing up to 20 ppm.

Our findings regarding the necessity for rigorous implementation of the XC kernel were confirmed in the latter study[21], focusing on extremely high ^{13}C and ^{29}Si NMR chemical shifts predicted in diamagnetic low-valence compounds of thallium(I) and lead(II). The SO-ZORA approach with PBE-40, which had previously shown good agreement with experiment for systems where the SO contribution to the CS was less than ~50 ppm, begins to fail, despite the artificially increased HF exchange. The deviations of the SO-ZORA approach from experimental data grew significantly with increasing SO-HALA effects, leading to root-mean-square deviations (RMSDs) of ~17 ppm for ^{13}C. The reason for the failure was extreme SO-HALA effects in these compounds, reaching over 200 ppm for ^{13}C. This is comparable to the standard chemical shift range of this nucleus. Attempts to compensate for the missing XC kernel by increasing the exact exchange in the functional (as in PBE-40) thus fail for large SO-HALA effects.

In contrast, the four-component Dirac–Kohn–Sham (4c-DKS) method, implemented in the ReSpect code and used with the PBE functional, provides significantly better agreement with experimental data across the full range of δ^{SO}(LA) values. For ^{13}C shifts, the 4c-PBE method achieves an RMSD of just seven ppm, even in cases where δ^{SO}(LA) exceeds 200 ppm. Note that such accuracy was achieved with the GGA functional, as the size of the tested systems did not allow more computationally demanding hybrid functionals, such as PBE0, at that time.

To summarize, our validation studies established that the PBE0 functional with the triple-ζ basis set and dispersion correction provides a reliable DFT-based method for structural optimization of various heavy-element complexes. The SO-ZORA PBE-40 approach is helpful for systems with low to moderate relativistic effects and in large systems where using 4c methods is not feasible. However, it does not perform reliably in heavy-element compounds where δ^{SO}(LA) is very large. The 4c method, despite its higher computational cost, is essential in such cases.

1.5 Analysis of SO-HALA effects

To fully understand the SO-HALA effects, one has to analyze their origin at the orbital level. Many approaches have been developed over the years for decomposing SO-HALA effects into individual molecular orbital contributions, enabling a detailed understanding of their electronic structure origins. These methods are generally based on various implementations of perturbation theory, in which the magnetic field, the Fermi-contact operator, and the SO operator can be applied as perturbations to the non-relativistic or scalar relativistic ground state. [10]

One of the first DFT frameworks for the analysis of SO-HALA effects was laid out already in 1994 by Malkin et al., who used the sum-over-states method with finite-field third-order perturbation theory to calculate and later analyze the SO-HALA effect.[58] Although qualitatively correct, the quantitative agreement of this method was often limited.

Another method was implemented by Autschbach et al. for the analysis using the SO-ZORA relativistic approximation in the ADF code. [39] It allowed the analysis of two-component NMR shielding tensors within a framework of scalar relativistic natural localized molecular orbitals (NLMO) and natural bond orbitals (NBO). It is based on the second-order perturbation theory (PT2) using the Fermi contact $\hat{\delta}^{\mathrm{LA}}$ and angular-moment $\hat{l}_u^{\mathrm{HA}}$ operators as perturbations, while the SO operator is included variationally. This allows for determining Ramsey-like orbital couplings between occupied and vacant scalar relativistic molecular orbitals (MO and MO*), see Figure 2. In combination with NMLO or NBO analysis, MO and MO* composition could be further analysed regarding individual atomic orbitals, allowing considerable insight into the SO-HALA propagation. [10]

Although useful, the PT2 analysis does not provide the complete picture due to the missing SO perturbation. Therefore, we have started collaborating more closely with Dr. Komorovsky, developing third-order perturbation theory (PT3) analysis and implementing it in the 4c ReSpect code.[17] This method allowed us to fully comprehend the connection between SO and the electronic structure of heavy elements. [10, 17, 18]

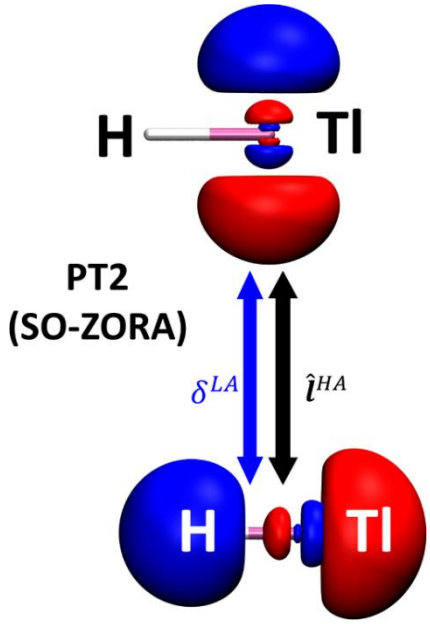

Figure 2: The example of PT2 analysis with Fermi contact $\hat{\delta}^{\mathrm{LA}}$ and angular-moment $\hat{l}_u^{\mathrm{HA}}$ operators applied to the scalar-relativistic MO of TlH.

The PT3 is generally described by the Eqs. (14) and (15), in which the occupied (φ_i, φ_j) and virtual (φ_a, φ_b) MOs are coupled *via* three operators: the SO operator, $r_{HA}^{-3}\hat{\boldsymbol{l}}^{HA}$, the Fermi contact operator, δ^{LA}, and the angular momentum operator, $\hat{\boldsymbol{l}}^{HA}$. The one-electron MO/MO* energies, ε_i, ε_j, ε_a, ε_b are present in the denominators.

$$\boldsymbol{\sigma}^{SO/FC^{\Delta}}(\mathrm{LA}) \approx -\frac{1}{c^4}\sum_{i=1}^{\mathrm{occ}}\sum_{j=1}^{\mathrm{occ}}\sum_{a=1}^{\mathrm{vac}}\frac{\langle\varphi_a|r_{HA}^{-3}\hat{\boldsymbol{l}}^{HA}|\varphi_i\rangle\langle\varphi_i|\delta^{LA}|\varphi_j\rangle\langle\varphi_j|\hat{\boldsymbol{l}}^{HA}|\varphi_a\rangle}{(\varepsilon_i-\varepsilon_a)(\varepsilon_j-\varepsilon_a)} + perm. \qquad \text{Eq. (14)}$$

$$\boldsymbol{\sigma}^{SO/FC^{\nabla}}(\mathrm{LA}) \approx +\frac{1}{c^4}\sum_{i=1}^{\mathrm{occ}}\sum_{a=1}^{\mathrm{vac}}\sum_{b=1}^{\mathrm{vac}}\frac{\langle\varphi_i|r_{HA}^{-3}\hat{\boldsymbol{l}}^{HA}|\varphi_a\rangle\langle\varphi_a|\delta^{LA}|\varphi_b\rangle\langle\varphi_b|\hat{\boldsymbol{l}}^{HA}|\varphi_i\rangle}{(\varepsilon_i-\varepsilon_a)(\varepsilon_i-\varepsilon_b)} + perm. \qquad \text{Eq. (15)}$$

Although the PT3 analysis is limited to the Fermi-contact mechanism of SO-HALA shielding ($\sigma^{SO/FC}$), this usually covers 95% of the total δ^{SO}(LA).[59, 60] PT3 thus provides both qualitative and sufficiently quantitative tools for analysis of the δ^{SO}(LA). Eqs. (14) and (15) have opposite signs and their products are marked differently, because they describe the coupling of two occupied and one vacant MO ($\boldsymbol{\sigma}^{SO/FC^{\Delta}}$) or two vacant and one occupied MO ($\boldsymbol{\sigma}^{SO/FC^{\nabla}}$). This is emphasized by the orientation of triangles in superscripts.

The reasoning behind the equations and PT3 analysis stands as follows:

1) Because of the orbital energies in the denominators, the main MO couplings arise from the frontier MOs with the smallest energy differences.

2) The frontier orbitals of HA complexes can be, in general, divided into four basic types: bonding $\sigma_{HA\text{-}LA}$, antibonding $\sigma^*_{HA\text{-}LA}$, electron lone pairs at HA, LP_{HA}, and vacant non-bonding orbitals at HA, termed as "vacant lone pairs" for the sake of simplicity, LP^*_{HA}.

3) Assuming the presence of only the orbital types described in 2), the PT3 expressions describe six distinct coupling contributions to $\sigma^{SO/FC}$(LA), with three contributions for each SO/FC type ($\boldsymbol{\sigma}^{SO/FC^{\Delta}}$and $\boldsymbol{\sigma}^{SO/FC^{\nabla}}$), which can be visualized using triangle representations where each vertex corresponds to a molecular orbital and each edge represents one of the three perturbation operators, see Figure 3.

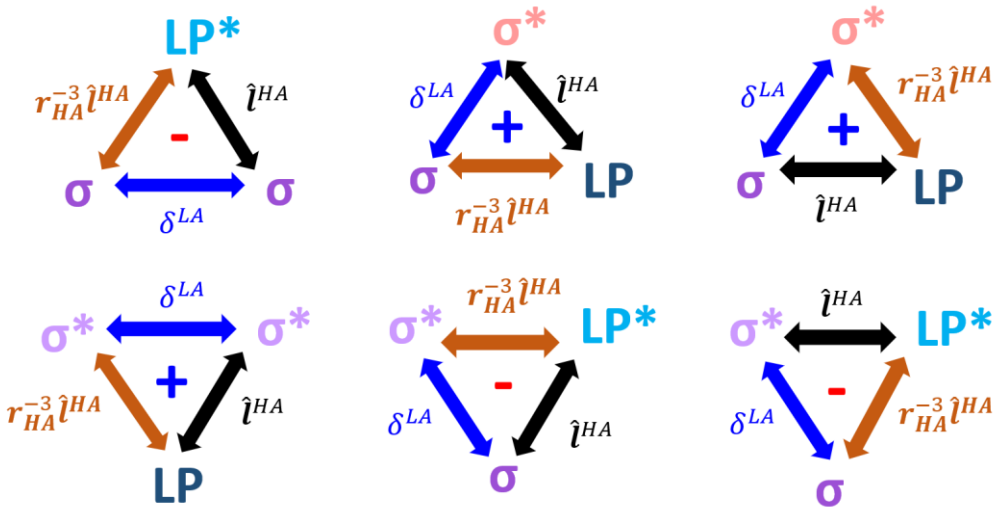

Figure 3: Schemes of $\boldsymbol{\sigma}^{SO/FC^{\Delta}}$and $\boldsymbol{\sigma}^{SO/FC^{\nabla}}$ coupling interaction in the form of triangles involving different orbital types (σ – dark purple, σ*- light purple, LP – dark blue, LP* - light blue). [18]

The sign of each orbital coupling triangle can be determined by analyzing the phase relationships in the PT3 expressions.[10, 17, 18] As the final values of the integrals are phase-invariant, the sign of the HA atomic orbital contributing to the bonding σ and antibonding σ* MOs can be fixed. Thus, the LA's AO will contribute with opposite signs to the $\sigma_{HA\text{-}LA}$ and $\sigma^*_{HA\text{-}A}$ MOs, resulting in a positive FC integral when σ orbitals are of the same type (i.e., both bonding or antibonding) and negative when both bonding or antibonding MO/MO* are involved. Second, integrals $\langle LP^x|\hat{\boldsymbol{l}}^{HA}|\sigma^{(*)}\rangle$ and $\langle LP^x|r_{HA}^{-3}\hat{\boldsymbol{l}}^{HA}|\sigma^{(*)}\rangle$ where LP^x is either LP or LP* will be of the same sign. Because these integrals are always paired, the corresponding

contributions from both the SO and angular momentum integrals are always positive. Finally, the FC operator couples only σ-type orbitals, which is not symmetry allowed for the SO operator. Please see our works on this topic for further clarification. [10, 17, 18]

There are two limiting cases of electronic configuration at the HA. The first case (Figure 4) depicts the system without occupied LP_{HA} MOs. This is characteristic of HA with formally empty valence shells, e.g., in d^0, p^0, or f^0 complexes. The second case (Figure 5) illustrates the situation where LP_{HA} is present, while LP^*_{HA} is absent, typical of heavy atoms with partially filled valence shells. Using the above-described reasoning, the sign of each respective $\sigma^{SO/FC}$ contribution can be determined for each combination of $\sigma_{HA\text{-}LA}$, $\sigma^*_{HA\text{-}LA}$, LP_{HA}, and LP^*_{HA}.

In systems with no occupied LP_{HA}, the three couplings involving LP_{HA} do not contribute, and all remaining couplings produce deshielding (Figure 4). In the alternative limiting case where the frontier LP_{HA} MOs are filled and LP^*_{HA} MOs are unavailable, the deshielding LP^*_{HA}-based couplings are not possible, and the remaining MO couplings result in shielding effects, see Figure 5. This is the case, for example, in $5p^4$ hydrides.

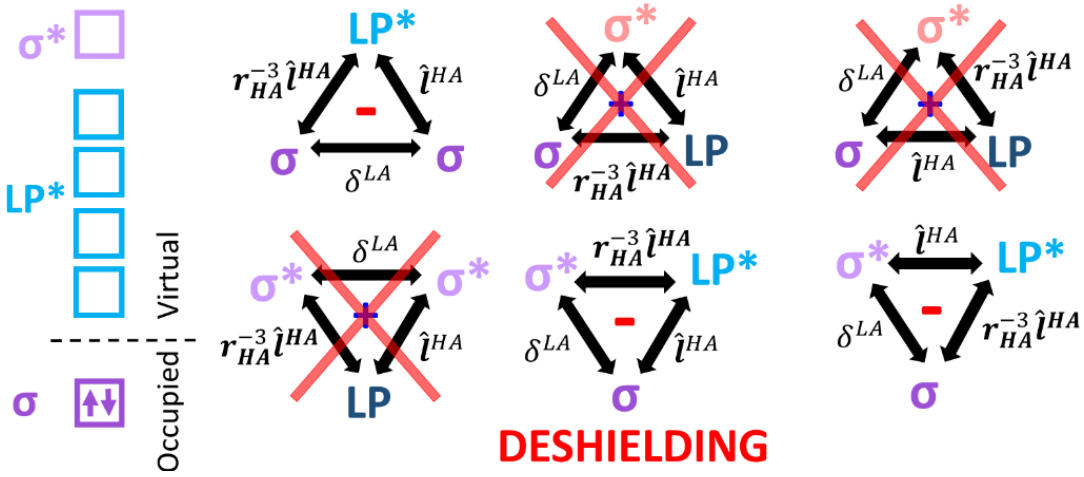

Figure 4: Schematic representation of $\boldsymbol{\sigma}^{SO/FC^{\Delta}}$ and $\boldsymbol{\sigma}^{SO/FC^{\nabla}}$ coupling triangles involving different orbital types (σ – dark purple, σ*- light purple, LP – dark blue, LP* - light blue) in a system without occupied LP_{HA} MOs. The electronic configuration at the HA is shown schematically on the left. Couplings that do not contribute are crossed out – note that only deshielding contributions remain.[18]

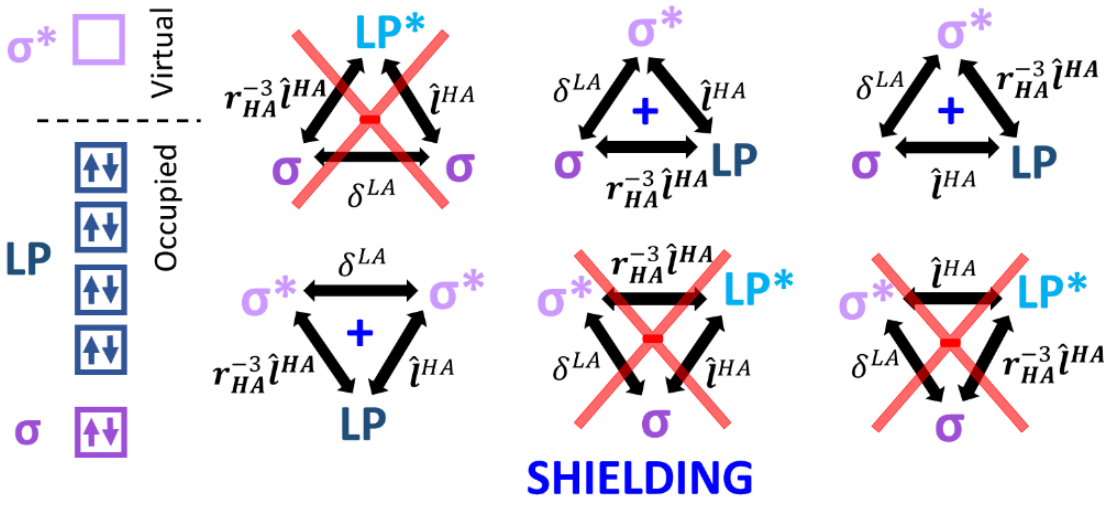

Figure 5: Schematic representation of $\boldsymbol{\sigma}^{SO/FC^{\Delta}}$ and $\boldsymbol{\sigma}^{SO/FC^{\nabla}}$ coupling triangles involving different orbital types (σ – dark purple, σ*- light purple, LP – dark blue, LP* - light blue) in a system with occupied LP_{HA} MOs. The electronic configuration at the HA is shown schematically on the left. Couplings that do not contribute are crossed out – note that only shielding contributions remain.[18]

In a general system, both mechanisms are present, and values of the $\delta^{SO/FC}$ (LA) are a product of the combination of these two coupling types. One may thus expect that the overall sign of $\delta^{SO/FC}$ (LA) would be difficult to determine without a detailed analysis. However, this is not the case. Because the overall size of $\delta^{SO/FC}$ (LA) is determined by the energy difference between frontier MOs and the overlap (symmetry) of MO/MO* couplings, couplings involving frontier orbitals are always dominant. Because LPs are non-bonding orbitals, they are high in energy, often forming the HOMO. On the contrary, the bonding σ-types orbitals are highly stabilized (low in energy). Hence, when at least one LP is present at HA, the $\delta^{SO/FC}$ (LA) is always shielding, because coupling involving LP has a very low energy denominator. The only exceptions to the rule are d^8 and d^{10} systems, where p-orbital admixture plays a role, and the overall sign of $\delta^{SO/FC}$ (LA) depends on the nature of the *trans* substituent, see Chapter 2.3. [10, 17, 18]

Moreover, in general complexes, more than one ligand is usually present. The MOs responsible for binding with ligands other than the NMR spectator atom LA contribute to the $\sigma^{SO/FC}$(LA) similarly to the LP_{HA} and LP^*_{HA} MOs, because they involve the same HA AOs types, which form LP. But their influence on $\sigma^{SO/FC}$(LA) is smaller than in non-bonding LPs, because admixture of other orbital types changes their shape and stabilizes their energy, resulting in higher energy denominators. [10, 17, 18] This is the reason why the highest δ^{SO}(LA) has been observed in low valence complexes (absence of other ligand binding orbitals). [10, 17, 18]

This detailed understanding of the PT3 mechanism enables qualitative prediction of SO-HALA effects based on the electronic structure of HA. It provides a powerful tool for interpreting and predicting relativistic NMR chemical shifts across diverse chemical systems. It explains periodic trends in heavy-element hydrides and extends to more complex molecular systems discussed in Part 2 of the thesis.

Part 2: Applications of Relativistic NMR calculations and analysis

This part outlines the factors influencing the propagation of SO-HALA effects and their practical applications, which are based on my works on this topic.[10–29] Let me also emphasize once again that these findings build upon the underlying theory laid out by Pyykkö, Kaupp, Malkin, and many others. Although I mainly performed calculations and analyses, the work is a product of collaboration with many other colleagues, without whose input these studies would not be feasible.

2.1 SO-HALA and Electronic Configuration of Heavy Atoms: The Lone-Pair Rule

The electronic configuration of the heavy atom represents one of the most fundamental factors determining both the magnitude and sign of SO-HALA effects at adjacent light nuclei. This principle, systematically established through extensive computational studies across the Periodic Table, has been codified into the "lone-pair rule", enabling understanding and predicting relativistic NMR effects based solely on the heavy atom's electronic configuration.

The theoretical foundation of the lone-pair rule emerges directly from the PT3 analysis of SO-HALA effects and is described in Chapter 1.5. Briefly, the presence or absence of occupied non-bonding orbitals (LP) at the HA fundamentally alters the dominant pathways for SO-HALA effect propagation. As shown in Chapter 1.5, the *HA with occupied LP* typically induces shielding σ^{SO}(LA), i.e., the negative chemical shift contributions at adjacent LA, through efficient $LP_{HA} \leftrightarrow \sigma^*_{HA\text{-}LA}$ coupling pathways. In contrast, *HA with formally empty valence shells* causes deshielding σ^{SO}(LA), i.e., the positive chemical shift contributions, via $\sigma_{HA\text{-}LA} \leftrightarrow LP^*_{HA}$ coupling mechanisms.[18]

The lone-pair rule has been extensively validated through a systematic study of heavy-element hydrides across the sixth period of the Periodic Table.[18] This study proved that the electronic configuration of heavy atoms from cesium to astatine causes predictable patterns in SO-HALA effects. We have thus established clear structure-property relationships that span the entire period and have several practical applications. The structures of the analyzed hydrides and their NMR chemical shifts are given in Figure 6, and the observed trends in $\delta^{exp}(^1H)$, $\delta^{calc}(^1H)$, and $\delta^{SO}(^1H)$ of hydride atoms across the 6th period are given in Figure 7.

For s-block elements, cesium and barium hydrides exhibit small deshielding SO-HALA effects at LA, even though s orbitals do not contribute to the SO coupling. This is caused by the admixture of 5d AOs into the bonding $\sigma_{HA\text{-}LA}$ MOs and the abundance of the low-lying empty 5d LP^*_{HA} MOs, allowing $\sigma_{HA\text{-}LA} \leftrightarrow LP^*_{HA}$ deshielding couplings, as shown in Figure 8.

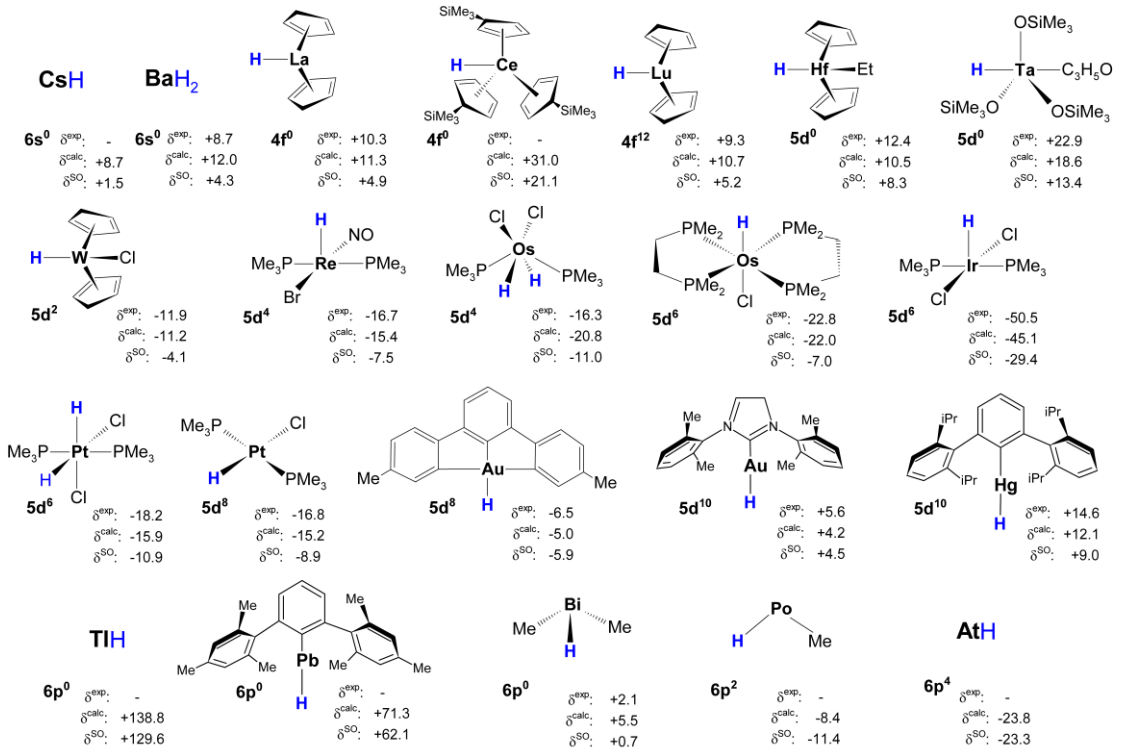

Figure 6: Structures and experimental, $\delta^{exp}(^1H)$, calculated total, $\delta^{calc}(^1H)$, and SO-HALA, $\delta^{SO}(^1H)$ NMR chemical shifts for investigated hydrides of 6th-period elements. [18]

The overall trends in $\delta^{exp}(^1H)$, $\delta^{calc}(^1H)$, and $\delta^{SO}(^1H)$ of hydride atoms across the 6th period and schematic electronic configuration at HA are shown in Figure 7, which reveals a wave-like dependence of chemical shifts, predominantly caused by $\delta^{SO}(^1H)$.

Moreover, during our study,[10] we have noted that the difference between the experimental $\delta^{exp}(^1H)$ values of CaH_2 (4.5 ppm) and BaH_2 (8.7 ppm) is 4.2 ppm,[10, 61] which is very similar to the difference between calculated $\delta^{SO}(^1H)$ in CaH_2 and BaH_2 (3.8 ppm). The SO-HALA effects are thus, somewhat unexpectedly, primarily responsible for the trend in $\delta^{exp}(^1H)$ of the second group hydrides. This explained the increasingly deshielding hydride resonances of the second group elements, a trend that puzzled the experimentalists for decades.[61] We have also hypothesized that these findings would be helpful in the development of advanced materials that use hydrides for charge transfer, such as the hydride-doped strontium mayenite, in which unexpectedly deshielded hydride resonances, not reproducible by scalar relativistic calculations, were observed.[62]

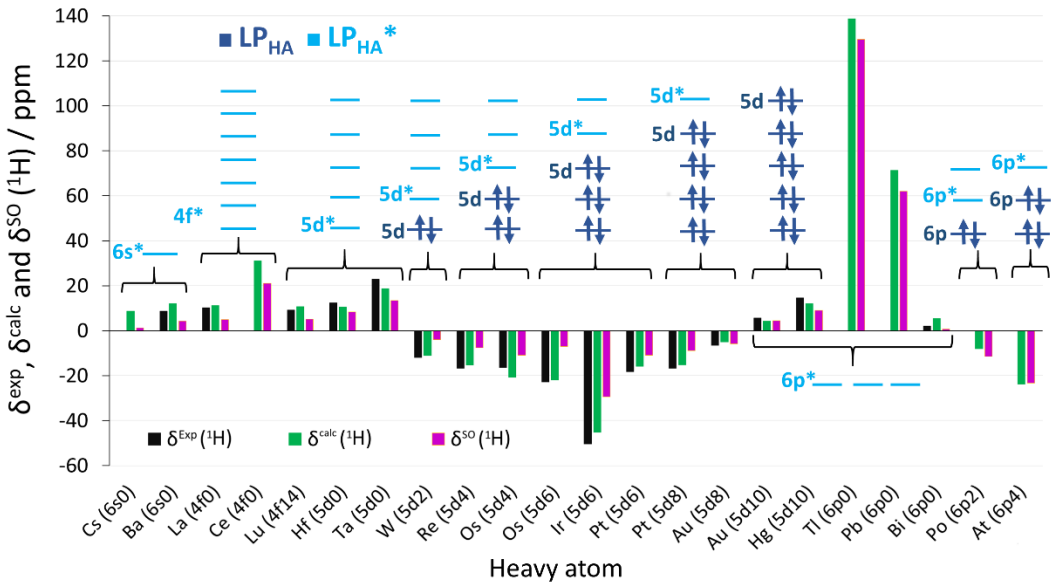

Figure 7: Trends in $\delta^{exp}(^1H)$ values (black), $\delta^{calc}(^1H)$ values (green), and $\delta^{SO}(^1H)$ values (magenta) across the 6th period. Schematics of the valence-shell electronic configurations of the HAs in their respective oxidation states are given above, with dark and light blue denoting LP_{HA} and LP^*_{HA}, respectively. [18]

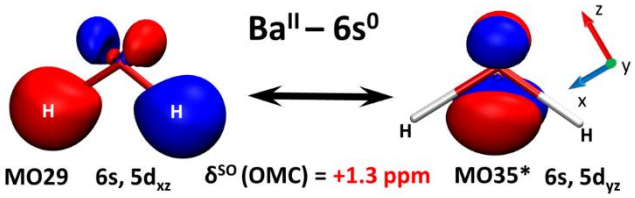

Figure 8: Selected $\sigma_{HA\text{-}LA} \leftrightarrow LP^*_{HA}$ deshielding coupling in a $6s^0$ Ba^{II} complex. [18]

The 6th-period transition metal series hydrides provide the most explicit demonstration of the lone-pair rule in action. Early transition metal hydrides with d^0 configurations of HA, such as hafnium(IV) and tantalum(V), exhibit strong deshielding $\delta^{SO}(^1H)$ at adjacent hydrogen nuclei. The empty 5d orbitals serve as efficient acceptors in $\sigma_{HA\text{-}LA} \leftrightarrow LP^*_{HA}$ coupling pathways, leading to positive chemical shift contributions that can exceed 13 ppm in Ta hydride, which is nearly the whole non-relativistic chemical shift range for ^1H nuclei.

As the 5d orbitals became filled, the situation immediately reverses, and the sign of $\delta^{SO}(^1H)$ inverts, due to activation of $LP_{HA} \leftrightarrow \sigma^*_{HA\text{-}LA}$ coupling pathways, which is favored due to smaller energy denominators compared to $\sigma_{HA\text{-}LA} \leftrightarrow LP^*_{HA}$ coupling (see Chapter 1.5). The tungsten(IV) hydride with its $5d^2$ configuration at HA is a prime example of this transition, resulting in negative total $\delta(^1H)$ values (see Figures 6 and 7).

In comparison, the tungsten(VI) hydride complex still features positive $\delta(^1H)$ values. Such a clear difference in $\delta(^1H)$ values depending on the oxidation number of the transition metal is highly advantageous, as it enables unambiguous detection of the metal's oxidation state by highly sensitive ^1H NMR even in complex environments. This may provide insights into reaction mechanisms and intermediate structures that are difficult to access through other spectroscopic methods. The unique relativistic signature of the ^1H shift may, for instance, serve as a reliable and straightforward probe for tracking changes in the electronic structure of transition metal complexes in catalytic or redox processes, where multiple species in different oxidation states may coexist, and traditional spectroscopic markers can be ambiguous or obscured.

The progression of shielding effects continues systematically through the 5d series element hydrides to $5d^8$ complexes, with maximum shielding effects observed for $5d^6$ configurations, particularly in iridium(III) complexes. Here, the square-pyramidal and octahedral ligand fields emphasize shielding $LP_{HA} \leftrightarrow \sigma^*_{HA\text{-}LA}$ couplings because the π-type metal 5d orbitals are filled first due to crystal-field influence.[26] Similarly, the vacant 6p* orbitals are still high in energy, which limits the presence of deshielding couplings. SO-HALA contributions can exceed -30 ppm for ^1H nuclei in $5d^6$ iridium complexes.[63]

The $\delta^{SO}(^1H)$ shielding then begins to diminish as the 5d shell approaches completion, with $5d^8$ and particularly the $5d^{10}$ systems like platinum(II) or gold(I) complexes showing intermediate effects that depend critically on coordination geometry and ligand field strength. The situation in these complexes is analyzed in detail in Chapter 2.3.

The deshielding $\delta^{SO}(^1H)$ is also present in the diamagnetic $4f^0$ and $4f^{14}5d^0$ lanthanide hydrides. For both La^{III} and Lu^{III} hydrides, the experimental and calculated ^1H chemical shifts are around +10 ppm, closely resembling those of $5d^0$ hydrides. Molecular orbital analysis confirms that the dominant shielding mechanism in these systems is $\sigma_{HA\text{-}LA} \leftrightarrow LP^*_{HA}$ coupling involving the 5d orbitals. In contrast, the Ce^{IV} hydride displays a markedly different behavior. The $\delta^{SO}(^1H)$ in Ce^{IV} hydride is +21.1 ppm, and $\delta^{CALC}(^1H)$ is + 31 ppm. This is significantly higher than other diamagnetic 4f-element hydrides and well beyond the conventional ^1H NMR range (~15 ppm). This may be why the Ce^{IV} hydride NMR chemical shifts have not been observed, despite compounds being known for several decades.[64]

An unusually high chemical shift in Ce^{IV} hydride stems from the involvement of Ce 4f atomic orbitals in bonding. The $\sigma_{Ce\text{–}H}$ bonding molecular orbital contains approximately 6% 4f character, in contrast to the <1% contribution in the $\sigma_{La\text{–}H}$ and $\sigma_{Lu\text{–}H}$ orbitals. This enables $4f \leftrightarrow 4f^*$ transitions within the $\sigma_{HA\text{-}LA} \leftrightarrow LP^*_{HA}$ coupling mechanism, significantly enhancing $\delta^{SO}(^1H)$ due to high 4f orbital angular momentum. This

mirrors the differences observed previously between Th^{IV} and U^{VI} hydrides: while Th^{IV} resembles a $6d^0$ element, U^{VI} has strong deshielding effects from $5f_0$ LP orbitals, resulting in "giant" SO-HALA effects.[65, 66]

The p-block elements best demonstrate the lone-pair rule's predictive power. Our studies of thallium(I) lead(II) compounds[13, 24] revealed that the $6p^0$ electronic configuration creates ideal conditions for extreme SO-HALA effects. The empty 6p* orbitals serve as highly efficient LP^*_{HA} acceptors, while the bonding 6p atomic orbitals have optimal energy and spatial characteristics for highly efficient coupling with 6p* counterparts. Calculations predicted ^1H chemical shifts exceeding 130 ppm for thallium(I) hydrides. These values extend beyond conventional NMR ranges for organic compounds and are the highest ever predicted in closed-shell compounds. The extreme SO-HALA effects in $6p^0$ complexes[13, 24] and the related discovery of lead(II) hydrides[67] are covered in Chapter 2.2.

The progression of $\delta^{SO}(^1H)$ through the p-block follows predictable patterns based on lone pair occupancy. Lead(II) compounds, with their $6s^2$ $6p^0$ configuration, show significant but somewhat reduced effects compared to thallium(I) due to larger energy denominators and the presence of another ligand. Bismuth(III) compounds, with a formal $6p^0$ configuration but significant ligand field effects, exhibit intermediate behavior where shielding and deshielding contributions nearly cancel. In polonium(II) and astatine(I) hydrides, the progressive filling of 6p orbitals leads to increasingly negative SO-HALA contributions, resulting in $\delta^{SO}(^1H)$ of -23 ppm in AtH. The illustration of the differences in selected orbital magnetic couplings between TlH and AtH, responsible for the opposing sign of $\delta^{SO}(^1H)$, is given in Figure 9.

The overall trend in $\delta^{SO}(^1H)$ of p-block elements regarding the configuration of heavy elements is schematically shown in Figure 10. Unlike 5d element complexes, the $\delta^{SO}(^1H)$ scales linearly with the number of vacant/occupied 6p orbitals.

To summarize, the lone-pair rule provides a first approximation that can be used to guess proper chemical shift ranges for LA in HA complexes, although there are several limitations. Orbital hybridization effects can significantly modify the $\delta^{SO}(LA)$, particularly in cases where p-orbital mixing is substantial, i.e., in d^8–d^{10} complexes. Crystal field effects represent another essential factor, particularly in transition metal complexes, where ligand field strength and symmetry can dramatically modify 5d orbital energies and occupations.

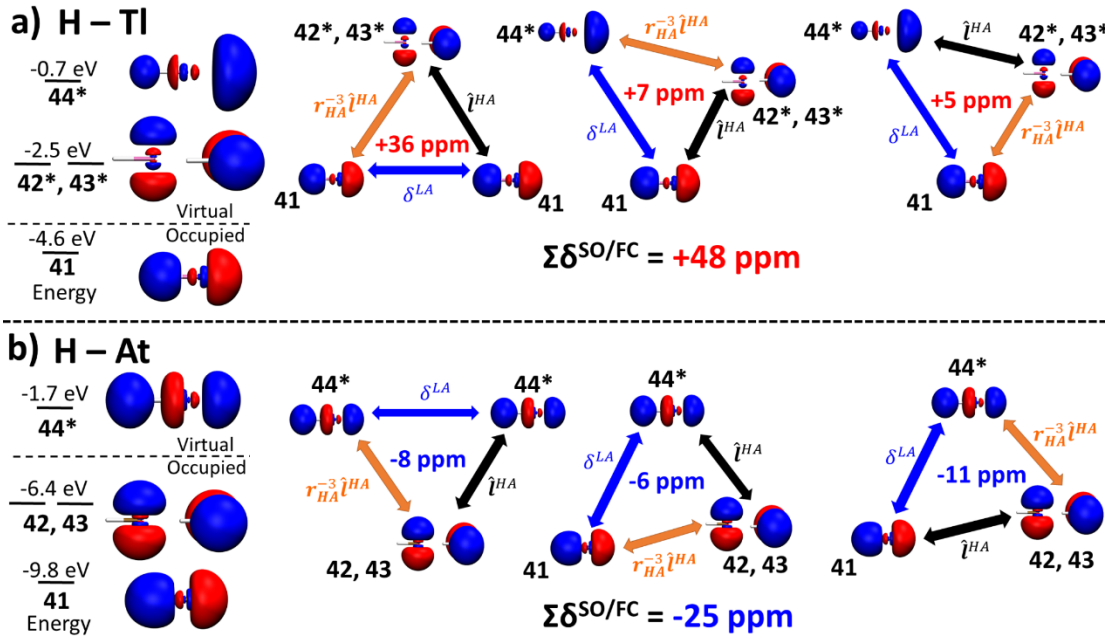

Figure 9: The PT3 orbital magnetic couplings in a) Tl^{I}H and b) At^{I}H in response to the SO coupling ($\boldsymbol{r}_{HA}^{-3}\hat{\boldsymbol{l}}^{HA}$), the Fermi-contact ($\delta^{LA}$), and the angular momentum operator ($\hat{\boldsymbol{l}}^{HA}$). [18]

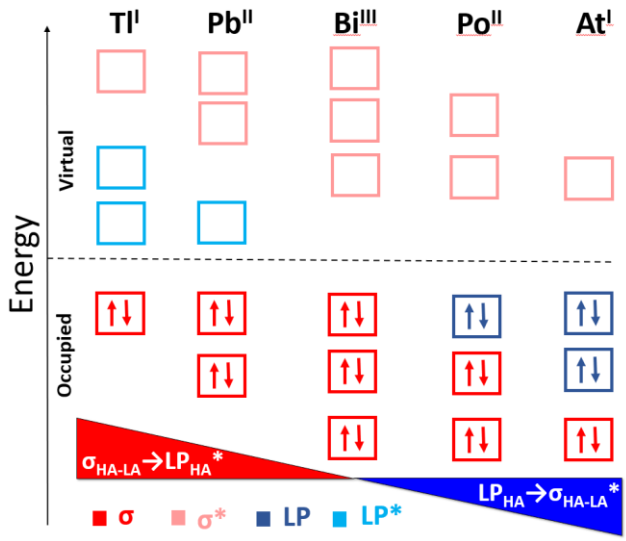

Figure 10: The schematic illustration of the dependence of δ^{SO}(LA) on the electronic configuration of HA in p-block elements. [18]

2.2 Pushing the Boundaries of NMR Chemical-Shift Ranges

My investigation of NMR chemical shifts in heavy-element compounds has revealed that the SO-HALA effects can be of sufficient magnitude to push light-atom resonances far beyond traditional boundaries, sometimes extending the observed ranges by a factor of two. The prime examples of this behavior can be found in my work focusing on Tl(I) and Pb(II) complexes.[13, 24]

2.2.1 High-Frequency Carbon and Silicon Chemical Shifts in Thallium(I) and Lead(II) Compounds

It has been observed in literature that NMR signals for ^{13}C and ^{29}Si in subvalent Tl(I) and Pb(II) organometallic compounds are often missing from NMR spectra or appear at remarkably deshielded positions, which lacked an explanation. Hence, we started to investigate the origin of unusually high-frequency NMR chemical shifts for LA directly bonded to low-valence thallium(I) or lead(II) metal centers.

We began by analyzing the differences between NMR chemical shifts of experimentally known full-valence M(IV) and low-valence M(II) compounds (M = Pb, Sn) of lead and tin, see Figure 11. While the ^{13}C NMR shifts in Pb(IV) and Sn(IV) compounds (**1** in Figure 11) are of conventional size (a few ppm), their Pb(II) and Sn(II) analogues (**2-5** in Figure 11) show considerable deshielding. In the tin compound **2a**, this deshielding is primarily due to an increase in the paramagnetic contribution to the chemical shift, with only a relatively small δ^{SO}(LA) of about +10 ppm. However, in the analogous lead(II) compound **2b**, the δ^{SO}(LA) is five times larger, reaching +52 ppm, and is the main reason for the much higher frequency shift than its tin counterpart. This trend continues in other compounds; for example, in Pb(II) compound **5**, the δ^{SO}(LA) to the ^{13}C shift reaches 126 ppm, accounting for the entire difference in the total chemical shift compared to the analogous Sn(II) compound. We concluded that deshielding in Sn(II) compounds is mainly a paramagnetic effect. However, the exceptionally high-frequency shifts in Pb(II) compounds are driven by the enormous SO contribution from the heavy lead atom.[24]

To place these findings in a broader context, we mapped the trends in relativistic effects on ^{13}C NMR shifts across a series of model complexes of the sixth-row elements in different oxidation states, obtaining similar trends to those formulated for the 6th period hydrides in Chapter 2.1.[24] Briefly, while the SO contributions were relatively small for transition metals and full-valence main group elements like Tl(III) and Pb(IV), typically between 10 and 30 ppm, there was a massive $\delta^{SO}(^{13}C)$ in the subvalent species of Tl(I) and Pb(II). For our model compounds, we calculated $\delta^{SO}(^{13}C)$ of +271 ppm for Tl(I) and +176 ppm for Pb(II), leading to predicted total ^{13}C chemical shifts of approximately 460 ppm and 360 ppm, respectively. The $\delta^{SO}(^{13}C)$ values are thus more than 15 times larger than in their full-valence counterparts and suggest

that the NMR signals for light atoms in some Tl(I) compounds may lie in a region above 400 ppm, well beyond the standard spectral window used in many experiments.

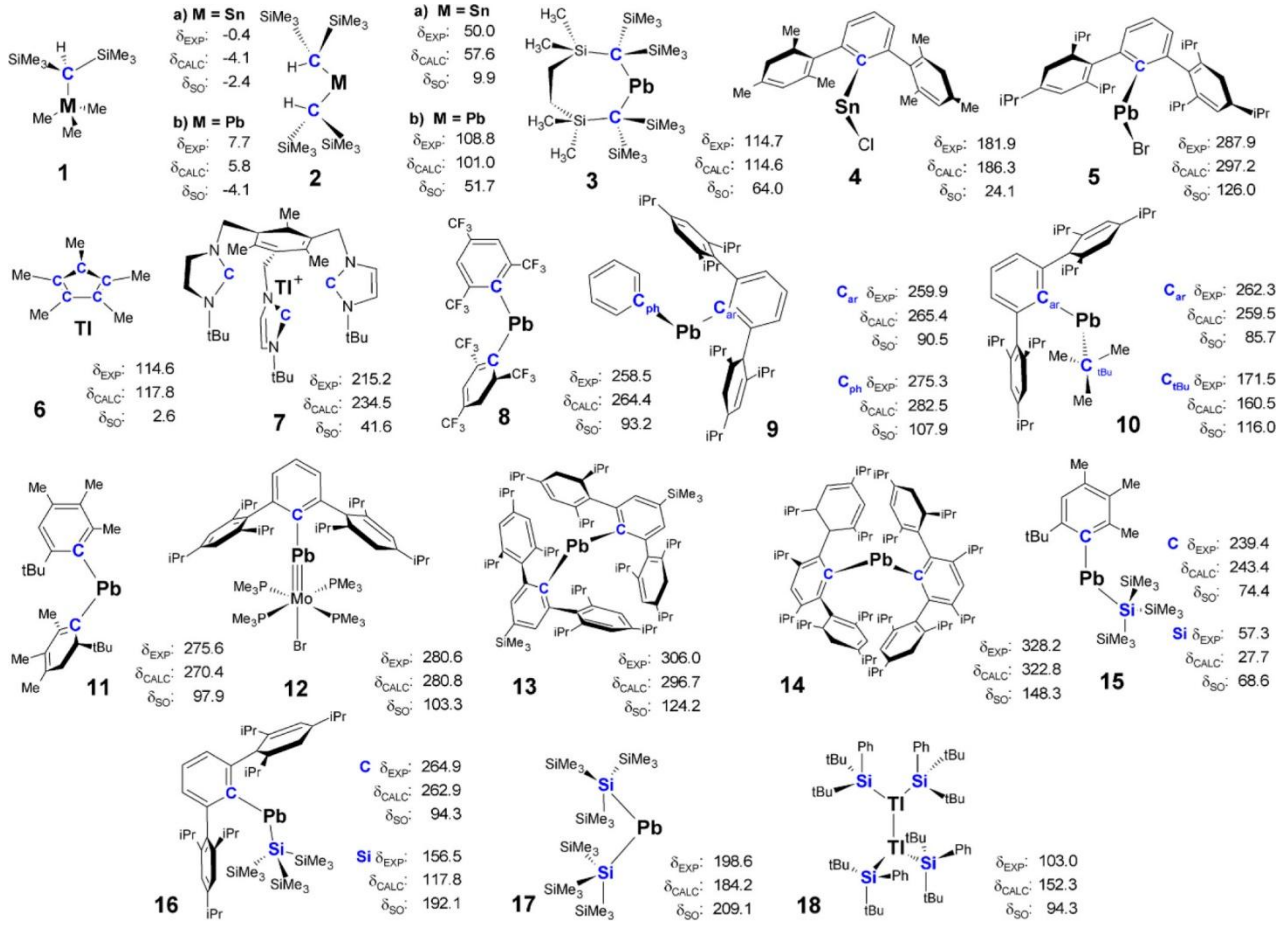

Figure 11: Structures of Sn^{II}, Sn^{IV}, Tl^{I}, Pb^{II}, and Pb^{IV} compounds with experimental (δ_{EXP}) and calculated (δ_{CALC} and δ_{SO}) ^{13}C and ^{29}Si NMR CS for the highlighted LA (in ppm). Me = Methyl, iPr = isopropyl, tBu = *tert*-butyl, Ph = phenyl. [24]

Hence, we used our calculations to predict the previously unassigned ^{13}C and ^{15}N NMR signals in several experimentally known Tl(I) and Pb(II) compounds, where NMR signals of atoms bound directly to HA were often conspicuously missing, see Figure 12.

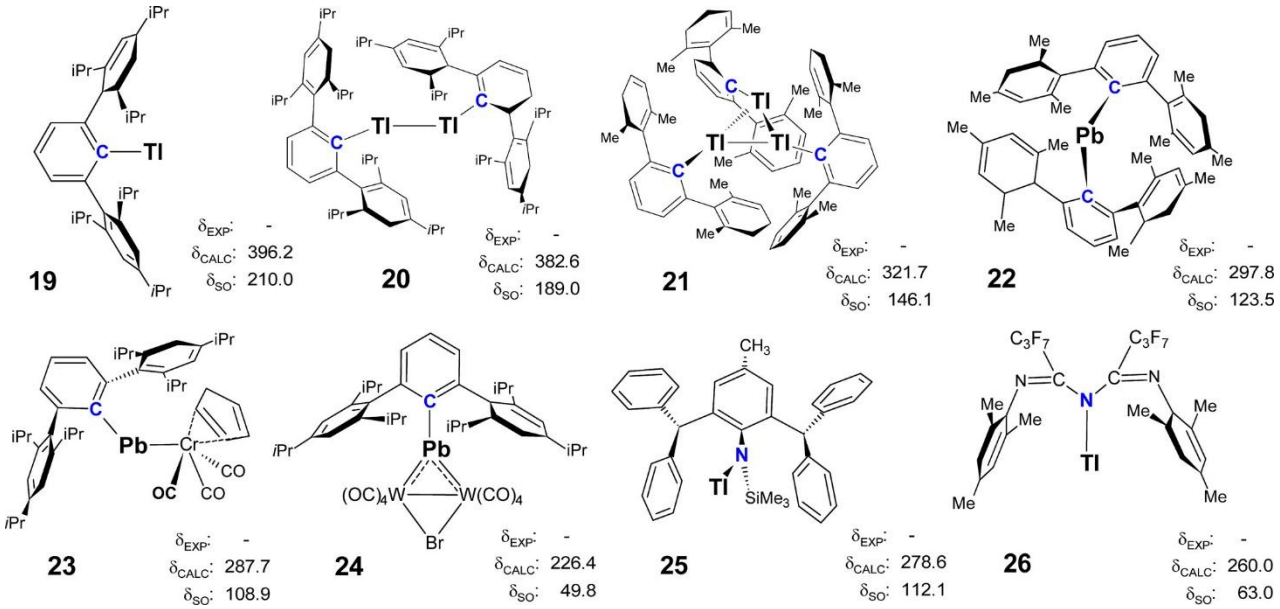

Figure 12: Structures of experimentally prepared Tl^{I} and Pb^{II} compounds where LA NMR chemical shifts were not reported. Me = Methyl, iPr = isopropyl, tBu = *tert*-butyl, Ph = phenyl. [24]

For two Tl(I) complexes with bulky terphenyl ligands, we predicted extremely high-frequency ^{13}C shifts of around 400 ppm and 380 ppm, caused by δ^{SO}(LA) accounting for more than 200 ppm, i.e., half of the total CS. Such values are unprecedented outside actinides, where orbitals with much higher angular momentum are involved.[66]

We also investigated the influence of structural factors on δ^{SO}(LA) using the complete set of investigated compounds. We have noted that the magnitude of the SO-HALA effect is highly sensitive to the coordination number of the central heavy atom. For instance, a tri-coordinated Tl(I) compound **7** shows a much smaller δ^{SO}(LA) of only +42 ppm. Interestingly, in clusters with direct Tl-Tl or Pb-Pb bonds, the SO effect remains large, which we attribute to the weak metallophilic interactions that do not significantly occupy the vacant 6p orbitals necessary for the large SO effect. The nature of the atom bonded to the metal is also critical. We found that the SO contribution to ^{15}N shifts in Tl-N bonds is smaller than for Tl-C bonds, which we attribute to the lower covalency of the Tl-N bond, confirming that the propagation of SO effects is strongly linked to the covalence of the HA-LA bond, which is discussed in Chapter 2.3.

Our investigation of ^{29}Si NMR shifts revealed even more dramatic effects. For a known lead silyl compound, we predicted a ^{29}Si shift of +360 ppm, driven by an SO contribution of +359 ppm, a value considerably larger than any reported for similar compounds. We have noted that the ^{29}Si resonance in this compound was likely misassigned in the original experimental work. [68]

Since mono-coordinated Tl(I)-silyl compounds are rare, we have prepared a series of model complexes. Our calculations predict unprecedentedly high-frequency δ(^{29}Si), ranging from 380 ppm to 1100 ppm, depending on the substituents on the silicon atom. For one of the Tl(I) complexes, we even predict a δ(^{29}Si) = 666 ppm, almost entirely caused by a massive SO contribution of 670 ppm. We have also found a strong linear correlation between the predicted SO contribution and the HOMO-LUMO energy gap of the molecule, which is modulated by the nature of the ligands. The future experimental searches for Tl(I)-silyl compounds should thus utilize significantly expanded ^{29}Si NMR spectral windows.

Finally, we analyzed the electronic origin of these giant SO effects. The large δ^{SO}(LA) arises from highly efficient magnetic couplings between occupied and virtual molecular orbitals, specifically those involving the heavy atom's 6p orbitals (6p → 6p* coupling), see Figure 13 for examples.

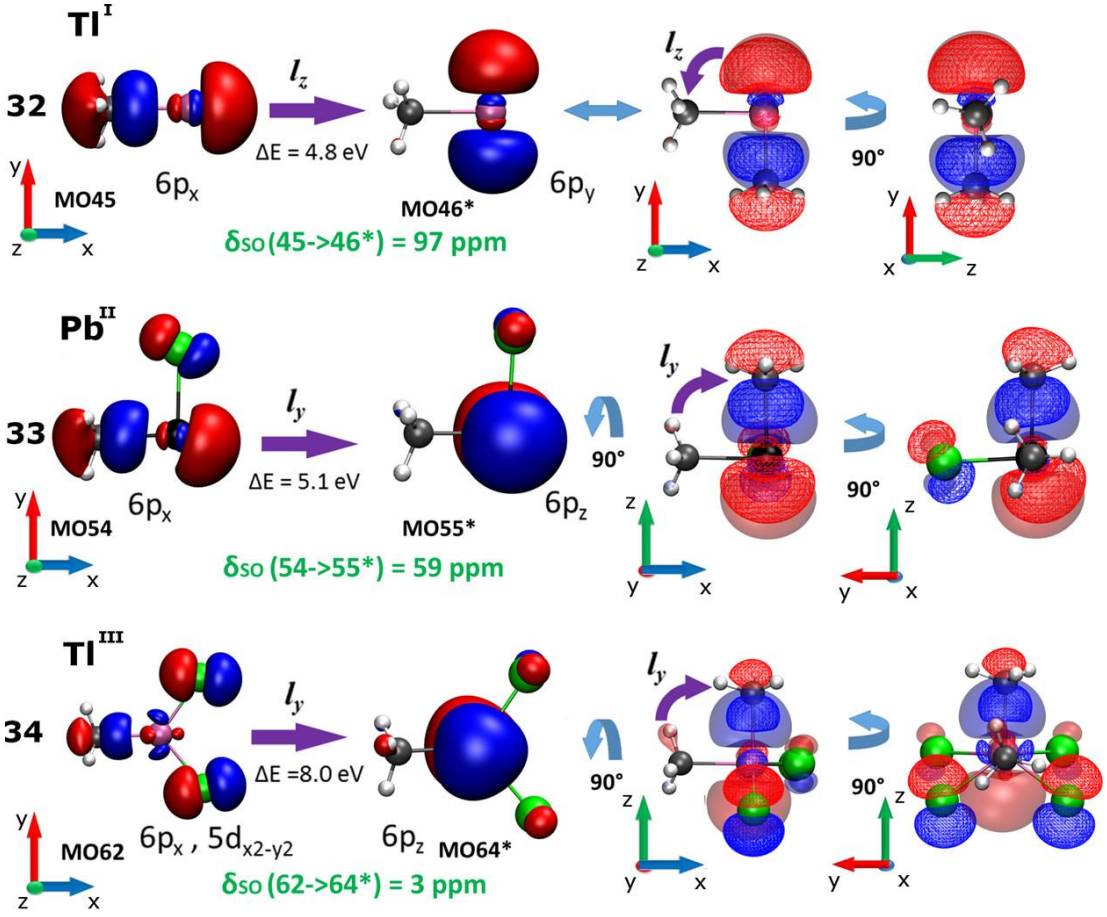

Figure 13: Selected orbital magnetic couplings for Tl(I), Pb(II), and Tl(III) complexes, with corresponding δ^{SO}(LA), Δ*E*, and MO composition and schematic illustrations of the MO → MO* overlap. [24]

Briefly, the giant size of the SO-HALA effect in subvalent Tl(I) and Pb(II) compounds is caused by the very low energy gap between occupied and vacant 6p orbitals, combined with a very high efficiency of their overlap due to highly similar orbital shapes. In contrast, in full-valence Tl(III) and Pb(IV) compounds, the 6p orbitals are more involved in bonding with other ligands and undergo hybridization, which distorts their shape and reduces their availability for these specific magnetic couplings, thus dramatically reducing the δ^{SO}(LA). Interestingly, the unique electronic structure of subvalent Tl(I) and Pb(II) compounds results from the inert-electron pair effect, in which the occupied $6s^2$ orbital is stabilized by the scalar relativistic effects. Scalar relativistic effect is thus an indirect cause of the massive SO effects, and the resulting high-frequency NMR shifts we have predicted.

After presenting these findings at an international conference, Prof. Siemeling invited me to work on a newly prepared N-heterocyclic plumbylene capable of activating C-H bonds. [23] This study investigated the synthesis and reactivity of an N-heterocyclic plumbylene featuring a ferrocenediyl backbone and trimethylsilyl substituents. NMR analysis of the plumbylene revealed a ^{207}Pb NMR signal at an unusually high-field chemical shift of 2550 ppm. This value was unexpected for a dicoordinate lead(II) atom and more typical of a tricoordinate lead species, suggesting that an additional interaction stabilized the electrophilic Pb(II) center. This hypothesis was confirmed by an X-ray crystal structure, which showed a short intramolecular Fe···Pb bond. Removing a Lewis base from the plumbylene generated a second, less stable complex, with a ^{207}Pb NMR signal at 4333 ppm, a chemical shift characteristic of dicoordinate diaminoplumbylenes. However, further NMR studies showed that this monomeric plumbylene was not stable in solution and undergoes a reversible equilibrium with a novel, unsymmetrical dimeric plumbylene, having ^{207}Pb NMR signals at 3764 ppm and 2853 ppm, corresponding to two chemically inequivalent lead atoms.

1D and 2D NMR experiments were performed to map out the connectivity of the dimer. As it turned out, a formation of the dimer involves the cleavage of a C–H bond and the formation of new Pb–C and N–H bonds. This is highly interesting, as the aromatic C-H bond is very stable. Its breaking indicates a rather unique catalytic potential of this compound. To conclusively verify the structural assignment, fully relativistic ^{13}C, ^{15}N, and ^{207}Pb NMR chemical-shift calculations were employed, using a methodology I have specifically optimized for NMR calculation of lead(II) compounds. The computed chemical shifts were in excellent agreement with experimental data, confirming the proposed structure of dimer plumbylene. The ^{13}C NMR signal at 182 ppm was thus confirmed to belong to the carbon atom directly bonded to lead, as evidenced by a large δ^{SO} (^{13}C) contribution of 100 ppm. On the contrary, the δ^{SO} values for bound nitrogen atoms were only about nine ppm in both cases, which implies only a small degree of covalency (see Section 2.3). This

is unsurprising as both nitrogen atoms share their electrons with two lead atoms simultaneously. These findings were published in a prestigious *Angewandte Chemie* journal. [23]

Although our work on ^{13}C species provided a fascinating insight into the structure and properties of these exotic molecules, there is another class of compounds, in which the δ^{SO}(LA) plays an even more crucial role: the lead(II) hydrides.

2.2.2 The quest for lead(II) hydrides

Our following study investigated the ^{1}H NMR chemical shifts of tin(II) and lead(II) hydrides using 4c DFT. Our work aimed to quantify and to understand the role of relativistic effects and to predict the spectral ranges for Pb(II) hydrides, which have not yet been experimentally characterized, despite serious efforts spanning several decades.[13]

Before predicting the NMR properties, we evaluated the thermodynamic stability of various possible isomers of dimeric Pb(II) hydrides with the general formula $(RPbH)_2$. We considered four central structural motifs proposed for group 14 dimeric hydrides earlier, see Figure 14.

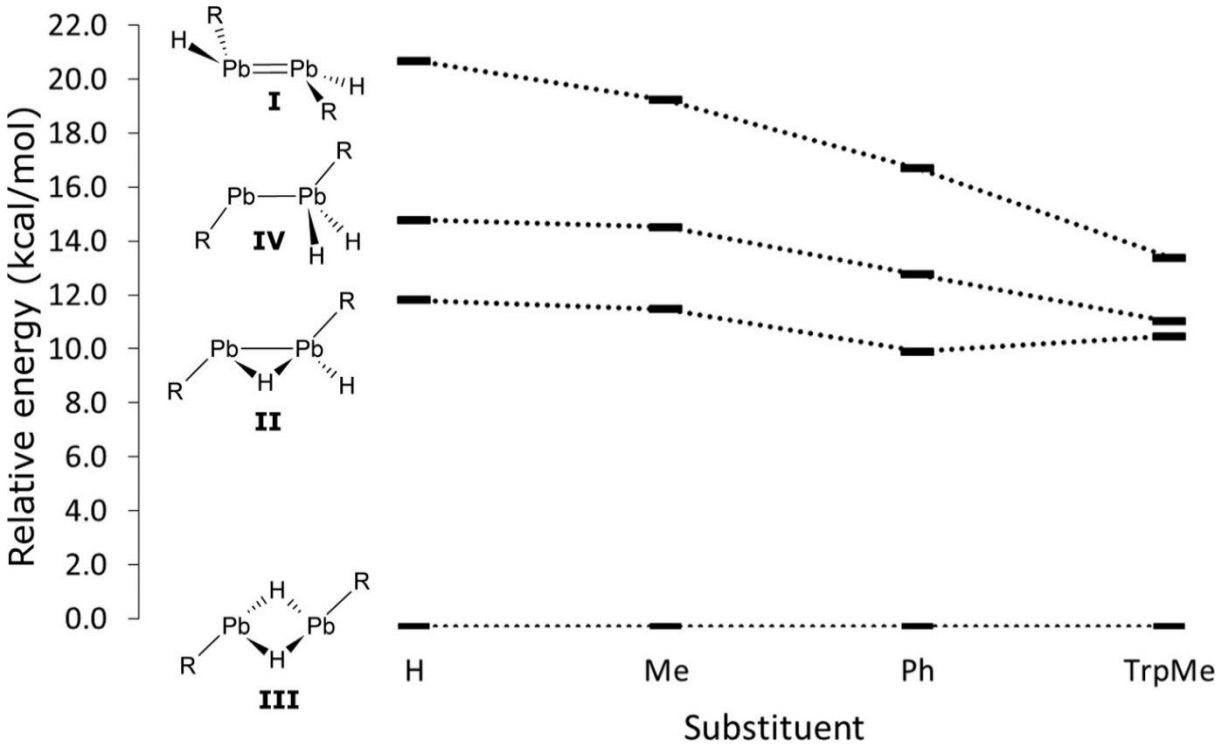

Figure 14: Relative energies of Pb^{II} dimeric hydrides $(HPbR)_2$ for different ligands R = H, Me (methyl), Ph (phenyl), TrpMe (C_6H_3-2,6-(C_6H_2-2,4,6-$(CH_3)_3)_2$).[13]

Our calculations revealed that the μ-H-bridged structure, or isomer III in Figure 14, is the most stable Pb(II) hydride. This finding held regardless of the size of the ligand (R) we tested, which ranged from a simple proton to a large terphenyl group. Other isomers were found to be considerably less stable; for instance, with the large TrpMe ligand, isomers II and IV are predicted to be about +11 kcal/mol higher in energy than isomer III, while isomer I is even less stable. The high stability of hydrogen-bridged isomer III correlates with its largest HOMO-LUMO energy gap, suggesting greater kinetic stability. Based on these results, we concluded that the hydrogen-bridged structure is the most likely conformation to be adopted by any dimeric Pb(II) hydride that may be synthesized.

A central part of our work was predicting the ^{1}H NMR chemical shifts for a range of possible Pb(II) hydrides, as these may fall outside of standard spectral regions, and our calculations aimed to guide future experimental searches. The 4c calculations revealed that the ^{1}H NMR resonances of hydride atoms in these Pb(II) compounds should appear in a high-frequency region between 14 ppm and 90 ppm, with most signals between 30 and 60 ppm, see Figure 15. The signal of the most stable isomer III falls to 31 ppm.

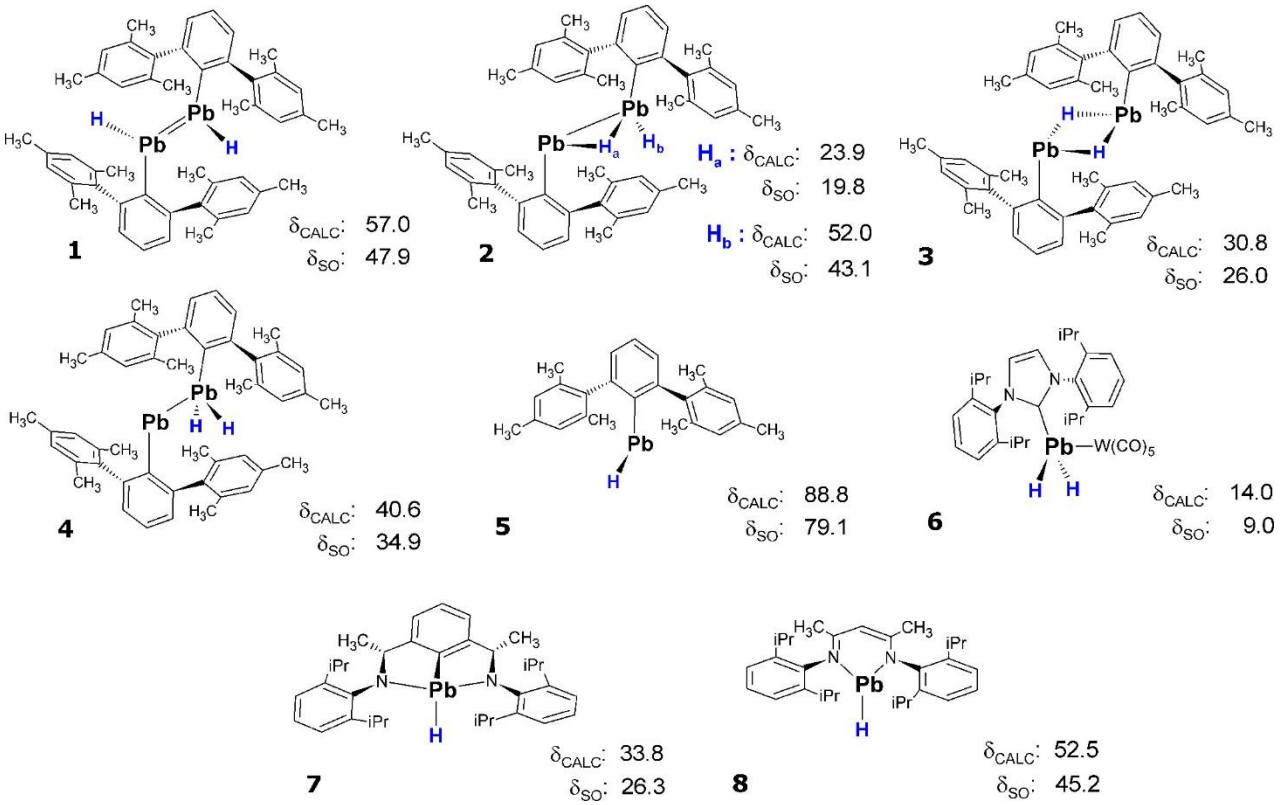

Figure 15: Structures of possible Pb^{II} hydrides **1–8** and their δ_{CALC}(^{1}H) and δ_{SO}(^{1}H). iPr = isopropyl.

This is a significant difference from the known ^{1}H NMR chemical shift ranges of sixth-period hydrides, which were found to resonate between -60 ppm and +25 ppm at that time. We found that, once again, the origin of these exceptionally high-frequency shifts is the large $\delta^{SO}(^{1}H)$, which can be as large as +80 ppm.

Hence, we concluded that the likely reason why these species have not been detected in reaction mixtures where their presence was suspected may be their unusually high NMR chemical shifts. We therefore suggested that experimentalists searching for new Pb(II) hydrides should explore high-frequency ^{1}H NMR spectral regions up to 100 ppm.

Furthermore, we discovered a strong correlation between the molecular structure of the Pb(II) hydrides and their ^{1}H NMR chemical shifts, indicating that ^{1}H NMR could be a powerful tool for structural elucidation. Essentially, the $\delta^{SO}(^{1}H)$ contribution in the hydrides, and by extension their total chemical shift $\delta(^{1}H)$, is highly sensitive to the coordination number of the central lead atom. For monomeric species, the $\delta^{SO}(^{1}H)$ decreases as the coordination number of the lead atom increases. The most significant shifts are thus predicted in the least stable two-coordinate Pb(II) compounds, such as compound **5** in Figure 15 with $\delta(^{1}H)$ near 90 ppm, because its vacant Pb 6p* atomic orbital does not participate in bonding. When the coordination number increases to three or four, this vacant orbital becomes involved in bonding with ligands, reducing its availability for the magnetic couplings responsible for the significant SO-HALA effect and thus dramatically reducing the chemical shift.

To further support our findings, we performed the same evaluation on a series of experimentally known Sn(II) hydrides, which allowed us to compare our results with existing experimental data. Although the observed $\delta^{SO}(^{1}H)$ values were only between 1 and 7 ppm in Sn(II) hydrides, about seven times smaller than in the analogous Pb(II) compounds, the magnitude of the SO effect in Sn(II) hydrides was indeed modulated by the coordination number of the tin atom in the same way as in lead analogs. The largest SO contributions are found in two-coordinated species where the vacant Sn 5p* orbital is fully available for magnetic couplings; this contribution decreases as the orbital becomes involved in coordination bonding in three- and four-coordinated compounds. Given this sensitivity, we proposed that the $\delta(^{1}H)$ of lead and tin hydrides can serve as an effective "probe" for studying the electronic and topological structure of these compounds.

The study on lead(II) hydrides received highly positive feedback from the experimental community. I was very pleased that, less than six months after the publication of this work, the first lead(II) hydride was synthesized by Wesemann's group.[67] In their work, Wesemann et al. report the first isolation and characterization of a low-valent organolead(II) hydride. In agreement with our prediction, the synthesized

hydride was of the dimeric μ-H-bridged structure. Wesemann also observed a ^{1}H NMR signal for this μ-H-bridged organolead hydride at 31.1 ppm in the solid state, which represents the lowest field (most deshielded) ^{1}H NMR chemical shift ever recorded for a diamagnetic compound to date. This extremely low-field shift also agrees with my prediction for the μ-H-bridged organolead hydride (30.8 ppm), which turned out to be only 0.3 ppm away from the experimental value. [13] Our theoretical work thus paved the way for discovering a new class of compounds.

2.3 The Nature of Heavy Atom-Light Atom Bond: Covalency and Trans Effect

In this chapter, I will delve into the intricate relationship between the character of the HA-LA bond and the δ^{SO}(LA) in various transition-metal systems, including d^6 iridium(III) and platinum (IV), d^8 platinum(II) and gold(III), and d^{10} gold(I) and mercury(II) complexes.[17, 25, 26, 29]. I will describe why is the nature of the HA-LA chemical bond—specifically its covalency and the influence of the chemical environment, such as the *trans* effect—a primary determinant for both the magnitude and the sign of the δ^{SO}(LA) and how can δ^{SO}(LA) serve as a reliable NMR spectroscopy probe to analyze the nature of the HA-LA bond and structure of heavy element complexes in general. Note that my works in this chapter are presented chronologically to illustrate the development of knowledge about the electronic structure and δ^{SO}(LA) relationship.

The initial study on d^6 iridium(III) complexes[26] was inspired by an incidental discovery of what was later known as the "SO trans effect" during our DFT validation and benchmarking study on d^6 iridium(III) and platinum (IV) complexes, discussed in Chapter 1.4.[29] During the validation, some DFT functionals performed poorly in describing the Ir-S bond in Ir(III) complex, which was in the trans position to NMR spectator atom N9 of the purine ligand, see Figure 16. The difference in the Ir–S interatomic distance between structures optimized with different methods was as large as 8.6 pm. This relatively minor structural variation led to a substantial difference of approximately 11 ppm in the calculated ^{15}N NMR chemical shift for the N9 atom. Even the small change in *trans* position thus considerably influenced the NMR CS at he opposite ligand, and, more importantly, the SO-HALA effect.

To systematically probe this dependency, we performed a series of calculations where we constrained the Ir–S distance at different lengths between 2.13 and 2.38 Å and allowed the rest of the molecule to relax. [29] This revealed an expected linear dependence of the ^{15}N NMR chemical shift of N9 on the Ir–S bond length. However, after decomposing the total chemical shift into its SR and SO contributions, we found that elongating the Ir–S bond by 25 pm altered the scalar-relativistic chemical shift by only about six ppm. In contrast, the SO contribution changed by a remarkable 24 ppm. The modulation of the SO coupling is thus the predominant cause of the trans ligand effect on δ(LA) in heavy element complexes.

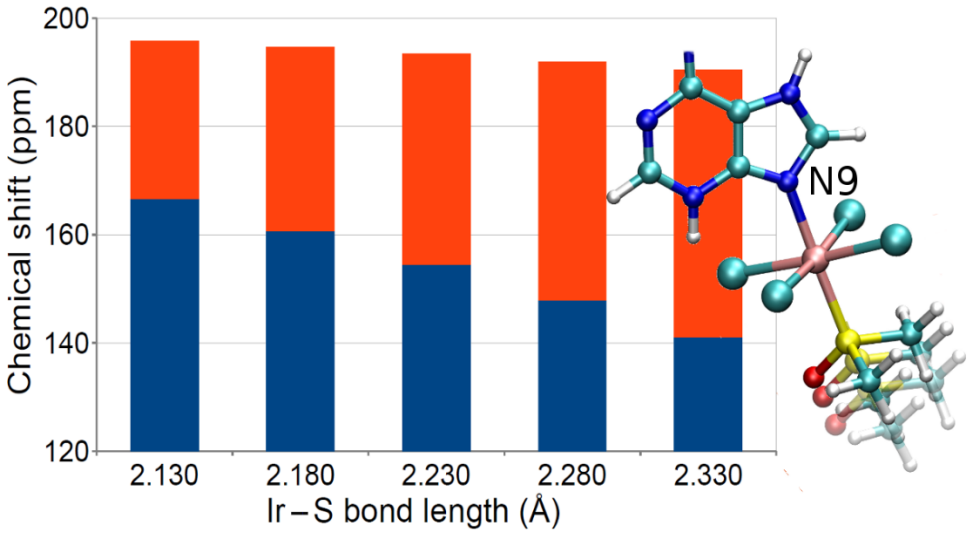

Figure 16: ^{15}N NMR chemical shift of N9 upon stretching the Ir–S bond. The δ^{SO} is coded in orange. [29]

Inspired by these findings, we have started more systematically investigating the mechanism and magnitude of SO-HALA effects on a series of d^6 iridium(III) complexes. [26]

Focusing on the axially coordinated nitrogen atom (N9) in a model octahedral iridium complex, we systematically modulated the electronic structure by stretching the Ir–S bond as in a previous study, and also by changing the trans ligand entirely. The composition of both Ir-S and Ir-N9 bonds in these complexes was analyzed. Relativistic DFT SO-ZORA calculation confirmed that δ^{SO}(LA) at N9 is highly sensitive to changes in the bonding environment, with values ranging from about 30 to 55 ppm as the Ir–S bond is lengthened. According to Kaupp et al., the size of δ^{SO}(LA) depends on the s-character of LA in the HA-LA bond and the energy gap between occupied and virtual molecular orbitals (MOs).[31] However, our results show that the s-character of the N9 atom in the Ir–N bond remained constant throughout these structural changes, indicating that other factors must be responsible for the observed modulation of δ^{SO}(LA).

Through detailed molecular orbital (MO) analysis, employing both PT2 (SO-ZORA) and sum-over-states third-order finite perturbation theory[58], we demonstrated that the key contributors to δ^{SO}(LA) are a small set of "δ^{SO}-active" MOs with significant iridium 5d-orbital character. The changes in δ^{SO}(LA) upon structural modification in the trans position were directly proportional to changes in the 5d-character of these occupied and virtual MOs. While energy gaps between MOs play a role, the sign and magnitude of δ^{SO}(LA) modulation are more closely tied to the 5d-orbital participation in the relevant MOs. To generalize these insights, we extended the analysis to a broader set of iridium complexes with various sulfur- and oxygen-based trans ligands. We observed a nearly perfect correlation between the d-character of the Ir–N

bond (as quantified by NBO analysis) and the calculated δ^{SO}(LA) at N9, regardless of the specific ligand employed, see Figure 17.

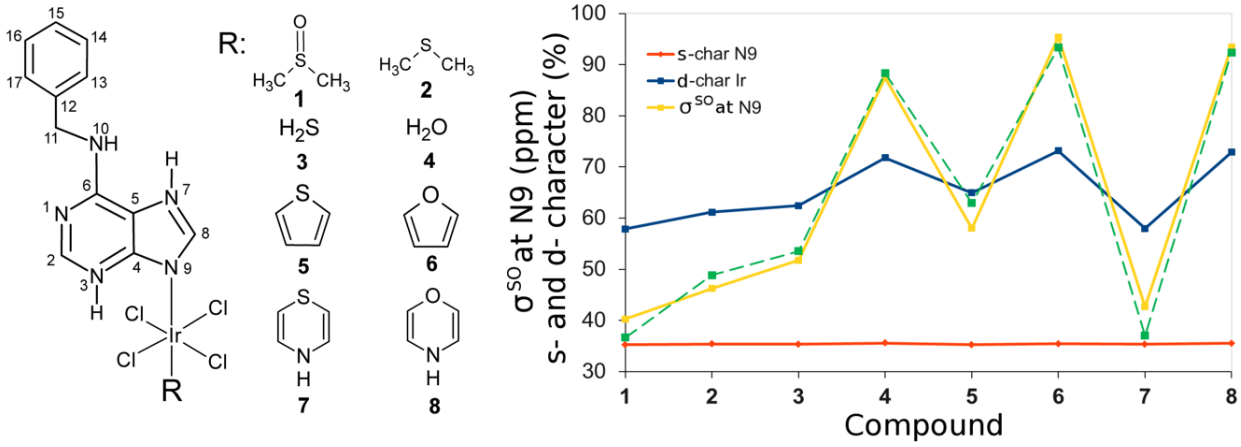

Figure 17: Structures of analyzed complexes (left) and dependence of σ^{SO}, s-orbital character of N9, and 5d orbital character of Ir in the Ir-N9 bond. The dashed green line represents the 5d character of Ir scaled to the range of σ^{SO} values to illustrate the correlation better.

This led us to propose the "Bonding D-Character" (BDC) approach, which enables the prediction of SO-induced NMR shifts in related complexes based solely on the metal d-character in the bonding orbital and *vice versa*. The predictive accuracy of this approach is within a few ppm, even for structurally diverse systems. To the best of my knowledge, this was the first work using the exact AO composition of HA MO to explain the SO-HALA effect propagation. The results also indicated that a direct and even more general structure and δ^{SO}(LA) relationship may exist and could be used as a HA-LA bond descriptor.

Hence, in the subsequent study,[25] we set out to perform more detailed analysis of the electronic factors responsible for the magnitude and sign of δ^{SO}(LA) in square-planar platinum(II) and gold(III) complexes with 2-phenylpyridine ligands, which display striking differences in δ^{SO}(LA) of directly bonded nitrogen and carbon atoms in response to the *trans* ligand.

Using DFT SO-ZORA calculations, we calculated δ^{SO}(LA) for the nitrogen and carbon atoms directly bonded to platinum and gold. We found that platinum complexes exhibit large, shielding δ^{SO}(LA), while gold complexes show much smaller or even deshielding δ^{SO}(LA). For example, the calculated δ^{SO}(LA) for the nitrogen atom in a platinum complex was around -34 ppm, compared to +18 ppm in a similar gold complex. These differences could not be explained by changes in the s-character of the light atom, which remained nearly constant across the series, and only partly by the involvement of d-orbitals.

According to molecular orbital (MO) analysis, the SO-active MOs in platinum complexes are primarily metal-centered 5d orbitals (LP). The efficient magnetic couplings between these 5d orbitals and their unoccupied 5d* partners (5d → 5d*), which correspond to $LP_{HA} \leftrightarrow \sigma^*_{HA\text{-}LA}$ coupling type, are responsible for the significant and positive (shielding) SO contributions observed in platinum complexes. In contrast, the SO-active MOs in gold complexes often have substantial 6s and 6p character. The dominant magnetic couplings thus become 6p → 6p* and are deshielding as they belong to the $\sigma_{HA\text{-}LA} \leftrightarrow LP^*_{HA}$ coupling family, see Figure 18.

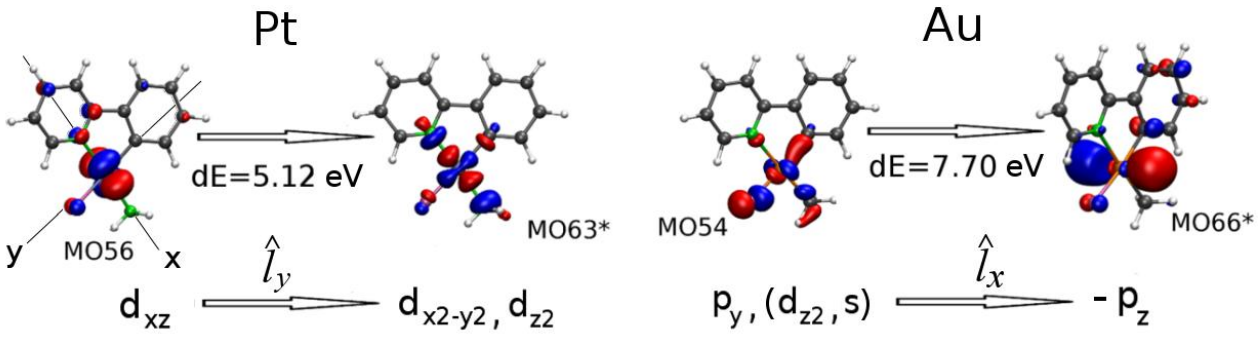

Figure 18: Selected MO→MO* magnetic couplings in Pt and Au compounds, corresponding energy differences dE, and schematic compositions of MOs involved. Selected Pt MO→MO* magnetic coupling contributes by - 25 ppm to δ^{SO}(LA), while Au MO→MO* magnetic coupling contributes by + 9 ppm. [25]

We reasoned that this difference in orbital composition is rooted in fundamental scalar relativistic effects. The 6s and 6p orbitals in gold are more stabilized (Figure 19) and thus more chemically accessible than in platinum due to a more substantial scalar relativistic effect and higher nuclear charge of Au, leading to a different bonding scenario. In other words, the bonding in platinum complexes is dominated by 5d orbitals, while in gold complexes, the admixture of 6s and 6p orbitals plays a much greater role. This shift in bonding character directly modulates the δ^{SO}(LA) sign. Clearly, the description relying solely on the d-character may not be valid for late-transition metal elements, as mentioned in Chapter 2.1.

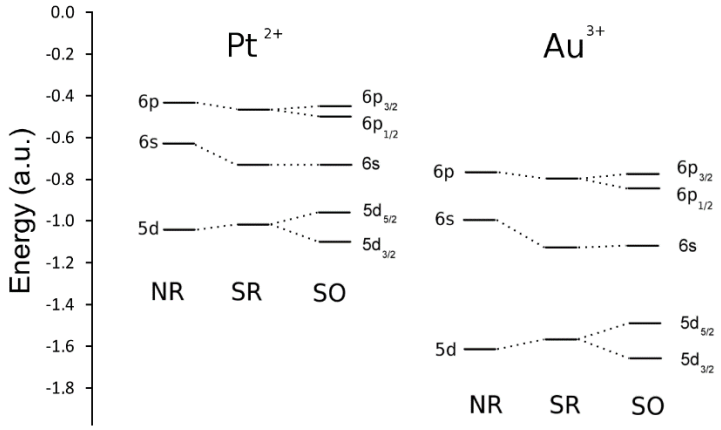

Figure 19: Atomic orbital energies in Pt^{2+} and Au^{3+} ions at non-relativistic (NR), scalar-relativistic (SR), and Spin-Orbit (SO) levels. [25]

Hence, to further generalize the relationship between electronic structure and SO-HALA effects, we analyzed the covalence of the metal–ligand bond using the delocalization index (DI) from the Quantum Theory of Atoms in Molecules (QTAIM) analysis [25]. We found a strong quantitative correlation between the magnitude of σ^{SO} at the light atom and the DI of the metal–ligand bond. The more covalent the bond (i.e., the greater the electron sharing between metal and ligand), the larger the SO-induced shielding. By scaling the DI with the light atom's electronegativity, we unified the correlation across different types of bonds, ligands, and metals, suggesting that this approach could be a general predictor of SO-HALA effects in heavy-element systems, see Figure 20.

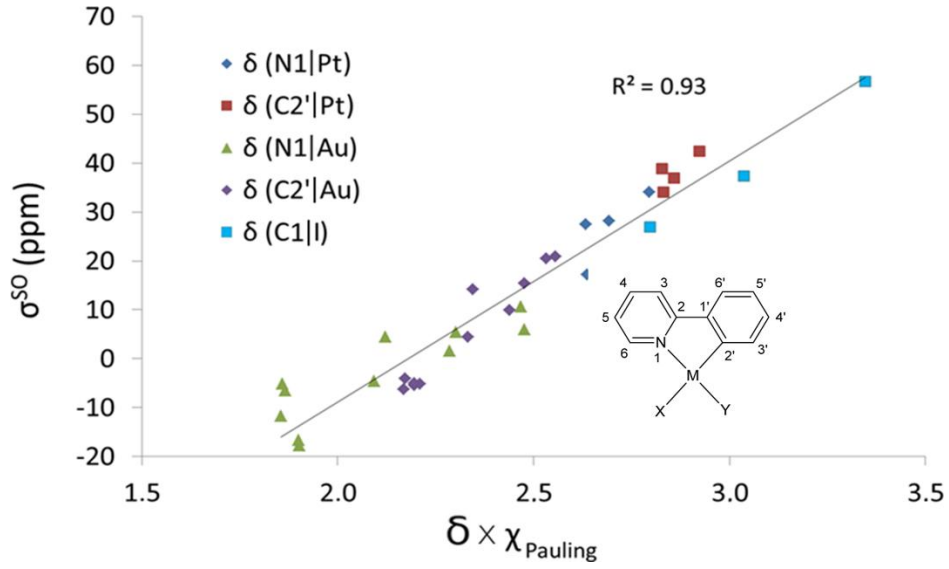

Figure 20: Correlation between DI (δ) from QTAIM analysis (scaled by Pauling electronegativity to account for various ligand atoms) and $\sigma^{SO}(^{13}C,^{15}N)$. [25]

In our last study on this topic,[17] we have greatly extended the test set and performed calculations on a large a series of transition-metal complexes of platinum(II), gold(I), gold(III), and mercury(II), focusing on a general chemical link between electronic structure, HA-LA bond, trans effect and the σ^{p} and σ^{SO}, aiming to unify the concepts discovered in our earlier work.

We first analyzed a series of linear Au(I) pyridine complexes to probe how the structural *trans* effect modulates the length and composition of the HA-LA bond and, in turn, the LA NMR shielding [17]. Our calculations revealed a strong correlation between the nature of the substituent in the *trans* position to the spectator nitrogen atom (further noted also as X) and the magnitude of the $\sigma^{SO}(^{15}N)$. We found that the presence of ligand X with a weak *trans* effect, such as fluoride (F^-), leads to a shorter, more covalent Au–N bond and a positive (shielding) σ^{SO} value (+13.3 ppm). Conversely, a ligand X with a strong *trans* effect, such as a methyl group ($-CH_3$), causes a longer, weaker Au–N bond and a negative (deshielding) σ^{SO} value (–19.6 ppm). Through Energy Decomposition Analysis combined with Natural Orbitals for Chemical Valence (EDA-NOCV), we determined that the character of the Au–N bond is directly influenced by the polarity of the M–X bond. A more polar HA–X bond allows for a more covalent HA–LA bond on the opposite side. The molecular orbital (MO) analysis showed that the strong *trans* effect in the methyl-substituted complex destabilizes a key σ-type Au–N bonding orbital, bringing it energetically closer to other frontier orbitals. This destabilization causes a large deshielding contribution ($\sigma_{HA\text{-}LA} \leftrightarrow LP^*_{HA}$ type coupling) that dominates the overall σ^{SO} and inverts its sign from shielding to deshielding. The *trans* effect described in our previous studies on the orbital level can thus be further generalized with respect to the chemical bond length, although the dependence is not linear.[10]

We then expanded our analysis to compare the isoelectronic d^{10} Au(I) and Hg(II) systems with d^8 Pt(II) complexes to understand how the metal's electronic configuration governs the sign and magnitude of σ^{SO}(LA). Our findings show a clear distinction based on the metal's d-shell occupancy and its involvement in bonding. In d^8 Pt(II) complexes, which have a formally incomplete 5d-shell, occupied π-type orbitals play a dominant role, as we have determined in previous work.[25] This leads to a significant SO shielding at the light atom, with a calculated σ^{SO}(LA) of +51 ppm for our model platinum complex. In contrast, for d^{10} Hg(II) complexes, the bonding is characterized by a significant involvement of the metal's 6p atomic orbitals and a contracted 5d-shell, see Figure 21. Our Hg complex features only about 9% of d-character in the HA-LA bond; the rest belongs to 6s and 6p hybridized orbitals. The role of occupied σ-type HA-LA bonding 6p orbitals is thus enhanced, resulting in a large deshielding σ^{SO}(LA) of –36.8 ppm for the model mercury complex. The Au(I) complexes represent an intermediate case where the electronic structure and the resulting σ^{SO}(LA) can be tuned by the *trans* ligand, pushing the system to behave more like Pt(II) (shielding) or Hg(II) (deshielding).

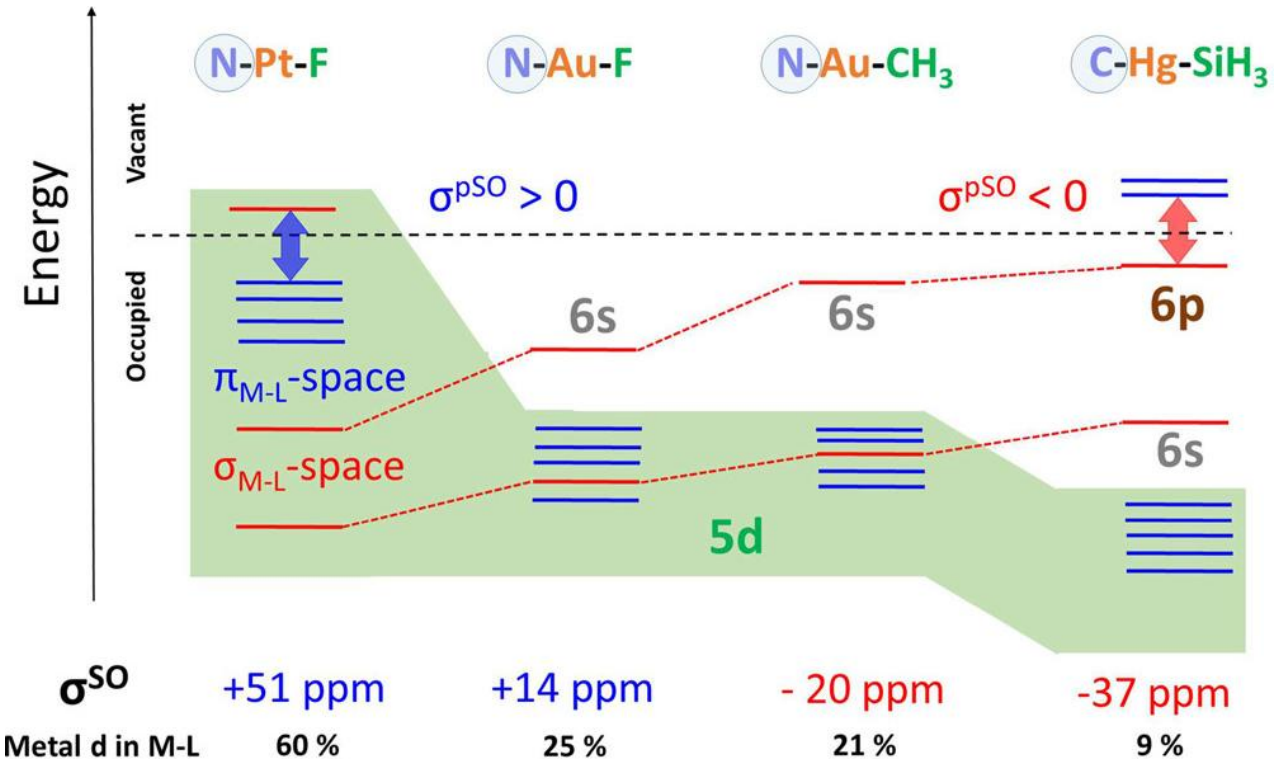

Figure 21: The MO energy levels scheme showing shielding and deshielding σ^{SO}(LA) contributions. The MOs with metal *5d* character are on a green background, π-type MOs are in blue, and σ-type HA–LA orbitals are in red. The σ^{SO}(LA) values and 5d contributions to HA–LA bonds (NBO analysis) are at the bottom.[17]

In the same work, the shielding and deshielding SO-HALA effects were visualized for the first time by the SO-induced electron deformation density (SO-EDD), see Figure 22 [17]. SO-EDD plots show that SO coupling in the Pt(II) complex shifts electron density from the metal's π-space to the ligands' nuclei (shielding). In contrast, in the Hg(II) complex, electron density is accumulated at the metal and depleted at the LA centers (deshielding). This provided a clearly understandable link between relativistic effects and classic NMR theory, in which the changes in electron density around the NMR spectator atom play a significant role.

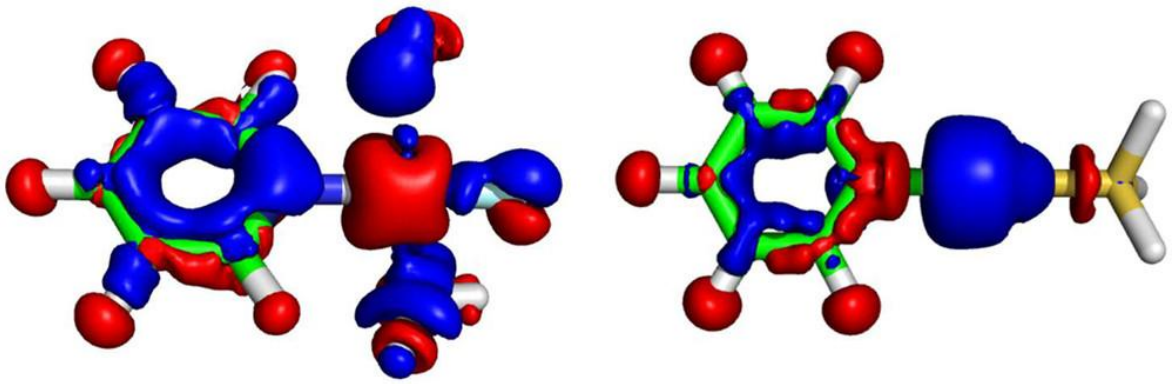

Figure 22: Spin-orbit-induced electron deformation density (SO-EDD) for Pt (left) and Hg (right) complexes.[17]

Based on the series of works summarized in this chapter, we determined how HA-LA bonding characteristics dictate the sign and magnitude of σ^{SO}(LA). We also established for the first time that the sign of σ^{SO}(LA) is fundamentally linked to the character of the σ-type HA-LA orbitals in the frontier region, influencing the balance between shielding and deshielding pathways, which is dictated by the metal's electronic structure and bonding environment.

This research provided a foundation for the detailed interpretation of SO-HALA origin, concepts, and trends across the Periodic Table, discussed in Chapters 1.5 and 2.1 and later published in *Chemical Reviews*.[10] In this review article, named "Relativistic Heavy-Neighbor-Atom Effects on NMR Shifts: Concepts and Trends Across the Periodic Table", we have summarized not only our research but also performed a thorough examination of the literature on SO-HALA over the last 20 years and described general principles, analytical, and computational methods of HALA effects. As a culmination of our efforts, we constructed a complete map of δ^{SO}(LA) sign and magnitude with respect to the electronic configuration of heavy elements across the whole Periodic Table,[10] see Figure 23. The Figure summarizes all my findings in this thesis regarding the propagation of SO-HALA effects across chemical bonds to light atoms. The subsequent Chapter investigates the "through space" SO-HALA effects.

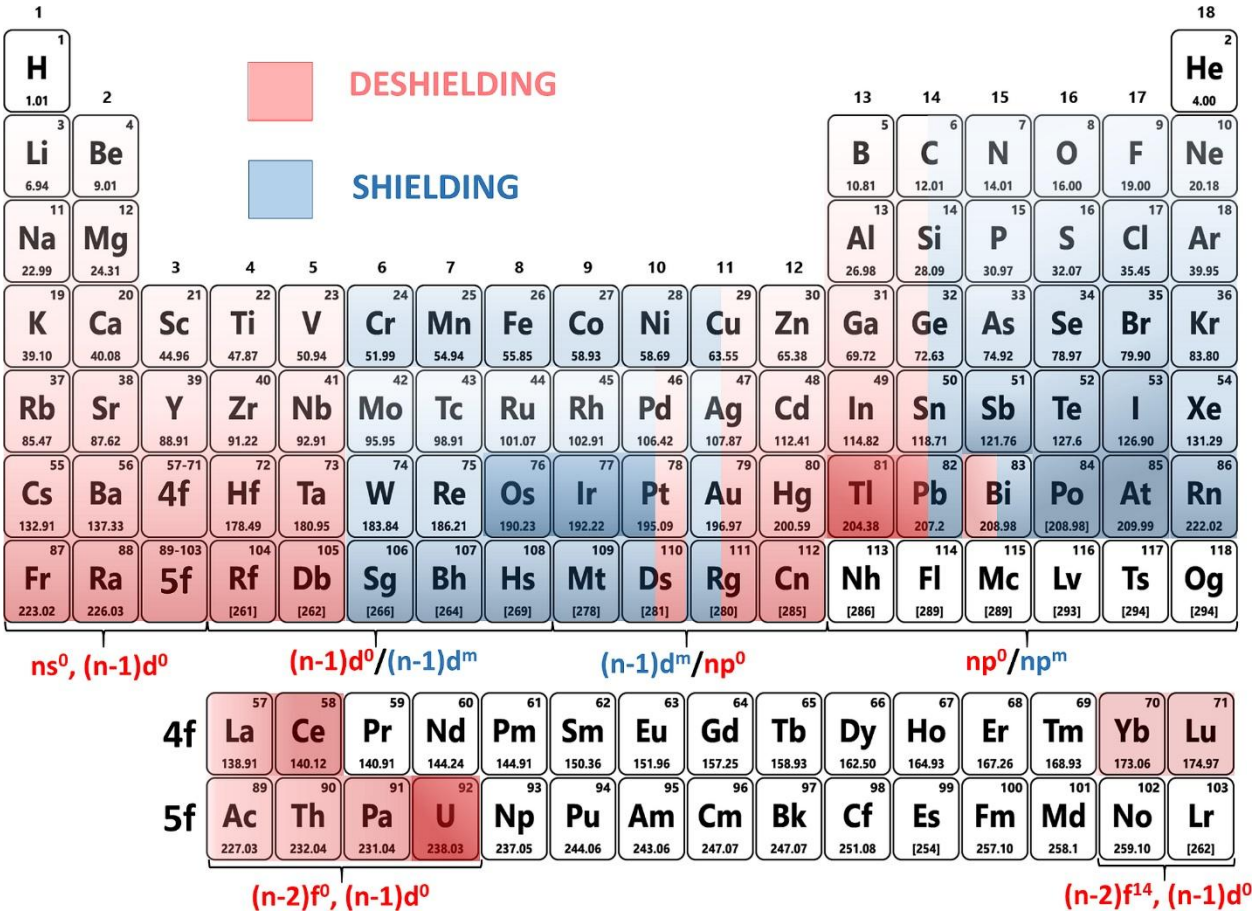

Figure 23: General trends in δ^{SO}(LA) across the Periodic Table. Red color represents deshielding ($\delta^{SO} > 0$), blue color corresponds to the shielding ($\delta^{SO} < 0$). The darker the shade of red or blue, the larger the SO-HALA effects. [10]

2.4 "Through Space" Relativistic Effects

After establishing the relationship between the character of the HA-LA bond and δ^{SO}(LA), I have shifted my focus to the investigation of SO-HALA effects propagation "through space", or more precisely, *via* weak interactions, namely, hydrogen bonds. To the best of my knowledge, the possibility of SO-HALA propagation outside the chemical bonds has not been considered before.

Hydrogen bond (HB) is, according to IUPAC: "*An attractive interaction between a hydrogen atom from a molecule or a molecular fragment X–H, in which X is more electronegative than H, and an atom or a group of atoms in the same or a different molecule, in which there is evidence of bond formation*."[69] This definition is intentionally broad to encompass various interactions now recognized as hydrogen bonds. It marks a shift from older, more restrictive definitions that limited hydrogen bonding to interactions involving highly electronegative atoms like fluorine, oxygen, and nitrogen. However, the IUPAC definition emphasizes that the hydrogen bond must be proven by "evidence of bond formation". [69]

Key criteria of HB formation include a combination of experimental and theoretical evidence, namely:

- **Structural Evidence**: The formation of a hydrogen bond (X–H···Y) leads to characteristic geometric changes. The H···Y distance is typically shorter than the sum of the van der Waals radii of H and Y, and the X–H bond length often increases upon formation of the bond. The geometry of the interaction, specifically the X–H···Y angle, tends to be linear (approaching 180°), though significant deviations are common.
- **Spectroscopic Evidence**: Infrared (IR) spectroscopy is a classic tool for identifying hydrogen bonds. The X–H stretching frequency commonly shows a red shift (a shift to lower wavenumbers) accompanied by significant band broadening and increased intensity. In NMR spectroscopy, forming a hydrogen bond typically causes a downfield shift of the proton signal (deshielding).
- **Energetic Considerations**: Hydrogen bonds are stronger than van der Waals forces but generally weaker than covalent or ionic bonds. Their strength varies widely, and a weak hydrogen bond has no specified lower energy limit.
- **Theoretical Evidence**: Computational chemistry provides powerful tools for identifying and characterizing hydrogen bonds. Electron density topology analysis using methods like the QTAIM can reveal a critical point of the bond between the H and Y atoms, providing direct evidence of a bonding interaction. Orbital analysis can show charge transfer from the acceptor (Y) to the antibonding σ* orbital of the X–H donor group.

The question of whether X–H…Y interaction is a hydrogen bridge or not is particularly complicated when Y is a transition metal. Transition metals may interact with hydrogen in many ways, most of which do not fulfill the conditions set by IUPAC. Yet, the presence of HB in transition metal complexes can be of high interest in transition metal catalysts, as HBs can help to stabilize or reorganize ligands, increasing the catalyst's activity and selectivity.[70] Moreover, HB involving heavy elements such as transition metals contains all the necessary factors for propagation of SO-HALA effects, having both s-character of LA (hydrogen) and involvement of d* orbitals of the acceptor. The prime candidate for forming HB among transition metals is gold, which has the highest electronegativity among all transition metals. According to the extensive review by Schmidbaur et al. [71], although many close-range X–H…Au interactions were reported, most were agostic (i.e., three three-center two-electron bonds), with the only "true" hydrogen bond being present in aurides (Au^-), which are analogous to halogenides.

2.4.1 Searching for Au(I)···H Hydrogen Bond

The existence of X-H…Au(I) hydrogen bond has thus been a subject of intense debate in the chemical literature, with NMR spectroscopy often cited as evidence for such interactions. For instance, Bakar et al. [72] suspected the presence of X-H…Au HB in a large Au_6 cluster, based on the short Au…H distance, and highly deshielded ^{1}H NMR resonance of the hydrogen in question (H2). However, our detailed analysis of this system, published in Nature Communications [22], disproved this assumption. In the work aptly titled "*^{1}H NMR is not a proof of hydrogen bonds in transition metal complexes*", we have used our computational analysis of the $\delta(^1H)$ to demonstrate that the deshielding effect at the relevant hydrogen nuclei is not related to the existence of Au···H–C hydrogen bond.

Briefly, our calculations allowed us to break down the origins of the observed 4.4 ppm deshielding at the key proton (H2), occurring upon formation of the gold cluster. We found the deshielding results from two distinct non-relativistic electronic effects on σ^d and σ^p of H2. Approximately 1.6 ppm of this deshielding arises from the σ^d modulation due to electron density depletion at the H2 nucleus. This change in electron density originates from Au–P π-back-bonding MO and does not involve any direct through-space interaction or bonding between the gold and hydrogen atoms. The remaining ~3.0 ppm of the deshielding comes from the σ^p modulation. We identified local Ramsey-type paramagnetic couplings from a side-on orbital interaction between the C-H bond and a nearby gold atom, Au3, next to the Au with the supposed hydrogen bond. This interaction increases the efficiency of deshielding paramagnetic couplings and thus the increased paramagnetic deshielding in the cluster compared to its precursors, see Figure 24. Moreover, there was essentially no transfer of SO-HALA effects through X-H…Au bond, which should be present in the case of a hydrogen bond.

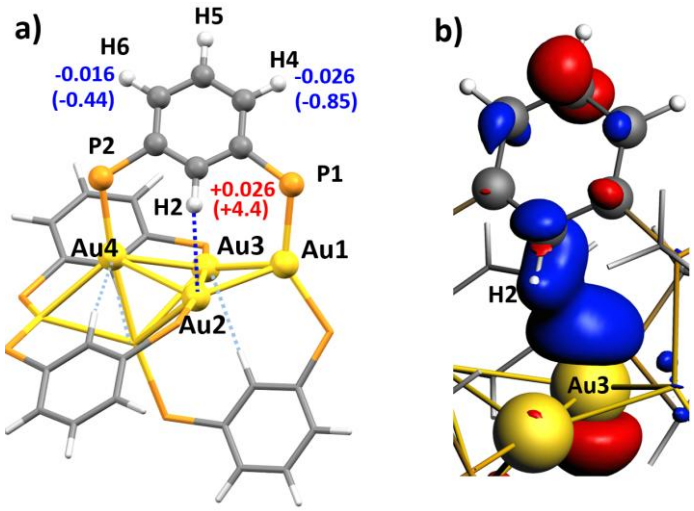

Figure 24: a) Schematic structure of Au complex with large sidechains removed for clarity, b) side-on Au3…H2-C2 interaction.

In conclusion, we have shown that short Au···H contacts in the Au_6 cluster represent a very weak auride-like interaction with minimal stabilizing effect. The distinct ^{1}H NMR deshielding is thus not proof of a significant C-H…Au hydrogen bond. It is caused by a combination of electron density redistribution through the molecule's framework and enhanced local paramagnetic effects from unrelated causes.

Although the SO-HALA effects were negligible, the study demonstrated the importance of a combined experimental/theoretical approach for an unequivocal proof of X-H…Au bond. As a result, we used this combined approach in our subsequent study, where we provided definitive computational and spectroscopic evidence for the existence of an intramolecular Au(I)···H–N hydrogen bond.[27] The work, later published in Angewandte Chemie, was centered on a $[Cl–Au–L]^+$ complex where L is a protonated N-heterocyclic carbene (complex **1** in Figure 25), which we characterized by helium-tagging infrared photodissociation (IRPD) spectroscopy. The complex proved unstable in solution, making gas-phase experiments and theoretical modeling essential for its characterization.

Our computational investigation began with identifying the stable conformation of complex **1**. We optimized the geometries of two possible conformers using density functional theory (DFT) methods, specifically our previously validated approach using PBE0-D3/def2-TZVPP. The first conformer, **1_A**, featured the N–H^+ group oriented towards the gold atom, while the second, **1_B**, had this group rotated away (see Figure 25). Our calculations showed that conformer **1_A** is approximately 10–12 kcal/mol (depending on the method used) more stable than **1_B**, with a significant barrier of about 12 kcal/mol for the interconversion. The calculated equilibrium geometry of **1_A** revealed a Au···H distance of roughly

2.17 Å (about 0.7 Å shorter than the sum of VdW radii of Au and H), which is also shorter than 2.20 Å in 1_B, and an Au–H–N angle of about 160°. All of these are structural hallmarks of a hydrogen bond.

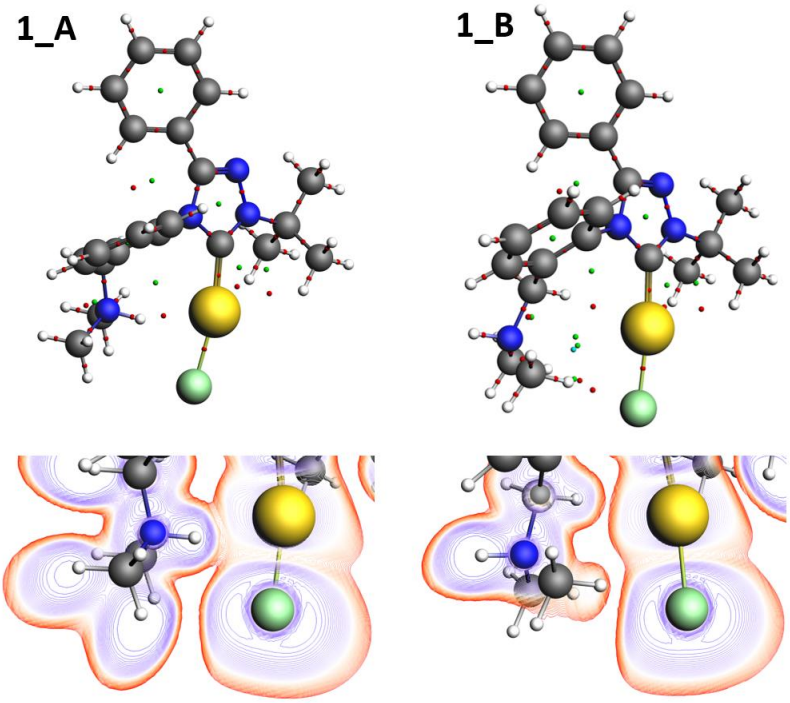

Figure 25: a) Structures of complex **1** conformers **1_A** and **1_B** with bond critical points (BCPs, red) and ring critical points (RCPs, green) from QTAIM analysis, b) Plots of the Laplacian of the electron density. [27]

A critical component of our study was directly comparing our computational results with the experimental IRPD spectra. To achieve this, we performed computationally intensive anharmonic vibrational frequency calculations. The simulated anharmonic spectrum for conformer **1_A** showed excellent agreement with the experimental data, successfully reproducing the key features. It most notably captured the substantial red shift of the N–H stretching modes to 3061 cm^{-1} and a complex series of bands between 2600 and 2900 cm^{-1}.[27] In contrast, the calculated spectrum for the non-bonded conformer **1_B** was inconsistent with our experimental observations, as it predicted an unperturbed N–H vibrational band around 3280 cm^{-1}, a feature completely absent in the experimental spectrum. This provided conclusive evidence that the molecule exists as conformer **1_A** and that the N–H bond is directly involved in the strong intramolecular interaction.

Further computational analysis of the vibrational modes in **1_A** revealed that the fundamental N–H vibration mode is coupled with the molecular framework's strong anharmonic low-frequency vibrational

modes. Our calculations showed that these couplings, which appear as a series of combination bands in the spectrum, correspond to the bending and sliding of the N–H^+ moiety relative to the Au–Cl bond. The existence of these strong couplings is a direct spectroscopic manifestation of the Au···H^+–N interaction and provides direct evidence for the bond's existence.

To quantify the strength and nature of Au···H^+–N interaction, we employed several bonding analysis methods. We calculated the counterpoise-corrected interaction energy in a simplified model system, which was -10.8 kcal/mol (at the PBE0-D3/def2-TZVPP level), confirming a HB of moderate strength. An Energy Decomposition Analysis (EDA) revealed that Au···H^+–N interaction energy arises from a combination of orbital and electrostatic interactions (which together account for about 60% of its energy) and dispersion forces (contributing the remaining 40%). We also characterized the bond using QTAIM and NBO analysis. The QTAIM analysis identified a bond critical point (BCP) between the gold and hydrogen atoms in **1_A**, having a positive Laplacian value and an electron density of $\rho = 0.033$ e·bohr^{-3}, which are characteristic of a moderate, closed-shell hydrogen bond, see Figure 25. The NBO analysis complemented this finding by identifying a strong donor-acceptor interaction between a lone-pair orbital on the gold atom and the antibonding σ^*_{N-H} orbital, with an estimated second-order perturbation energy E(2) of -13 kcal/mol. This confirmed the role of the gold atom as the electron donor in the hydrogen bond.

Finally, we have performed NMR calculations, which provided further evidence for the Au···H–N bond. The calculated $\delta(^1H)$ of the hydrogen atom involved in the bond (**1_A**) was 10.6 ppm, representing a significant deshielding of 5.8 ppm compared to the non-bonded conformer **1_B**. While deshielding may not be conclusive proof of hydrogen bonding, as we have shown in our previous work[22], a more definitive piece of evidence came from the calculated $\delta(^{15}N)$. Our calculations revealed a sizable SO contribution of -5.8 ppm to the shielding of the nitrogen nucleus in **1_A**. Such a substantial SO-HALA can only be induced by the Au atom through direct Au···H^+–N interaction, because the H-N bond is too far from Au for the SO-HALA effect to propagate *via* chemical bonds.

In summary, our computational analysis provided robust proof of the existence of a moderate-strength intramolecular Au(I)···H–N hydrogen bond. Through detailed calculations of the molecular structure, stability, anharmonic vibrational spectra, and NMR properties, we were able to interpret the experimental data and unambiguously characterize the nature of this interaction, demonstrating that it is a genuine hydrogen bond governed by a combination of electrostatic, orbital, and dispersion forces.

2.4.2 Experimental Proof of "Through Space" SO-HALA Effect Propagation

Although our calculation predicted the transport of the SO-HALA effect *via* Au(I)···H–N hydrogen bond to the ^{15}N nucleus, the experimental proof of this interaction was missing, as NMR spectra of complex **1** could not be measured at that time.

Hence, to obtain the experimental proof of "through space" SO-HALA effect propagation, we performed a solid-state investigation of a series of 4-dimethylaminopyridinium ($DMAPH^+$) salts with different halide counter-ions, namely iodide (I^-), bromide (Br^-), and chloride (Cl^-).[15] We selected these systems for several reasons. First, 4-dimethylaminopyridine (DMAP) is a strong organic base that readily forms salts, and second, solid-state NMR (SS-NMR) spectroscopy provides an ideal platform for studying these interactions, as the restricted molecular motion conserves the interatomic distances and simplifies the interpretation of spectra compared to the solution. We successfully synthesized the salts $[DMAPH]^+I^-$, $[DMAPH]^+Br^-$, and $[DMAPH]^+Cl^-$, and determined their solid-state structures using X-ray diffraction. The basic structural motif in these compounds is a dimer of $DMAPH^+$ cations, where the pyridinium protons (H1) form hydrogen bonds with a pair of halide anions (Figure 26).

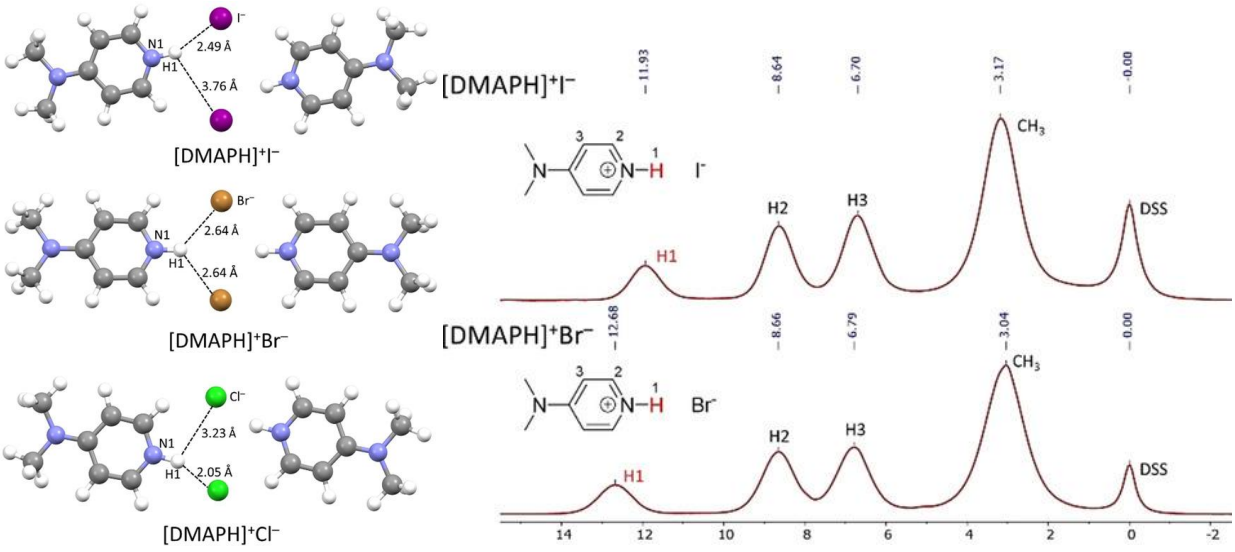

Figure 26: Left: Structures of $DMAPH]^+I^-$, $[DMAPH]^+Br^-$, and $[DMAPH]^+Cl^-$ complexes. Right: ^1H MAS NMR spectra of solid $[DMAPH]^+I^-$ and $[DMAPH]^+Br^-$ adducts relative to DSS.[15]

Next, ^1H SS-NMR spectra for these salts were measured using ultra-fast magic-angle spinning (MAS). The spectra revealed that while the $\delta(^1H)$ for the methyl protons and the aromatic protons H2 and H3 were nearly identical across the different salts, the $\delta(^1H)$ of the H1 proton, which is directly involved in the N–H^+···X^- hydrogen bond, varied significantly depending on the halide. Specifically, the H1 signal in the iodide

salt had been shielded compared to the bromide and chloride salts, hinting at a unique effect involving the heavy iodine atom (see Figure 26).

To explain the origin of these differences, we first employed the standard gauge-including projector-augmented wave (GIPAW) methodology, a DFT-based approach for calculating NMR parameters in crystalline solids. It is important to note that this method includes scalar relativistic effects but omits the SO coupling contribution. We observed a good linear correlation for most protons when we plotted the experimental ^{1}H chemical shifts against our calculated values. However, the H1 signal of the $[DMAPH]^{+}I^{-}$ system was a clear outlier, with the calculated value deviating from the experimental one by approximately one ppm, see Figure 27.

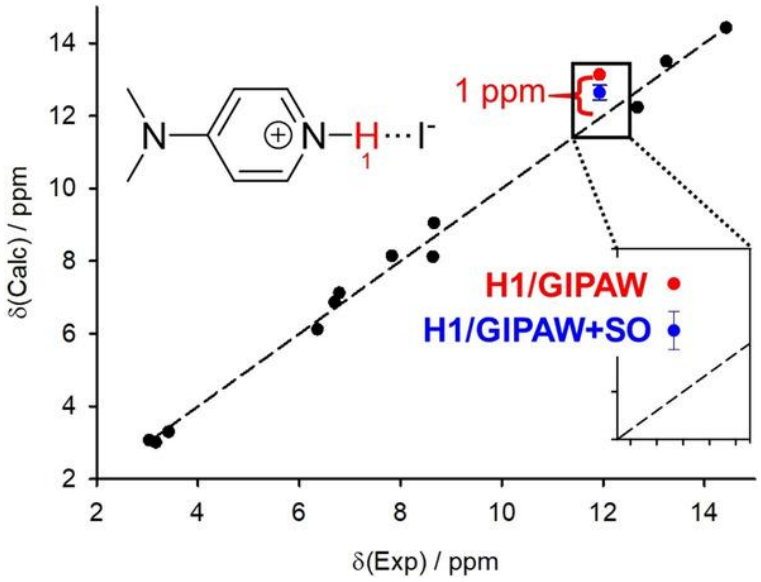

Figure 27: The plot of experimental and calculated (GIPAW/PBE) ^{1}H NMR chemical shifts in DMAP salts with and without the SO correction.[15]

This deviation is substantially larger than the typical errors found in these types of calculations for molecular solids. Furthermore, the magnitude of this deviation correlated with the atomic number of the anion: it was largest for iodide (~1 ppm), smaller for bromide (~0.6 ppm), and negligible for chloride (~0.1 ppm). This trend strongly suggests that deviation is caused by spin-orbit coupling.

We calculated δSO(H1) in the $[DMAPH]^{+}I^{-}$ system to test this hypothesis. We found that at all tested levels of theory, the calculated $\delta^{SO}(H1)$ was negative, indicating a shielding effect, with a magnitude between -0.35 and -0.6 ppm, depending on the method used. When we added this calculated SO correction to our initial GIPAW result, the agreement with the experimental data improved dramatically. The corrected

value for the H1 proton in the iodide salt no longer appeared as an outlier and fell neatly in line with the other data points.

To better understand the pathway for this effect and further support our findings, we analyzed the nature of the N–H^+···I^- interaction by QTAIM. We identified a bond critical point between the H1 and I^- atoms, which is characteristic of a moderate-strength hydrogen bond. Further analysis confirmed a degree of electron sharing between the two atoms, a prerequisite for the propagation of the SO effect. The interaction energy was calculated to be around -10 kcal/mol, confirming a hydrogen bond of medium strength.

The molecular orbital (MO) analysis also revealed the electronic origin of the shielding effect. The SO operator on the heavy iodine atom enables a mixing of iodine's occupied 5p lone pair orbitals with the N1–H1 bonding orbital. This mixing, which is forbidden at the non-relativistic level, results in an additional shielding contribution (a negative δ^{SO}). We visualized this mechanism with an SO-EDD plot, which clearly showed that the SO interaction causes a depletion of electron density from the σ-space of the hydrogen bond, while increasing the electron density in the π-space and at the H1 nucleus, thus influencing the Ramsey-type paramagnetic couplings, see Figure 28.

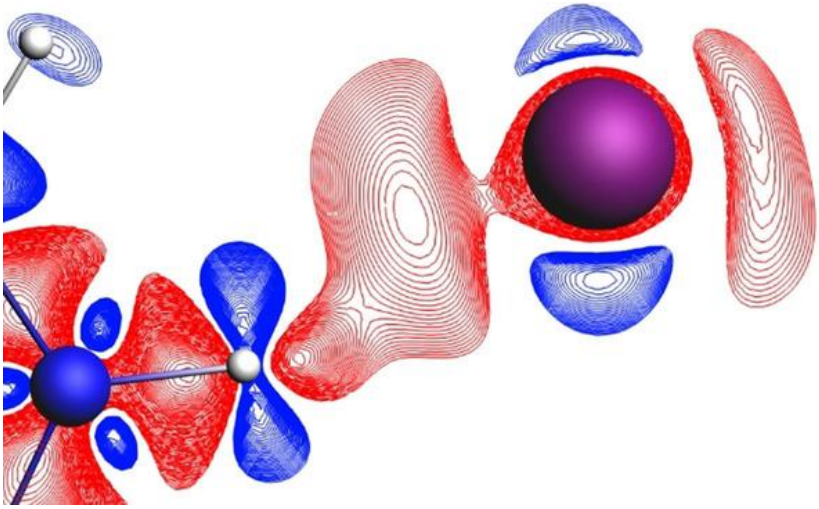

Figure 28: SO-EDD plot of N1-H1···I^- interaction in the $[DMAPH]^+I^-$ complex. [15]

In summary, our work [15] provides the first combined experimental and theoretical evidence that the SO-HALA effect is being transmitted from the iodide anion to the H1 proton through the N–H^+···I^- hydrogen bond. By comparing high-resolution solid-state NMR data and relativistic calculations, we demonstrated that spin-orbit coupling is essential for accurately predicting the ^{1}H NMR chemical shift of a proton in a hydrogen bond with a heavy atom. This finding confirms for the first time that relativistic effects can be transmitted "through-space" *via* non-covalent interactions.

2.5 Further Applications of HALA Effects Analysis

2.5.1 Relativity vs. Aromaticity in Osmabenzenes

Osmabenzenes provide a compelling example of how heavy elements can influence aromatic phenomena. In our study [21], we investigated the magnetic properties and aromaticity of osmium-containing metallacycles, specifically focusing on osmabenzene and osmapentalene derivatives, by employing both scalar-relativistic and fully relativistic DFT calculations. Our work aimed to dissect the origins of their unique NMR characteristics, revealing that paramagnetic and relativistic effects, rather than aromaticity, are the primary drivers of the observed phenomena.

Our analysis of the magnetically induced current density (MIC) in osmabenzene revealed a unique σ-type Craig-Möbius magnetic aromaticity, a distinct difference from conventional π-aromatic systems. This arises because the MIC density around the osmium atom is shaped like a $5dz^2$ orbital, which lacks the correct symmetry to overlap with the carbon p-orbitals, thereby preventing a π-current along the Os–C bonds. A key finding was that the osmium atom generates a powerful local paramagnetic current with its partially filled 5d subshell. The strength of this current passing between the osmium atom and the center of the osmiumbenzene ring was calculated to be nearly -140 $nA.T^{-1}$, an order of magnitude larger than the actual aromatic ring currents in the molecule. This intense local paramagnetic current significantly impacts methods like Nucleus-Independent Chemical Shift (NICS) used to assess aromaticity. Because NICS measures magnetic shielding at a single point, it cannot distinguish the genuine ring current from the overwhelming local paramagnetic effect of the osmium atom, vastly overestimating aromaticity in these heavy-element systems.

The high NMR deshielding observed in the NMR spectra of light atoms near the osmium center had previously been attributed to the molecules' aromaticity. However, our analysis demonstrates this is incorrect. The deshielding is instead caused by local Ramsey-type paramagnetic couplings between the occupied bonding σ(Os–C) orbitals and the vacant antibonding π*(Os) orbitals. This paramagnetic effect is substantial; for the carbon atoms C1 and C5 in osmabenzene, the magnetic shielding tensor component parallel to the Os–C bond is deshielded by approximately -350 ppm. While this powerful deshielding dominates, a secondary effect from the osmium's paramagnetic current is the induction of shielding currents around the neighboring carbons, resulting in a shielding of about +200 ppm in the tensor component perpendicular to the molecular ring.

Our fully relativistic calculations also quantified the significant role of SO coupling on the NMR chemical shifts. For the carbon atoms directly bonded to osmium (C1 and C5) in osmabenzene, the δ^{SO}(LA) is

strongly shielding, calculated to be +29 ppm and +23 ppm, respectively. This relativistic shielding effect partially counteracts the much larger paramagnetic deshielding. A notable observation is that δ^{SO}(LA) sign oscillates with distance from the heavy osmium atom. While the effect shields the adjacent carbons, it becomes deshielding for protons located further away. This alternation correlates directly with the spin-orbit-induced magnetic currents (SO-MIC) orientation at each nucleus, offering an alternative way of looking at long-range SO-HALA effects, see Figure 29. In the first approximation, the δ^{SO}(LA) could be considered a product of counter-directional currents at the light atoms, induced by a movement of electrons around the osmium atom within an external magnetic field. Tertiary currents that arise in response to these secondary ones, and δ^{SO}(LA) is propagated further. The SO-MIC can explain the alternating signs of SO across the molecule.

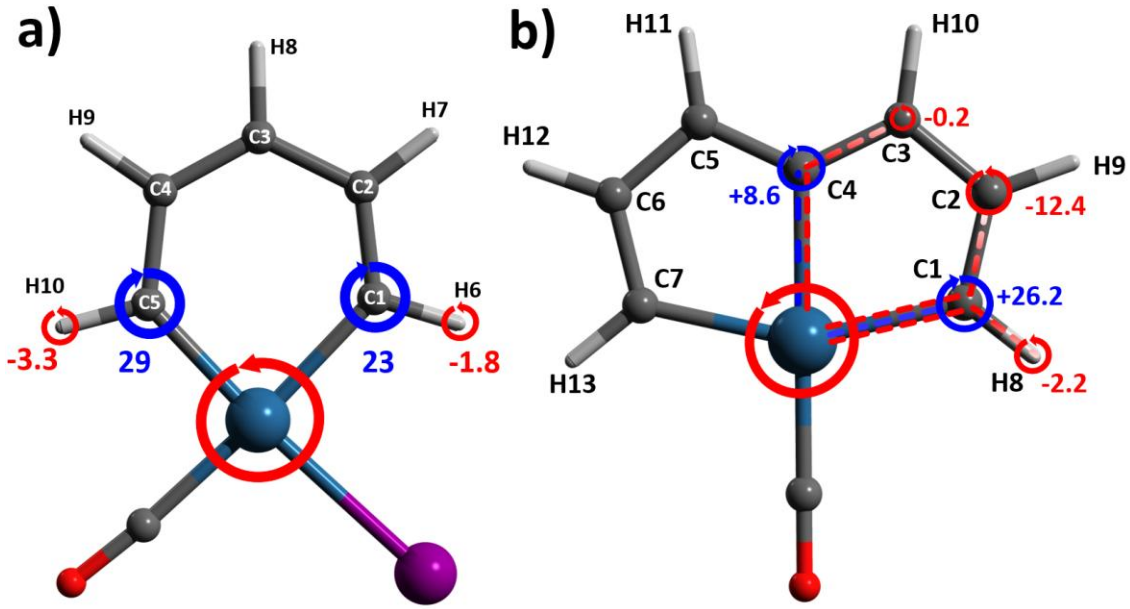

Figure 29: Schematic representation of SO-induced magnetic current direction around C1, C5, H6, and H10 in osmabenzene and around C1-C4 and H8 in osmapentalene with σ^{SO}(LA) in ppm. Blue represents σ^{SO}(LA) shielding and diatropic SO-induced magnetic current, while red is associated with σ^{SO}(LA) deshielding and paratropic SO-induced magnetic current.

2.5.2 Highly Accurate Calculations of NMR Spectroscopic Parameters in Solid State

In this study,[20] we systematically investigated the factors contributing to the accuracy of quantum-chemical predictions for proton NMR chemical shifts in molecular solids. To do this, we focused on six amino acids, which provided a range of hydrogen bonding environments, including CH, CH_2, CH_3, OH, SH, and NH_3 groups. We obtained high-resolution experimental data for these compounds using ultra-fast MAS NMR. Then we compared these results to a series of theoretical calculations to identify the sources of error and the most effective methods for improving computational accuracy.

We began by using the GIPAW method with a GGA-level DFT functional. Our results showed that this standard method produced significant deviations from experimental values, with errors reaching 1.5 ppm. The most crucial discrepancy was observed for the SH proton in L-cysteine. Still, several other protons also showed considerable errors, highlighting the limitations of this standard level of theory for achieving high accuracy.

To improve upon these results, we explored several corrections. We first calculated corrections on isolated molecules extracted from the crystal structures, using higher levels of theory. These included a hybrid density functional (PBE0) and more computationally expensive methods like MP2 and coupled-cluster singles and doubles (CCSD). However, we found that these corrections alone did not systematically improve the accuracy of the $\delta(^1H)$ predictions. The most significant improvement came from including the effects of molecular dynamics and, crucially, nuclear quantum effects (NQEs) through path-integral molecular dynamics (PIMD) simulations. These PIMD corrections were substantial for all proton types. The corrections were consistently negative (deshielding) for hydrogens attached to carbon or nitrogen, typically in the range of -0.6 to -1.0 ppm. The corrections for OH and COOH protons were similarly significant. The SH proton in L-cysteine was a unique case, exhibiting a shielding PIMD correction that was highly dependent on its specific hydrogen-bonding environment (S–H···S vs. S–H···O). We then investigated the influence of SO coupling, which is known to be necessary for atoms near heavy elements. Interestingly, our calculations confirmed that the SO contribution was essential for accurately modeling the chemical shift of the SH proton in L-cysteine. It amounted to 0.56 ppm for the ^1H NMR chemical shift of the SH proton, which is rather large given that sulfur is generally not considered a heavy element.

Ultimately, we achieved the best agreement with our experimental data by combining multiple corrections, which reduced the root-mean-square deviation (RMSD) by approximately half compared to the uncorrected GIPAW calculations, and the maximum error dropped from 1.5 ppm to a more acceptable 0.4 ppm. In contrast, for carbon-13 chemical shifts, we found that a simple and computationally inexpensive molecular correction using the hybrid PBE0 functional provided the best results, likely due to

a fortunate cancellation of errors. Our work demonstrates that for highly accurate proton NMR predictions in molecular crystals, it is critical to account for nuclear quantum effects and, when relevant, relativistic spin-orbit coupling, even in the case of third-period elements.

2.6 Beyond NMR

The importance of relativistic effects to spectroscopic parameters is, of course, not limited to NMR. Thus, my experience in calculating and understanding relativistic effects found applications outside the NMR when I joined a team developing and validating robust computational methods to accurately simulate X-ray absorption spectra (XAS). [14, 19]

Our work began with establishing a highly accurate benchmark using the "gold standard" of relativistic calculations, the 4c relativistic theory[19]. Then, these findings were extended to develop more computationally efficient exact two-component (X2C) methods that retain the accuracy of the parent 4c approach.[14] A central theme across our studies has been the meticulous calibration of computational techniques, revealing the critical role of Hartree-Fock (HF) exchange in achieving agreement with experimental data.

Our initial study aimed to establish a reliable computational protocol for simulating XAS using 4c damped response time-dependent density functional theory (4c-DR-TDDFT). This method is suited for X-ray applications because it includes both scalar and SO relativistic effects variationally and can calculate XAS spectra directly for a selected frequency region. We calculated XAS spectra for a carefully selected set of closed-shell transition metal and actinide compounds to assess the influence of molecular geometry, basis sets, and functionals. The calibration set included $VOCl_3$, CrO_2Cl_2, MoS_4^{2-}, WCl_6, $PdCl_6^{2-}$, ReO_4^-, and $UO_2(NO_3)_2$, which encompass 3d, 4d, 5d, and 5f elements with various and oxidation states. This diverse collection of compounds was chosen to ensure the broad applicability of our computational protocol across different chemical environments and electronic structures.

It was established that factors like using an optimized versus an experimental (X-ray) geometry or increasing the basis set size beyond augmented double-zeta (aVDZ) quality for light atoms had a negligible effect on the positions of the main absorption lines. Even in MoS_4^{2-}, whose experimental structure had C_{3v} symmetry with Mo-S bonds of 2.193 and 2.172 Å due to crystal packing effects, while the optimized geometry had (artificial) T_d symmetry with all Mo-S bonds being 2.193 Å, calculated XAS spectra showed negligible variations in the positions and intensities of the absorption bands.

The investigation of different DFT functionals revealed that the choice of functional profoundly influences the calculated spectra. We tested PBE, PBE0, B3LYP, B3LYP-50HF, and CAM-B3LYP functionals, finding that while pure GGA functionals like PBE performed poorly, hybrid functionals showed significant improvement. Range-separated functionals like CAM-B3LYP, however, provided results almost identical

to their global hybrid counterparts, suggesting that the global amount of HF exchange is more important than its long-range behavior for core excitations.

Most importantly, we discovered that the energy shift of calculated spectra compared to experimental results has a linear dependence on the amount of HF exchange included in the functional. This linear correlation held regardless of the underlying functional (e.g., PBE0 or B3LYP), indicating that the percentage of HF exchange is the most critical parameter for accurately predicting spectral line positions. This is highly similar to the dependence found in our earlier work on NMR CS. [16, 29] This time, however, the dependence could not be explained by missing relativistic terms, as fully relativistic calculations were used. Nevertheless, optimizing the HF exchange allowed us to determine an optimal amount that minimizes the deviation from experimental values. We systematically investigated the dependence of XAS spectra on the amount of HF exchange using PBE0-XHF functionals, where X varied from 0% to 60%, see Figure 30. We also explored B3LYP variants and found that the relative shift of the XAS signals, defined as $(E_{Theor} - E_{Exp})/E_{Exp}$, depends linearly on the percentage of HF exchange, regardless of the original type of hybrid functional used. For absorption edges above 1000 eV, which includes the L- and M-edges of many heavy elements, we established that an optimal value of 60% HF exchange consistently provides the best results. This "60% rule" yields remarkable accuracy, with relative errors below 0.2% for absorption edge energies and below 2% for SO splittings.

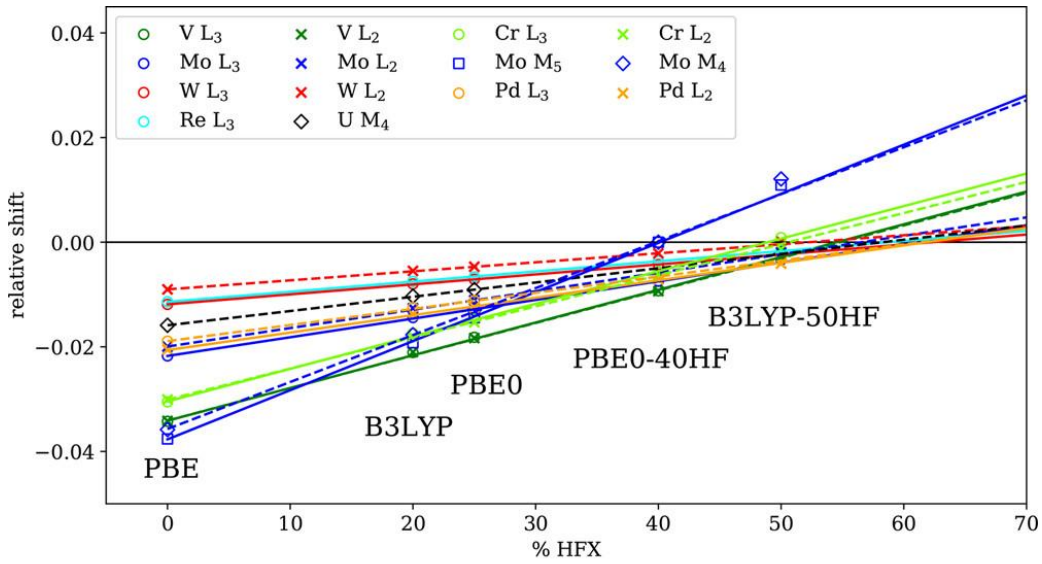

$$\text{relative shift} = (E_{\text{Theory}} - E_{\text{Exp}})/E_{\text{Exp}}$$

Figure 30: Relative shifts of XAS spectral lines concerning the percentage of HFX in a functional.[19]

For lower energy regions (below 1000 eV), the optimal amount varied between 40% and 50%, suggesting an energy-dependent optimization where higher energies require more HF exchange to correct self-interaction errors. Establishing this protocol provides a predictive tool that avoids the need for arbitrary, system-specific energy corrections introduced in other computational methods to match experimental data.

Our method also allows for variation of the damping parameter, and thus control over the signal broadening. This allows for modifying calculated signals to match experimental ones, or to split the signals into individual lines for detailed analysis. Figure 31 depicts the results of damping parameter variation in the heaviest tested system, the M4-edge of $UO_2(NO_3)_2$, including splitting the spectrum into individual lines, thus matching the best experimental methods available (HERFD).

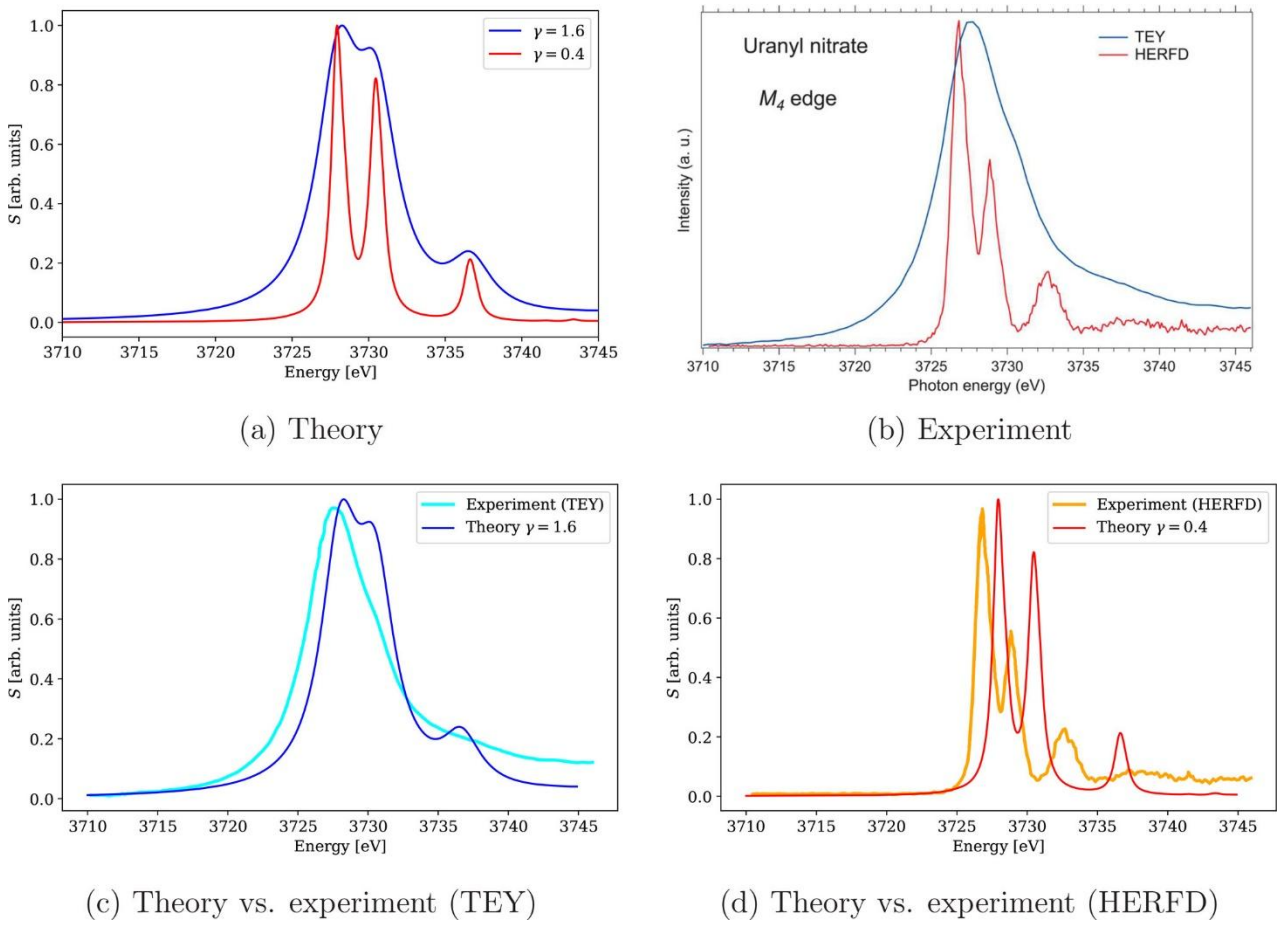

Figure 31: Calculated XAS spectra near the uranium M4-edge in $UO_2(NO_3)_2$. Comparison of different damping parameters and experimental results. No artificial energy shifts were applied to the spectra. [19]

While the 4c-DR-TDDFT method proved highly accurate, its computational cost can be prohibitive. This motivated our subsequent work, where we developed and validated a more efficient X2C method to achieve 4c quality at a 2c cost. In this second study, we evaluated several "flavors" of X2C Hamiltonians by repeating the calibration study on the same molecular set we used in our previous work.

Our analysis revealed that the widely used one-electron X2C (1eX2C) approximation, which neglects two-electron picture-change (PC) corrections, suffers from a significant flaw: it consistently overestimates the spin-orbit splitting compared to both the 4c calculations and experimental data. This error is not merely a quantitative inaccuracy in peak positions—for instance, it can lead to shifts as large as 20 eV in the L-edge spectrum of WCl_6—but can also qualitatively alter the spectral shape when different SO-split edges (like L_2 and L_3) overlap. This shortcoming was particularly evident in the spectra near the molybdenum M_4- and M_5-edges of MoS_4^{2-}, where the 1eX2C method caused lines from different edges to overlap and merge, resulting in a different overall spectral shape compared to the 4c reference.

Our more advanced atomic mean-field (amfX2C) and extended atomic mean-field (eamfX2C) approaches correct this shortcoming. These methods properly account for the two-electron scalar and spin-orbit PC effects that arise from the X2C transformation. Our calibration demonstrated that both the (e)amfX2C and the molecular mean-field (mmfX2C) Hamiltonians exactly reproduce the reference 4c spectra in all essential features, including shape, position, and, crucially, the SO splitting, see Figure 32.

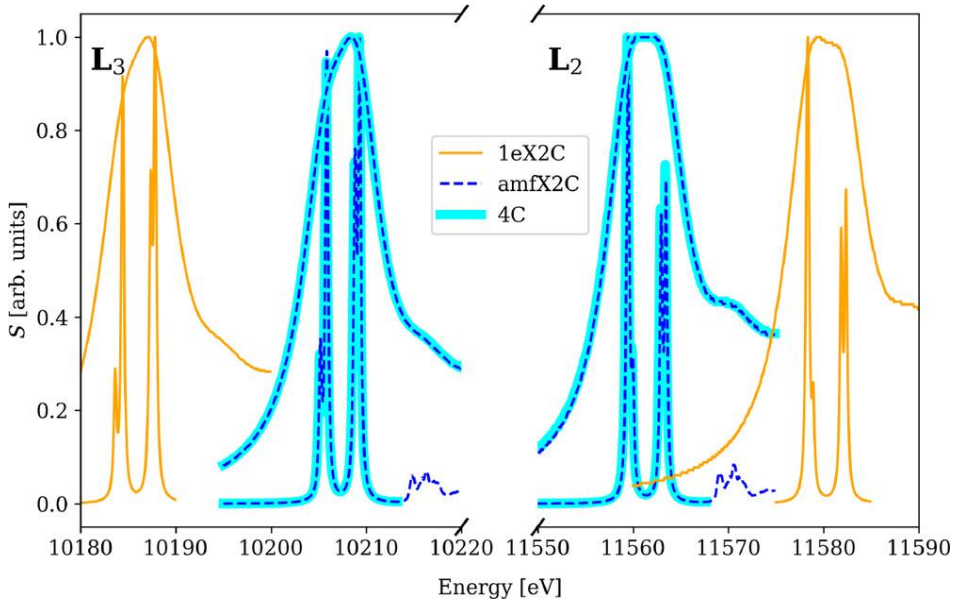

Figure 32: Comparison of 1eX2C, amfX2C, and 4c reference XAS spectra of $[WCl_4(PMePh_2)_2]$ near $W_{L2,3}$-edges. Note the perfect agreement between amfX2C and 4c. No corrections for energy were performed. [14]

The excellent agreement between the (e)amfX2C methods and the parent 4c approach means that the computational protocol calibrated in our previous study can be directly transferred to these more efficient 2c calculations. One can thus apply the 60% HF exchange rule to these 2c calculations and expect the same high level of accuracy as the 4c approach, without relying on any cancellation of errors.

The validation of this claim was demonstrated through comprehensive benchmarking. We achieved remarkable accuracy with the optimized 60% HF exchange protocol for the main absorption lines across our calibration set. For example, in the case of WCl_6, our calculations predicted the L_3-edge at 10207.3 eV compared to the experimental value of 10212.2 eV, representing an error of only -4.9 eV or -0.05%. Similarly, for $PdCl_6^{2-}$, our L_3-edge prediction of 3173.4 eV compared to the experimental 3177.8 eV, with an error of -4.4 eV or -0.14%. The spin-orbit splitting was reproduced with even higher precision, with most systems showing errors below 2% of the experimental values. The calibration also demonstrated that the computational protocol performs consistently across different types of systems, from early transition metals like vanadium and chromium to actinides like uranium, validating the broad applicability of our approach.

Furthermore, these accurate 2c methods offer a significant computational advantage. Our benchmarks showed that the amfX2C approach provides an approximately 7-fold speedup in the DR-TDDFT step compared to the 4c calculations, drastically reducing the time required for simulations. A calculation that might take a week with 4c methods can now be completed in less than a day using amfX2C, without sacrificing accuracy. This computational efficiency was demonstrated in our calculations of larger systems, where we successfully calculated XAS spectra for $[RuCl_2(DMSO)_2(Im)_2]$ containing 41 atoms and 4652 4c basis spinors, and $[WCl_4(PMePh_2)_2]$ containing 59 atoms and 7212 4c basis spinors (Im = imidazole, Me=methyl, Ph=phenyl). Using the calibrated 60% HF exchange protocol and changing the damping parameter, we could provide detailed assignments of XAS spectral features based on ligand field theory and double point group symmetry.

In conclusion, our combined work provides a validated approach for the accurate and efficient first-principles simulation of X-ray absorption spectra for heavy-element systems. A combination of high precision and reasonable computational cost makes the high-accuracy simulation of XAS for large and complex molecular systems accessible to researchers studying heavy-element chemistry and materials science.

Part 3: Summary and Outlook

This habilitation thesis presented an overview of my research regarding the relativistic effects in NMR and beyond. In my work, I have shown that relativistic effects are not just theoretical curiosities but are behind many experimental concepts.

The key scientific contribution of my research is understanding the SO-HALA effects and the electronic structure relationship, based mainly on a third-order perturbation theory (PT3) analysis. This analysis identified six fundamental orbital magnetic coupling pathways that determine both the magnitude and sign of SO-HALA effects, leading to the formulation of the "lone-pair rule". The lone pair rule explained the dependence of the SO-HALA effect on heavy element configuration, enabling the qualitative prediction of SO-HALA effects. According to this rule, heavy atoms with occupied non-bonding lone electron pairs typically induce shielding (negative) SO effects at adjacent light nuclei. In contrast, those with formally empty valence shells cause deshielding (positive) SO effects. This approach was validated across the entire Periodic Table.

Another significant outcome of my research was discovering and predicting new chemical shift ranges that extend far beyond conventional NMR windows. The work on lead(II) hydrides was particularly impactful, as predicting ^{1}H NMR chemical shifts for these elusive compounds allowed the first lead(II) hydride to be characterized by NMR shortly after. Its structure and NMR chemical shift nearly perfectly matched my prediction. The measured ^{1}H NMR chemical shift of 31.1 ppm also represents the most deshielded ^{1}H NMR signal ever recorded for a diamagnetic compound.

I have also delved into structure-property relationships showing that SO-HALA effects can be used as sensitive electronic structure and chemical bonding probes. In particular, the degree of covalency in the HA-LA bond was crucial for the efficiency of SO-HALA propagation; more covalent bonds can carry larger relativistic effects. This relationship was quantified by analyzing delocalization indices (DI) from the Quantum Theory of Atoms in Molecules (QTAIM), providing a universal predictor for the magnitude of SO-HALA effects across diverse chemical systems.

I have also participated in discovering the first Au(I)….H-X hydrogen bond and in the theoretical/experimental proof of "through-space" relativistic effects, which are transmitted *via* hydrogen bonds, i.e., outside classical chemical bonds.

Last but not least, my work also extended to applications beyond NMR spectroscopy, specifically to X-ray absorption spectroscopy (XAS), where relativistic effects are crucial for accurate spectral interpretation. I

have participated in developing four-component and exact two-component (X2C) methods, which can deliver four-component quality results at a significantly reduced computational cost, making high-accuracy relativistic calculations accessible for larger and more complex molecular systems.

I hope that insights gained throughout my work provide a foundation for a further understanding of how relativistic quantum mechanical phenomena manifest as observable chemical properties, and that I was able to bring relativistic NMR closer to everyday use. I hope that as computational methods become more and more accessible and experimental techniques become more sensitive, relativistic quantum chemistry will play an increasingly important role in advancing our understanding of the fascinating world of heavy element chemistry.

List of Figures

Figure 12: Structures of experimentally prepared Tl^{+} and Pb^{2+} compounds where LA NMR chemical shifts were not reported. Me = methyl, iPr = isopropyl, tBu = tert-butyl, Ph = phenyl.

Figure 13: Selected orbital magnetic couplings for Tl(I), Pb(II), and Tl(III) complexes, with corresponding δ^{SO}(LA), ΔE, and MO composition and schematic illustrations of the MO → MO* overlap.

Figure 14: Relative energies of Pb^{2+} dimeric hydrides $(HPbR)_2$ for different ligands R = H, Me (methyl), Ph (phenyl), TrpMe (C_6H_3-2,6-(C_6H_2-2,4,6-$(CH_3)_3)_2$).

Figure 15: Structures of possible Pb^{2+} hydrides 1–8 and their $\delta^{CALC}(^1H)$ and $\delta^{SO}(^1H)$. iPr = isopropyl.

Figure 16: ^{15}N NMR chemical shift of N9 upon stretching the Ir–S bond. The δ^{SO} is coded in orange.

Figure 17: Structures of analyzed complexes (left) and dependence of σ^{SO}, s-orbital character of N9, and 5d orbital character of Ir in the Ir-N9 bond. The green line represents the 5d character of Ir scaled to the range of σ^{SO} values to illustrate the correlation better.

Figure 18: Selected MO→MO* magnetic couplings in Pt and Au compounds, corresponding energy differences ΔE, and schematic compositions of MOs involved. Selected Pt MO→MO* magnetic coupling contributes by -25 ppm to δ^{SO}(LA), while Au MO→MO* magnetic coupling contributes by +9 ppm.

Figure 19: Atomic orbital energies in Pt^{2+} and Au^{3+} ions at non-relativistic (NR), scalar-relativistic (SR), and Spin-Orbit (SO) levels.

Figure 20: Correlation between DI (δ) from QTAIM analysis (scaled by Pauling electronegativity to account for various ligand atoms) and $\delta^{SO}(^{13}C,^{15}N)$.

Figure 21: The MO energy levels scheme showing shielding and deshielding δ^{SO}(LA) contributions. The MOs with metal 5d character are on a green background, π-type MOs are in blue, and σ-type HA–LA orbitals are in red. The δ^{SO}(LA) values and 5d contributions to HA–LA bonds (NBO analysis) are at the bottom.

Figure 22: Spin-orbit-induced electron deformation density (SO-EDD) for Pt (left) and Hg (right) complexes.

Figure 23: General trends δ^{SO}(LA) across the Periodic Table. Red color represents deshielding ($\delta^{SO} > 0$), blue color corresponds to the shielding ($\delta^{SO} < 0$). The darker the shade of red or blue, the larger the SO-HALA effects.

Figure 24: a) Schematic structure of Au complex with large sidechains removed for clarity, b) side-on Au_3…H_2-C_2 interaction.

Figure 25: a) Structures of complex **1** conformers **1_A** and **1_B** with bond critical points (BCPs, red) and ring critical points (RCPs, green) from QTAIM analysis, b) Plots of the Laplacian of the electron density.

Figure 26: Left: Structures of $[DMAPH]^+I^-$, $[DMAPH]^+Br^-$, and $[DMAPH]^+Cl^-$ complexes. Right: ^1H MAS NMR spectra of solid $[DMAPH]^+I^-$ and $[DMAPH]^+Br^-$ adducts relative to DSS.

Figure 27: The plot of experimental and calculated (GIPAW/PBE) ^1H NMR chemical shifts in DMAP salts with and without the SO correction.

Figure 28: SO-EDD plot of N_1-H_1⋯I^- interaction in the $[DMAPH]^+I^-$ complex.

Figure 29: Schematic representation of SO-induced magnetic current direction around C_1, C_5, H_6, and H_{10} in osmabenzene and around C_1-C_4 and H_8 in osmapentalene with δ^{SO}(LA) in ppm. Blue represents δ^{SO}(LA) shielding and diatropic SO-induced magnetic current, while red represents δ^{SO}(LA) deshielding and paratropic SO-induced magnetic current.

Figure 30: Relative shifts of XAS spectral lines concerning the percentage of HFX in a functional.

Figure 31: Calculated XAS spectra near the uranium M_4-edge in $UO_2(NO_3)_2$. Comparison of different damping parameters and experimental results. No artificial energy shifts were applied to the spectra.

Figure 32: Comparison of 1eX2C, amfX2C, and 4c reference XAS spectra of $[WCl_4(PMePh_2)_2]$ near $WL_{2,3}$-edges. Note the perfect agreement between amfX2C and 4c. No corrections for energy were performed.

References:

[1] PURCELL, E. M., H. C. TORREY a R. V. POUND. Resonance Absorption by Nuclear Magnetic Moments in a Solid. *Physical Review* [online]. 1946, **69**(1–2), 37–38. Dostupné z: doi:10.1103/PhysRev.69.37

[2] BLOCH, F. Nuclear Induction. *Physical Review* [online]. 1946, **70**(7–8), 460–474. Dostupné z: doi:10.1103/PhysRev.70.460

[3] ABRAGAM, A. a L. C. HEBEL. The Principles of Nuclear Magnetism. *American Journal of Physics* [online]. 1961, **29**(12), 860–861. ISSN 0002-9505. Dostupné z: doi:10.1119/1.1937646

[4] ATKINSON, R. Andrew. NMR of proteins and nucleic acids [online]. 2022 [vid. 2025-07-07]. Dostupné z: doi:10.1039/9781839167690-00249

[5] VÍCHA, Jan, Martin BABINSKÝ, Gabriel DEMO, Olga OTRUSINOVÁ, Séverine JANSEN, Blanka PEKÁROVÁ, Lukáš ŽÍDEK a Markéta L. MUNZAROVÁ. The influence of Mg2+ coordination on 13C and 15N chemical shifts in CKI1RD protein domain from experiment and molecular dynamics/density functional theory calculations. *Proteins: Structure, Function, and Bioinformatics* [online]. 2016, **84**(5), 686–699. ISSN 1097-0134. Dostupné z: doi:10.1002/prot.25019

[6] SCHMIDT-ROHR, K. a H. W. SPIESS. CHAPTER ONE - Introduction. In: K. SCHMIDT-ROHR a H. W. SPIESS, ed. *Multidimensional Solid-State NMR and Polymers* [online]. San Diego: Academic Press, 1994 [vid. 2025-07-07], s. 1–12. ISBN 978-0-08-092562-2. Dostupné z: doi:10.1016/B978-0-08-092562-2.50006-0

[7] MÜNSTER, Lukáš, Jan VÍCHA, Jiří KLOFÁČ, Milan MASAŘ, Anna HURAJOVÁ a Ivo KUŘITKA. Dialdehyde cellulose crosslinked poly(vinyl alcohol) hydrogels: Influence of catalyst and crosslinker shelf life. *Carbohydrate Polymers* [online]. 2018, **198**, 181–190. ISSN 0144-8617. Dostupné z: doi:10.1016/j.carbpol.2018.06.035

[8] RAMSEY, Norman F. Magnetic Shielding of Nuclei in Molecules. *Physical Review* [online]. 1950, **78**(6), 699–703. Dostupné z: doi:10.1103/PhysRev.78.699

[9] PYYKKÖ, Pekka. Relativistic effects in structural chemistry. *Chemical Reviews* [online]. 1988, **88**(3), 563–594. ISSN 0009-2665. Dostupné z: doi:10.1021/cr00085a006

[10] VÍCHA, Jan, Jan NOVOTNÝ, Stanislav KOMOROVSKY, Michal STRAKA, Martin KAUPP a Radek MAREK. Relativistic Heavy-Neighbor-Atom Effects on NMR Shifts: Concepts and Trends Across the Periodic Table. *Chemical Reviews* [online]. 2020, **120**(15), 7065–7103. ISSN 0009-2665. Dostupné z: doi:10.1021/acs.chemrev.9b00785

[11] VÍCHA, Jan, Gabriel DEMO a Radek MAREK. Platinum-Modified Adenines: Unprecedented Protonation Behavior Revealed by NMR Spectroscopy and Relativistic Density-Functional Theory Calculations. *Inorganic Chemistry* [online]. 2012, **51**(3), 1371–1379. ISSN 0020-1669. Dostupné z: doi:10.1021/ic201595e

[12] PAWLAK, T., D. NIEDZIELSKA, J. VICHA, R. MAREK a L. PAZDERSKI. Dimeric Pd(II) and Pt(II) chloride organometallics with 2-phenylpyridine and their solvolysis in dimethylsulfoxide. *Journal of*

Organometallic Chemistry [online]. 2014, **759**, 58–66. ISSN 0022-328X. Dostupné z: doi:10.1016/j.jorganchem.2014.02.016

[13] VÍCHA, Jan, Radek MAREK a Michal STRAKA. High-Frequency 1H NMR Chemical Shifts of SnII and PbII Hydrides Induced by Relativistic Effects: Quest for PbII Hydrides. *Inorganic Chemistry* [online]. 2016, **55**(20), 10302–10309. ISSN 0020-1669. Dostupné z: doi:10.1021/acs.inorgchem.6b01575

[14] KONECNY, Lukas, Stanislav KOMOROVSKY, Jan VICHA, Kenneth RUUD a Michal REPISKY. Exact Two-Component TDDFT with Simple Two-Electron Picture-Change Corrections: X-ray Absorption Spectra Near L- and M-Edges of Four-Component Quality at Two-Component Cost. *The Journal of Physical Chemistry A* [online]. 2023, **127**(5), 1360–1376. ISSN 1089-5639. Dostupné z: doi:10.1021/acs.jpca.2c08307

[15] VÍCHA, Jan, Petr ŠVEC, Zdeňka RŮŽIČKOVÁ, Maksim A. SAMSONOV, Kateřina BÁRTOVÁ, Aleš RŮŽIČKA, Michal STRAKA a Martin DRAČÍNSKÝ. Experimental and Theoretical Evidence of Spin-Orbit Heavy Atom on the Light Atom 1H NMR Chemical Shifts Induced through H···I− Hydrogen Bond. *Chemistry – A European Journal* [online]. 2020, **26**(40), 8698–8702. ISSN 1521-3765. Dostupné z: doi:10.1002/chem.202001532

[16] VÍCHA, Jan, Jan NOVOTNÝ, Michal STRAKA, Michal REPISKY, Kenneth RUUD, Stanislav KOMOROVSKY a Radek MAREK. Structure, solvent, and relativistic effects on the NMR chemical shifts in square-planar transition-metal complexes: assessment of DFT approaches. *Physical Chemistry Chemical Physics* [online]. 2015, **17**(38), 24944–24955. ISSN 1463-9084. Dostupné z: doi:10.1039/C5CP04214C

[17] NOVOTNÝ, Jan, Jan VÍCHA, Pankaj L. BORA, Michal REPISKY, Michal STRAKA, Stanislav KOMOROVSKY a Radek MAREK. Linking the Character of the Metal–Ligand Bond to the Ligand NMR Shielding in Transition-Metal Complexes: NMR Contributions from Spin–Orbit Coupling. *Journal of Chemical Theory and Computation* [online]. 2017, **13**(8), 3586–3601. ISSN 1549-9618. Dostupné z: doi:10.1021/acs.jctc.7b00444

[18] VÍCHA, Jan, Stanislav KOMOROVSKY, Michal REPISKY, Radek MAREK a Michal STRAKA. Relativistic Spin–Orbit Heavy Atom on the Light Atom NMR Chemical Shifts: General Trends Across the Periodic Table Explained. *Journal of Chemical Theory and Computation* [online]. 2018, **14**(6), 3025–3039. ISSN 1549-9618. Dostupné z: doi:10.1021/acs.jctc.8b00144

[19] KONECNY, Lukas, Jan VICHA, Stanislav KOMOROVSKY, Kenneth RUUD a Michal REPISKY. Accurate X-ray Absorption Spectra near L- and M-Edges from Relativistic Four-Component Damped Response Time-Dependent Density Functional Theory. *Inorganic Chemistry* [online]. 2022, **61**(2), 830–846. ISSN 0020-1669. Dostupné z: doi:10.1021/acs.inorgchem.1c02412

[20] DRAČÍNSKÝ, Martin, Jan VÍCHA, Kateřina BÁRTOVÁ a Paul HODGKINSON. Towards Accurate Predictions of Proton NMR Spectroscopic Parameters in Molecular Solids. *ChemPhysChem* [online]. 2020, **21**(18), 2075–2083. ISSN 1439-7641. Dostupné z: doi:10.1002/cphc.202000629

[21] FOROUTAN-NEJAD, Cina, Jan VÍCHA a Abhik GHOSH. Relativity or aromaticity? A first-principles perspective of chemical shifts in osmabenzene and osmapentalene derivatives. *Physical Chemistry Chemical Physics* [online]. 2020, **22**(19), 10863–10869. ISSN 1463-9084. Dostupné z: doi:10.1039/D0CP01481H

[22] VÍCHA, J., C. FOROUTAN-NEJAD a M. STRAKA. 1 H NMR is not a proof of hydrogen bonds in transition metal complexes. *Nature Communications* [online]. 2019, **10**(1), 1643. ISSN 2041-1723. Dostupné z: doi:10.1038/s41467-019-09625-9

[23] GUTHARDT, Robin, Jan OETZEL, Julia I. SCHWEIZER, Clemens BRUHN, Robert LANGER, Martin MAURER, Jan VÍCHA, Pavletta SHESTAKOVA, Max C. HOLTHAUSEN a Ulrich SIEMELING. Reactive Dimerization of an N-Heterocyclic Plumbylene: C−H Activation with PbII. *Angewandte Chemie* [online]. 2019, **131**(5), 1401–1405. ISSN 1521-3757. Dostupné z: doi:10.1002/ange.201811559

[24] VÍCHA, Jan, Radek MAREK a Michal STRAKA. High-Frequency 13C and 29Si NMR Chemical Shifts in Diamagnetic Low-Valence Compounds of TlI and PbII: Decisive Role of Relativistic Effects. *Inorganic Chemistry* [online]. 2016, **55**(4), 1770–1781. ISSN 0020-1669. Dostupné z: doi:10.1021/acs.inorgchem.5b02689

[25] VÍCHA, Jan, Cina FOROUTAN-NEJAD, Tomasz PAWLAK, Markéta L. MUNZAROVÁ, Michal STRAKA a Radek MAREK. Understanding the Electronic Factors Responsible for Ligand Spin–Orbit NMR Shielding in Transition-Metal Complexes. *Journal of Chemical Theory and Computation* [online]. 2015, **11**(4), 1509–1517. ISSN 1549-9618. Dostupné z: doi:10.1021/ct501089z

[26] VÍCHA, Jan, Michal STRAKA, Markéta L. MUNZAROVÁ a Radek MAREK. Mechanism of Spin–Orbit Effects on the Ligand NMR Chemical Shift in Transition-Metal Complexes: Linking NMR to EPR. *Journal of Chemical Theory and Computation* [online]. 2014, **10**(4), 1489–1499. ISSN 1549-9618. Dostupné z: doi:10.1021/ct400726y

[27] STRAKA, Michal, Erik ANDRIS, Jan VÍCHA, Aleš RŮŽIČKA, Jana ROITHOVÁ a Lubomír RULÍŠEK. Spectroscopic and Computational Evidence of Intramolecular AuI···H+−N Hydrogen Bonding. *Angewandte Chemie* [online]. 2019, **131**(7), 2033–2038. ISSN 1521-3757. Dostupné z: doi:10.1002/ange.201811982

[28] VÍCHA, Jan, Juha VAARA a Michal STRAKA. The essential role of symmetry in understanding 3He chemical shifts in endohedral helium fullerenes. *Physical Chemistry Chemical Physics* [online]. 2023, **25**(15), 10620–10627. ISSN 1463-9084. Dostupné z: doi:10.1039/D3CP00256J

[29] VÍCHA, Jan, Michael PATZSCHKE a Radek MAREK. A relativistic DFT methodology for calculating the structures and NMR chemical shifts of octahedral platinum and iridium complexes. *Physical Chemistry Chemical Physics* [online]. 2013, **15**(20), 7740–7754. ISSN 1463-9084. Dostupné z: doi:10.1039/C3CP44440F

[30] AUTSCHBACH, Jochen. Relativistic Effects on Magnetic Resonance Parameters and Other Properties of Inorganic Molecules and Metal Complexes. In: Maria BARYSZ a Yasuyuki ISHIKAWA, ed. *Relativistic Methods for Chemists* [online]. B.m.: Springer Netherlands, 2010 [vid. 2015-03-18], Challenges and Advances in Computational Chemistry and Physics, 10, s. 521–598. ISBN 978-1-4020-9974-8. Dostupné z: http://link.springer.com/chapter/10.1007/978-1-4020-9975-5_12

[31] KAUPP, Martin, Olga L. MALKINA, Vladimir G. MALKIN a Pekka PYYKKÖ. How Do Spin–Orbit-Induced Heavy-Atom Effects on NMR Chemical Shifts Function? Validation of a Simple Analogy to Spin–Spin Coupling by Density Functional Theory (DFT) Calculations on Some Iodo Compounds. *Chemistry – A European Journal* [online]. 1998, **4**(1), 118–126. ISSN 1521-3765. Dostupné z: doi:10.1002/(SICI)1521-3765(199801)4:1<118::AID-CHEM118>3.0.CO;2-6

[32] PYYKKÖ, Pekka, Andreas GÖRLING a Notker RÖSCH. A transparent interpretation of the relativistic contribution to the N.M.R. 'heavy atom chemical shift'. *Molecular Physics* [online]. 1987, **61**, 195–205. ISSN 0026-8976. Dostupné z: doi:10.1080/00268978700101071

[33] HEGETSCHWEILER, Kaspar, Dirk KUPPERT, Jochen HUPPERT, Michal STRAKA a Martin KAUPP. Spin−Orbit-Induced Anomalous pH-Dependence in 1H NMR Spectra of CoIII Amine Complexes: A Diagnostic Tool for Structure Elucidation. *Journal of the American Chemical Society* [online]. 2004, **126**(21), 6728–6738. ISSN 0002-7863. Dostupné z: doi:10.1021/ja0316723

[34] HYVARINEN, M., J. VAARA, A. GOLDAMMER, B. KUTZKY, K. HEGETSCHWEILER, M. KAUPP a M. STRAKA. Characteristic Spin-Orbit Induced H-1(CH2) Chemical Shifts upon Deprotonation of Group 9 Polyamine Aqua and Alcohol Complexes. *Journal of the American Chemical Society* [online]. 2009, **131**(33), 11909–11918. ISSN 0002-7863. Dostupné z: doi:10.1021/ja903637m

[35] IUPAC. Recommendations for the Presentation of NMR Data for Publication in Chemical Journals. *Pure and Applied Chemistry* [online]. 1972, **29**(4), 625–628. ISSN 0033-4545, 1365-3075. Dostupné z: doi:10.1351/pac197229040625

[36] NAKAGAWA, N., S. SINADA a S. OBINATA. The 6th NMR Symposium. *The 6th NMR Symposium*. 1967, 8–8.

[37] NOMURA, Yujiro, Yoshito TAKEUCHI a Naoya NAKAGAWA.]Substituent effects in aromatic proton nmr spectra. III substituent effects caused by halogens. *Tetrahedron Letters* [online]. 1969, **10**(8), 639–642. ISSN 0040-4039. Dostupné z: doi:10.1016/S0040-4039(01)87770-4

[38] PITZER, Kenneth S. RELATIVISTIC EFFECTS ON CHEMICAL PROPERTIES [online]. 1978 [vid. 2025-07-07]. Dostupné z: https://escholarship.org/uc/item/2vb947cs

[39] DESCLAUX, J. P. Relativistic Dirac-Fock expectation values for atoms with Z = 1 to Z = 120. *Atomic Data and Nuclear Data Tables* [online]. 1973, **12**(4), 311–406. ISSN 0092-640X. Dostupné z: doi:10.1016/0092-640X(73)90020-X

[40] DESCLAUX, J. P. a P. PYYKKÖ. Dirac-Fock one-centre calculations. The molecules CuH, AgH and AuH including p-type symmetry functions. *Chemical Physics Letters* [online]. 1976, **39**(2), 300–303. ISSN 0009-2614. Dostupné z: doi:10.1016/0009-2614(76)80080-2

[41] PYYKKO, Pekka a Jean Paul DESCLAUX. Relativity and the periodic system of elements. *Accounts of Chemical Research* [online]. 1979, **12**(8), 276–281. ISSN 0001-4842. Dostupné z: doi:10.1021/ar50140a002

[42] CRAMER, Christopher J. Introduction to Relativistic Quantum Chemistry. *Theoretical Chemistry Accounts* [online]. 2008, **119**(5–6), 523–524. ISSN 1432-881X, 1432-2234. Dostupné z: doi:10.1007/s00214-007-0399-y

[43] BETHE, Hans A. a Edwin E. SALPETER. *Quantum Mechanics of One- and Two-Electron Atoms* [online]. Berlin, Heidelberg: Springer Berlin Heidelberg, 1957 [vid. 2025-07-08]. ISBN 978-3-662-12871-8. Dostupné z: doi:10.1007/978-3-662-12869-5

[44] ANDRAE, D., U. HÄUSSERMANN, M. DOLG, H. STOLL a H. PREUSS. Energy-adjustedab initio pseudopotentials for the second and third row transition elements. *Theoretica chimica acta* [online]. 1990, **77**(2), 123–141. ISSN 0040-5744, 1432-2234. Dostupné z: doi:10.1007/BF01114537

[45] VAARA, Juha. Theory and computation of nuclear magnetic resonance parameters. *Physical Chemistry Chemical Physics* [online]. 2007, **9**(40), 5399. ISSN 1463-9076, 1463-9084. Dostupné z: doi:10.1039/b706135h

[46] VAARA, Juha, Olga L. MALKINA, Hermann STOLL, Vladimir G. MALKIN a Martin KAUPP. Study of relativistic effects on nuclear shieldings using density-functional theory and spin–orbit pseudopotentials. *The Journal of Chemical Physics* [online]. 2001, **114**(1), 61–71. ISSN 0021-9606, 1089-7690. Dostupné z: doi:10.1063/1.1330208

[47] DYALL, Kenneth G. a Knut FAEGRI JR. *Introduction to Relativistic Quantum Chemistry*. B.m.: Oxford University Press, 2007. ISBN 978-0-19-803230-4.

[48] KOMOROVSKY, Stanislav, Michal REPISKY, Olga L. MALKINA, Vladimir G. MALKIN, Irina Malkin ONDÍK a Martin KAUPP. A fully relativistic method for calculation of nuclear magnetic shielding tensors with a restricted magnetically balanced basis in the framework of the matrix Dirac–Kohn–Sham equationa). *The Journal of Chemical Physics* [online]. 2008, **128**(10), 104101. ISSN 0021-9606, 1089-7690. Dostupné z: doi:10.1063/1.2837472

[49] REPISKY, Michal, Stanislav KOMOROVSKY, Olga L. MALKINA a Vladimir G. MALKIN. Restricted magnetically balanced basis applied for relativistic calculations of indirect nuclear spin–spin coupling tensors in the matrix Dirac–Kohn–Sham framework. *Chemical Physics* [online]. 2009, **356**(1–3), Moving Frontiers in Quantum Chemistry: Electron Correlation, Molecular Properties and Relativity, 236–242. ISSN 0301-0104. Dostupné z: doi:10.1016/j.chemphys.2008.10.037

[50] REPISKY, Michal, Stanislav KOMOROVSKY, Marius KADEK, Lukas KONECNY, Ulf EKSTRÖM, Elena MALKIN, Martin KAUPP, Kenneth RUUD, Olga L. MALKINA a Vladimir G. MALKIN. ReSpect: Relativistic spectroscopy DFT program package. *The Journal of Chemical Physics* [online]. 2020, **152**(18), 184101. ISSN 0021-9606. Dostupné z: doi:10.1063/5.0005094

[51] DYALL, Kenneth G. Interfacing relativistic and nonrelativistic methods. IV. One- and two-electron scalar approximations. *The Journal of Chemical Physics* [online]. 2001, **115**(20), 9136–9143. ISSN 0021-9606. Dostupné z: doi:10.1063/1.1413512

[52] SAUE, Trond. Relativistic Hamiltonians for Chemistry: A Primer. *Chem. Phys. Chem.* [online]. 2011, **12**(17), 3077–3094. ISSN 1439-7641. Dostupné z: doi:10.1002/cphc.201100682

[53] LIU, Junzi a Lan CHENG. An atomic mean-field spin-orbit approach within exact two-component theory for a non-perturbative treatment of spin-orbit coupling. *The Journal of Chemical Physics* [online]. 2018, **148**(14), 144108. ISSN 0021-9606. Dostupné z: doi:10.1063/1.5023750

[54] LENTHE, E. van, J. G. SNIJDERS a E. J. BAERENDS. The zero-order regular approximation for relativistic effects: The effect of spin–orbit coupling in closed shell molecules. *The Journal of Chemical Physics* [online]. 1996, **105**(15), 6505–6516. ISSN 0021-9606, 1089-7690. Dostupné z: doi:10.1063/1.472460

[55] ADAMO, Carlo a Vincenzo BARONE. Toward reliable density functional methods without adjustable parameters: The PBE0 model. *The Journal of Chemical Physics* [online]. 1999, **110**(13), 6158–6170. ISSN 0021-9606, 1089-7690. Dostupné z: doi:10.1063/1.478522

[56] ADAMO, Carlo, Gustavo E. SCUSERIA a Vincenzo BARONE. Accurate excitation energies from time-dependent density functional theory: Assessing the PBE0 model. *The Journal of Chemical Physics* [online]. 1999, **111**(7), 2889–2899. ISSN 0021-9606, 1089-7690. Dostupné z: doi:10.1063/1.479571

[57] AUTSCHBACH, Jochen. The role of the exchange-correlation response kernel and scaling corrections in relativistic density functional nuclear magnetic shielding calculations with the zeroth-order regular approximation. *Molecular Physics* [online]. 2013, **111**(16–17), 2544–2554. ISSN 0026-8976. Dostupné z: doi:10.1080/00268976.2013.796415

[58] MALKIN, Vladimir G., Olga L. MALKINA, Mark E. CASIDA a Dennis R. SALAHUB. Nuclear Magnetic Resonance Shielding Tensors Calculated with a Sum-over-States Density Functional Perturbation Theory. *Journal of the American Chemical Society* [online]. 1994, **116**(13), 5898–5908. ISSN 0002-7863. Dostupné z: doi:10.1021/ja00092a046

[59] STANDARA, Stanislav, Kateřina MALIŇÁKOVÁ, Radek MAREK, Jaromír MAREK, Michal HOCEK, Juha VAARA a Michal STRAKA. Understanding the NMR chemical shifts for 6-halopurines: role of structure, solvent and relativistic effects. *Physical Chemistry Chemical Physics* [online]. 2010, **12**(19), 5126–5139. ISSN 1463-9084. Dostupné z: doi:10.1039/B921383J

[60] LANTTO, Perttu, Stanislav STANDARA, Sebastian RIEDEL, Juha VAARA a Michal STRAKA. Exploring new 129Xe chemical shift ranges in HXeY compounds: hydrogen more relativistic than xenon. *Physical Chemistry Chemical Physics* [online]. 2012, **14**(31), 10944–10952. ISSN 1463-9084. Dostupné z: doi:10.1039/C2CP41240C

[61] NICOL, A. T. a R. W. VAUGHAN. Proton chemical shift tensors of alkaline earth hydrides. *The Journal of Chemical Physics* [online]. 1978, **69**(11), 5211–5213. ISSN 0021-9606. Dostupné z: doi:10.1063/1.436475

[62] HAYASHI, Katsuro, Peter V. SUSHKO, Yasuhiro HASHIMOTO, Alexander L. SHLUGER a Hideo HOSONO. Hydride ions in oxide hosts hidden by hydroxide ions. *Nature Communications* [online]. 2014, **5**, 3515. ISSN 2041-1723. Dostupné z: doi:10.1038/ncomms4515

[63] HROBÁRIK, Peter, Veronika HROBÁRIKOVÁ, Florian MEIER, Michal REPISKÝ, Stanislav KOMOROVSKÝ a Martin KAUPP. Relativistic Four-Component DFT Calculations of 1H NMR Chemical Shifts in Transition-Metal Hydride Complexes: Unusual High-Field Shifts Beyond the Buckingham–Stephens Model. *The Journal of Physical Chemistry A* [online]. 2011, **115**(22), 5654–5659. ISSN 1089-5639. Dostupné z: doi:10.1021/jp202327z

[64] KAPUR, Shushma, B. L. KALSOTRA a R. K. MULTANI. Hydride and amide derivatives of tricyclopentadienyl cerium(IV) and bisindenyl cerium(IV). *Journal of Inorganic and Nuclear Chemistry* [online]. 1974, **36**(4), 932–934. ISSN 0022-1902. Dostupné z: doi:10.1016/0022-1902(74)80841-9

[65] GREIF, Anja H., Peter HROBÁRIK, Jochen AUTSCHBACH a Martin KAUPP. Giant spin–orbit effects on 1H and 13C NMR shifts for uranium(VI) complexes revisited: role of the exchange–correlation response

kernel, bonding analyses, and new predictions [online]. 2016, **18**(44), 30462–30474. ISSN 1463-9084. Dostupné z: doi:10.1039/C6CP06129J

[66] HROBÁRIK, Peter, Veronika HROBÁRIKOVÁ, Anja H. GREIF a Martin KAUPP. Giant Spin-Orbit Effects on NMR Shifts in Diamagnetic Actinide Complexes: Guiding the Search of Uranium(VI) Hydride Complexes in the Correct Spectral Range. *Angewandte Chemie International Edition* [online]. 2012, **51**(43), 10884–10888. ISSN 1521-3773. Dostupné z: doi:10.1002/anie.201204634

[67] SCHNEIDER, Julia, Christian P. SINDLINGER, Klaus EICHELE, Hartmut SCHUBERT a Lars WESEMANN. Low-Valent Lead Hydride and Its Extreme Low-Field 1H NMR Chemical Shift. *Journal of the American Chemical Society* [online]. 2017, **139**(19), 6542–6545. ISSN 0002-7863. Dostupné z: doi:10.1021/jacs.7b01856

[68] GEHRHUS, Barbara, Peter B. HITCHCOCK a Michael F. LAPPERT. New Reactions of a Silylene: Insertion into M□N Bonds of M[N(SiMe3)2]2 (M □ Ge, Sn, or Pb). *Angewandte Chemie International Edition in English* [online]. 1997, **36**(22), 2514–2516. ISSN 1521-3773. Dostupné z: doi:10.1002/anie.199725141

[69] ARUNAN, Elangannan, Gautam R. DESIRAJU, Roger A. KLEIN, Joanna SADLEJ, Steve SCHEINER, Ibon ALKORTA, David C. CLARY, Robert H. CRABTREE, Joseph J. DANNENBERG, Pavel HOBZA, Henrik G. KJAERGAARD, Anthony C. LEGON, Benedetta MENNUCCI a David J. NESBITT. Definition of the hydrogen bond (IUPAC Recommendations 2011). *Pure and Applied Chemistry* [online]. 2011, **83**(8), 1637–1641. ISSN 1365-3075, 0033-4545. Dostupné z: doi:10.1351/pac-rec-10-01-02

[70] REEK, Joost N. H., Bas DE BRUIN, Sonja PULLEN, Tiddo J. MOOIBROEK, Alexander M. KLUWER a Xavier CAUMES. Transition Metal Catalysis Controlled by Hydrogen Bonding in the Second Coordination Sphere. *Chemical Reviews* [online]. 2022, **122**(14), 12308–12369. ISSN 0009-2665. Dostupné z: doi:10.1021/acs.chemrev.1c00862

[71] SCHMIDBAUR, Hubert, Helgard G. RAUBENHEIMER a Liliana DOBRZAŃSKA. The gold–hydrogen bond, Au–H, and the hydrogen bond to gold, Au···H–X. *Chemical Society Reviews* [online]. 2013, **43**(1), 345–380. ISSN 1460-4744. Dostupné z: doi:10.1039/C3CS60251F

[72] BAKAR, Md Abu, Mizuho SUGIUCHI, Mitsuhiro IWASAKI, Yukatsu SHICHIBU a Katsuaki KONISHI. Hydrogen bonds to Au atoms in coordinated gold clusters. *Nature Communications* [online]. 2017, **8**(1), 576. ISSN 2041-1723. Dostupné z: doi:10.1038/s41467-017-00720-3